Non-Destructive Estimation of Particle Size in Granular Compacts by Terahertz Scattering

Keir N Murphy

Strathclyde Institute of Pharmacy and Biomedical Sciences

University of Strathclyde

Glasgow, UK

A thesis submitted in fulfilment of the requirements for the degree of

Doctor of Philosophy

January 08, 2024

This thesis is the result of the author's original research. It has been composed by the author and has not been previously submitted for examination, which has led to the award of a degree.

Signed: *Keir N Murphy*

Date: 08/January/2024

Abstract

Particle size measurements in granular compacts are crucial for various industries, particularly pharmaceuticals, to ensure product quality and efficiency. In the pharmaceutical industry, variations in particle size of either active pharmaceutical ingredients (APIs) or excipients occur throughout the manufacturing process. Particle size variation in pharmaceutical products has been extensively investigated and is linked to altered dissolution performance, thus impacting the efficacy and quality of the final product. However, current methods for particle size monitoring are predominantly offline and destructive, bearing various inherent limitations. This necessitates the need for innovative techniques. An ideal solution would encompass various characteristics, such as allowing for non-destructive in-situ monitoring during the manufacturing process. To this end, the application of terahertz time-domain spectroscopy (THz-TDS) as a technique for quantifying particle or domain size in granular compacts is considered.

Samples were developed comprising a mixture of polymer powder and borosilicate microspheres, allowing for the isolation of particle size and concentration in compacts. Multiple polymer materials were compacted and analysed at various pressures to minimise sample porosity while ensuring sufficient compact strength for further handling. It was determined that polytetrafluoroethylene (PTFE) was the preferred matrix material with acceptable tensile strength and exhibiting minimal porosity if compacted at 392 MPa. Finally, ten borosilicate microsphere samples were fabricated at six concentration levels and five particle sizes to isolate the effect of particle size and concentration on THz scattering.

Employing THz-TDS, each compact and optical grade borosilicate glass windows were analysed at low frequencies (<1.2 THz) before extraction of the scattering contributions to the loss coefficient. It was observed that the scattering increased linearly at low concentrations before the onset of saturation and subsequently decreased at higher concentrations. Additionally, the typical approach to scattering analysis via power law fitting was investigated, and the dependence of the fitting parameters was

determined, with the exponent being solely dependent on concentration. The pre-exponent was dependent on particle size and concentration, leading to the potential for particle size estimation with simple linear fitting.

Furthermore, complex pharmaceutical compacts fabricated at various compaction pressures and API particle sizes are analysed using THz-TDS. The extracted loss coefficient suggested that API agglomeration occurred in smaller particle-size batches, increasing the loss coefficient at THz frequencies. Subsequent near-infrared chemical imaging confirmed the presence of API agglomeration. The use of power law fitting allowed for the development of a linear model (R^2= 0.91) for the non-destructive estimation of agglomerate size. This work highlights the applicability of THz-TDS for the estimation of particle size changes in granular compacts with the aid of a linear model.

The thesis culminates with an unexpected discovery upon extending the scattering analysis to higher frequencies. The emergence of spurious peaks was observed, attributed to multiple paths of photon propagation through a mixture. This finding raises concerns for confidence in THz-TDS measurements at higher frequencies (>2 THz); therefore, further work is recommended. However, it should be noted that the analysis in chapters 3-5 was conducted at lower frequencies where this effect is negligible.

This thesis underscores the applicability of THz-TDS for estimating particle size changes in granular compacts while providing crucial insights into other material characteristics, such as sample porosity. Additionally, it advances our current understanding of scattering in the terahertz region, specifically in mixed materials. Finally, a concerning finding is highlighted that could significantly impact the reproducibility and accuracy of THz-TDS analysis of granular compacts at high frequencies.

Contents

Abbreviations

SOD	Solid oral dosage forms
PAT	Process analytical technique
CQA	Critical quality attribute
UHPLC-UV	Ultra high-performance liquid chromatography (UV detection)
API	Active pharmaceutical ingredient
PSD	Particle size distribution
ZPA	Zero porosity approximation
NIRS	Near infra-red spectroscopy
NIR-CI	Near infra-red chemical imaging
PCA	Principle component analysis
FBRM	Focused beam reflectance measurement
CLD	Chord length distribution

THz	Terahertz
THz-TDS	Terahertz time-domain spectroscopy
DR	Dynamic range
FSR	Free spectral range
EMT	Effective medium theory
PTFE	Polytetrafluoroethylene
PE	Polyethylene
HDPE	High-density polyethylene
RI	Refractive index
HPV	Hydraulic press with vacuum
HPNV	Hydraulic press without vacuum
QBD	Quality by design
DLS	Dynamic light scattering

Nomenclature

n	Refractive index
c	Speed of light
L	Sample thickness
υ	Frequency
d	Diameter
H	Height
h	Breaking force
ρ	Density
m	mass
f	Porosity
P	Pressure
F	Force
A	Area

g	Gravity
ϕ	Phase
I	Intensity
C	Concentration
V	Volume
r	Axial relaxation
σ_t	Tensile strength
α_{abs}	Absorption coefficient
α_{max}	Maximum absorption
α_{loss}	Loss coefficient
α_{scatt}	Scattering contributions
$R(\nu)$	Fresnel reflection
$T(\nu)$	Fresnel transmission
E	Electric field

Acknowledgements

I thank my supervisors, Dr Daniel Markl, Dr Mira Naftaly, and Dr Alison Nordon. Their guidance and patience in teaching the fundamentals of scientific research have been invaluable and have shaped me into the person I am today. I could not have completed this project without their constant encouragement; they truly have been the best mentors I could have ever hoped for.

I would also like to thank various PhD students and collaborators who have helped me through the project's more difficult periods. First, I would like to thank Peter Hou, Natalie MacLean, Hannah Jesney, Daniel Powell, Peter Martin, Silke Henry, and Russell Miler, who have supported me during rough times. I would also like to thank Dr Alexander Ryckaert, who has taught me much since our meeting in the project's first year; I wish you all the best in your future endeavours.

I would also like to thank my sister (Ainsley Murphy) for her support throughout the project. Finally, I would like to thank my family, my mother and father (Elizabeth and Brian Murphy), who were my first and most cherished teachers.

Thank you all.

Keir N Murphy

Research Outputs

Journal Papers

1. **K. N. Murphy,** M. Naftaly, A. Nordon, and D. Markl, “Polymer Pellet Fabrication for Accurate THz-TDS Measurements,” Appl. Sci., vol. 12, no. 7, p. 3475, 2022, doi: 10.3390/app12073475.

2. **K. N. Murphy,** M. Naftaly, A. Nordon, and D. Markl, “Effect of particle size and concentration on low-frequency terahertz scattering in granular compacts [Invited].” Optical Materials Express, vol. 13,no. 8, p. 2251, 2023, doi 10.1364/ome.494825

3. **K. N. Murphy,** D. Markl, A. Nordon, and M. Naftaly, “Observation of spurious spectral features in mixed-powder compressed pellets measured by terahertz time-domain spectroscopy.,” *IEEE Transactions on Terahertz Science and Technology*, vol. 13, no. 5, pp. 569-572, Sept. 2023, doi: 10.1109/TTHZ.2023.3290118.

Oral Presentation Conference Contributions

1. **K. N. Murphy,** M. Naftaly, A. Nordon, and D. Markl, “Effect of Microsphere Concentration and Size in Compacts on Terahertz Scattering,” *2021 51st European Microwave Conference (EuMC)*, London, United Kingdom, 2022, pp. 994-997, doi: 10.23919/EuMC50147.2022.9784372.

2. **K. N. Murphy,** M. Naftaly, A. Nordon, and D. Markl, “Analysis of THz Scattering of Compacted Granular Materials using THz-TDS.,” in 2022 47th International Conference on Infrared, Millimeter and Terahertz Waves (IRMMW-THz)*, Delft, Netherlands, 2022, pp. 1-2, doi: 10.1109/IRMMW-THz50927.2022.9895792*

3. **K. N. Murphy,** M. Naftaly, A. Nordon and D. Markl, "The Effect of Terahertz Scattering on Loss Coefficient in Granular Compacts," 2023 48th International Conference on Infrared, Millimeter, and Terahertz Waves (IRMMW-THz), Montreal, QC, Canada, 2023, pp. 1-2, doi: 10.1109/IRMMW-THz57677.2023.10299219.

1 Introduction

1.1 Importance of Particle and Domain Size in the Process Industry

The process industry is pivotal in manufacturing essential commodities required for modern life. These industries include a diverse array of sectors, varying from pharmaceuticals, which are critical for producing and developing high-quality medications, to the construction materials sector, which fabricates products encompassing cement, tiles, and plaster.

Granular materials, composed of discrete particles that interact through friction or cohesive forces, exhibit complex behaviours that dictate various process-critical factors, including powder flow. To understand these complex behaviours, a concept called domain size is typically employed to portray a length scale of distinct regions in the materials. An example of this is segregation, where smaller particles separate from larger ones, creating two distinct size domains. In contrast, particle size refers to the dimension of a single particle or a distribution of particles.

Domain size plays a pivotal role in granular materials, profoundly influencing the final product in various industries, including paints and emulsions, construction, and pharmaceuticals (Beekman et al., 2005; Shekunov et al., 2007). Alterations in particle size in the construction industry affect the optimal process parameters (powder flow, mix proportioning, etc.) as well as the visual and tactile properties of the final product, such as cement, tiles, and plaster (Rawle, 2014; Shekunov et al., 2007). In addition to the changes in visual and tactile properties, inhomogeneous particle size mixtures can lead to the product's breakage.

Similarly, particle size changes in paints and emulsions lead to modifications to material properties such as opacity and weather resistance (Figure 1-1).

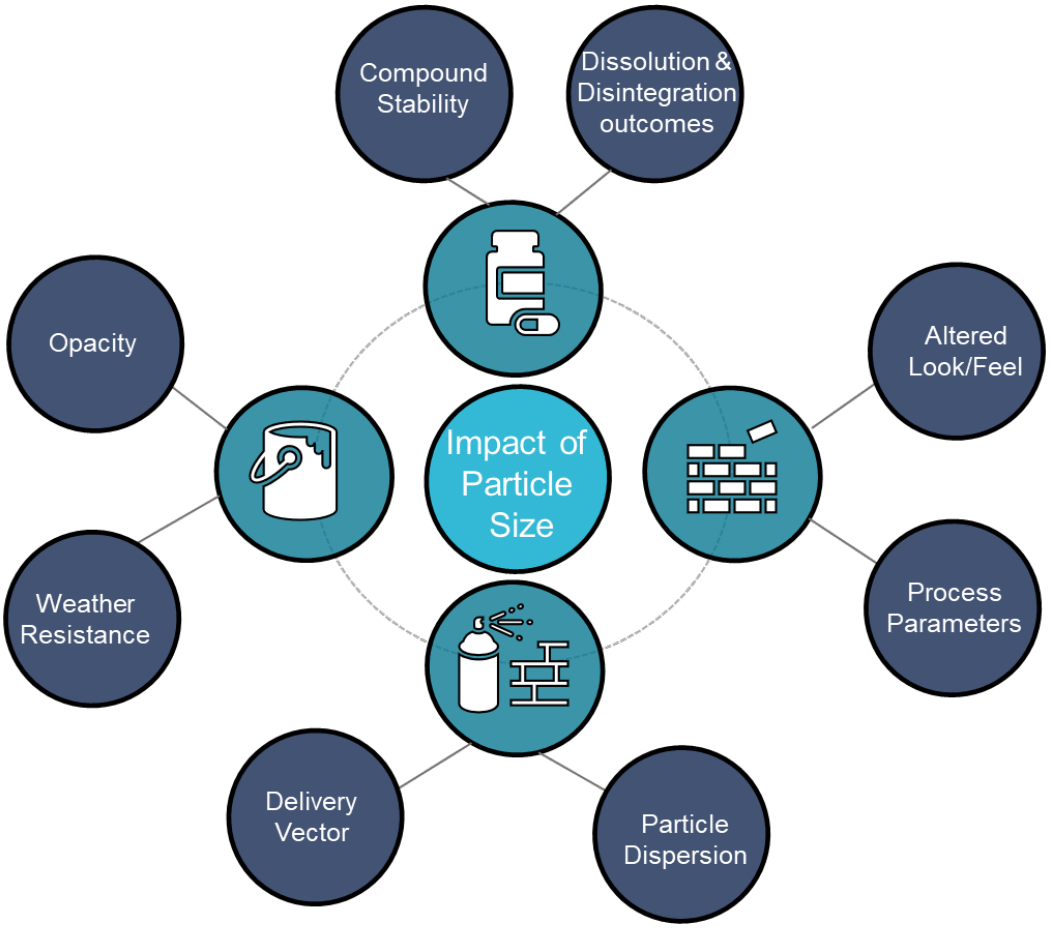

Figure 1-1: The effect of particle size in various industries (pharmaceuticals, construction, aerosols & paints/emulsions) on final product quality and performance.

1.2 Importance of Particle and Domain Size in the Pharmaceutical Industry

In the pharmaceutical industry, oral solid dosage (OSD) forms such as tablets and capsules dominate the drug administration market, accounting for at least 63% of the market share (Zhong et al., 2018). These products are manufactured through various techniques and processes, commonly including crystallisation, feeding, blending and compaction (Silva et al., 2013). To ensure product quality, process analytical techniques (PAT) are employed to develop

process understanding and to monitor critical quality attributes (CQAs) during manufacture (Alshihabi et al., 2012; Clegg, 2020; Kumar et al., 2013).

The CQAs are material and product characteristics integral to the Quality by Design (QBD) ethos and ensure product adherence to quality specifications. During formulation development, CQAs are determined to provide manufacturing targets, ensuring the final product quality. Particle or domain size significantly affects the CQA, e.g., slowed dissolution rates of the active pharmaceutical ingredient (API) affect bioavailability and, therefore, the product's efficacy. The particle or domain size can change throughout the manufacturing process through various mechanisms, including.

- Compaction—High pressure is exerted on the powder blend to create a tablet, potentially fragmenting particles.

- Agglomeration —This technique is commonly applied to increase particle size in a controlled manner to improve powder flowability and blend uniformity.

- Uncontrolled agglomeration—Occurs due to cohesive forces or moisture forming particle aggregates increasing dissolution time.

This section continues to discuss each of these processes in greater depth before exploring the effect of such changes on dissolution rates and bioavailability of the API:

Compaction: One process that can lead to a change in particle size or domain size is during compaction of the formulation (Anuschek et al., 2023; Skelbæk-Pedersen et al., 2020). During compaction, powder blends are compressed into compacts upon which deformation can occur (Figure 1-2). For brittle materials, this compression can cause fragmentation of the particles, leading to a change in particle size distribution (PSD) or domain size (Silva et al., 2013).

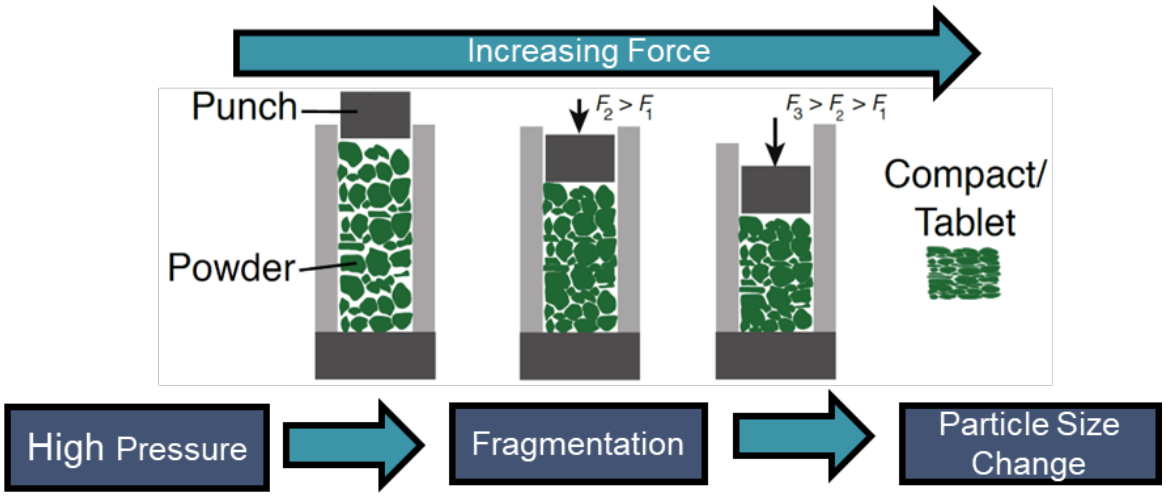

Figure 1-2: Compaction of pharmaceutical blends into compacted tablets. High pressure compaction can lead to fragmentation of particles, especially of brittle materials.

Agglomeration: Particle agglomeration is another method by which particle size changes can occur throughout various stages in the manufacturing process. Agglomeration involves transforming fine particles into an aggregate where individual primary particles can still be identified. In pharmaceutical manufacturing, controlled agglomeration, commonly known as granulation, is pivotal in improving powder flowability, particle size distribution, and blend uniformity. It is a process in which a binder is added to bulk powder, creating granules through bridges between individual particles.

Uncontrolled agglomeration: Uncontrolled agglomeration presents challenges during manufacturing, particularly during blending (Gupta et al., 2022). It occurs when the cohesive

forces (Van der Walls or electrostatic forces) lead to the generation of agglomerates, negatively affecting the CQAs of the final product, such as the dissolution rate (Burgess et al., 2004; Gupta et al., 2022; Hartley et al., 1985). Additionally, moisture can function as a binder for the agglomeration of fine particles (especially hygroscopic materials).

Changes in the particle or domain size are known to affect the dissolution rate and the bioavailability of the API (Silva et al., 2013). The dissolution rate depends on the particle surface area, with smaller particles dissolving faster than larger ones, influencing API uptake into the bloodstream and, therefore, the product's therapeutic effect (Silva et al., 2013). Another critical attribute is compound stability, where maintaining potency and safety after storage is pivotal. Particle size can change during storage as larger domain sizes are observed when particles partially dissolve and recrystallise due to the moisture and temperature in the environment. These particles can then form a solid bridge, resulting in larger particles that dissolve slower, leading to a slowdown of the dissolution of the product (Maclean et al., 2022).

PAT monitoring is commonly employed to detect changes in domain or particle size during manufacture to ensure OSD performance and quality. As the industry shifts to continuous manufacturing, a PAT capable of non-destructive and contactless analysis is paramount. Such a technique should also possess the ability to provide measurements that probe a representative volume of the sample and have a fast analysis time (Challa & Potumarthi, 2013). Current techniques, however, are hampered by various limitations, including being offline and destructive, requiring specialised sample preparation or being limited to surface analysis, hindering detection of particle size changes in the core.

1.3 State of the Art of Process Analytical Technologies for Particle Size and Domain Size Measurements

Given the wide-ranging impact on performance and manufacturability (Shekunov et al., 2007), process analytical tools are critical to identifying particle size changes throughout manufacturing. This section discusses the current state-of-the-art techniques in particle size estimation and their advantages and disadvantages for application to the pharmaceutical industry.

1.3.1 Particle and Domain Size Characterization

Characterisation of regularly shaped particles, such as spheres or cylinders, can accurately be described by well-defined dimensions such as radius and height. However, irregularly shaped particles pose challenges in particle size characterisation for real-world applications. The characterisation of such particles varies between the different analytical techniques employed (Martin Rhodes, 2008). The primary dimension characterising the particle or domain size is the diameter. This section explores the dimensions employed to characterise particle size before delving into distributions and their effect on PAT.

One method for the description of particle size is the area (d_s) or volume equivalent diameter (d_v) (Martin Rhodes, 2008), commonly employed in laser diffraction and dynamic light scattering (DLS). This approach estimates a spherical particle with a diameter (d) equivalent to the measured area (S_p) or volume (V_p) as in Equations 1 and 2.

$$V_p = \frac{\pi}{6} d_V^3 \tag{1}$$

$$S_p = \pi d_s^2 \quad (2)$$

Developing the equivalent diameter using both the particle volume and area, an equivalent surface-to-volume diameter (d_{SS}) can be obtained as in Equation 3.

$$\frac{S_p}{V_p} = \frac{6}{d_{SS}} \quad (3)$$

The sieve diameter is another approach to quantifying particle size employed when sieving a material (Martin Rhodes, 2008). The diameter represents the minimum sieve size through which the particle could pass (Figure 1-3).

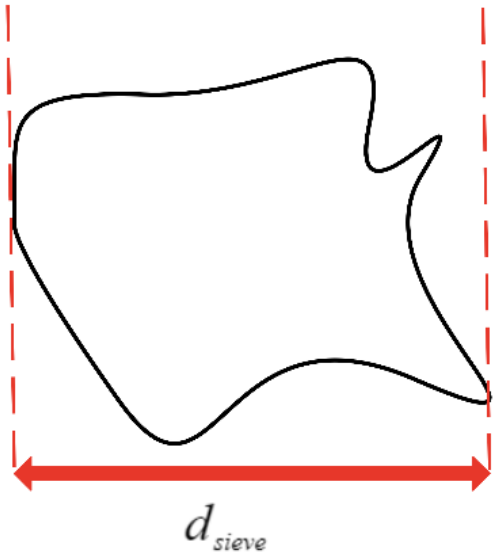

Figure 1-3: Diagram depicting the sieve diameter. Smallest sieve size the particle can pass through.

This approach has various limitations for particle size analysis, including the potential for larger particles to pass through the sieve, reducing the technique's reliability. Additionally, like the equivalent diameter method, no insight into particle shape can be obtained.

The chord length (Martin's diameter) is another method employed for particle size characterisation, used in focussed beam reflectance measurements (FBRM) (Martin Rhodes, 2008). The chord length represents the distance between two points in a particle, typically determined via the path of the FBRM laser (Figure 1-4).

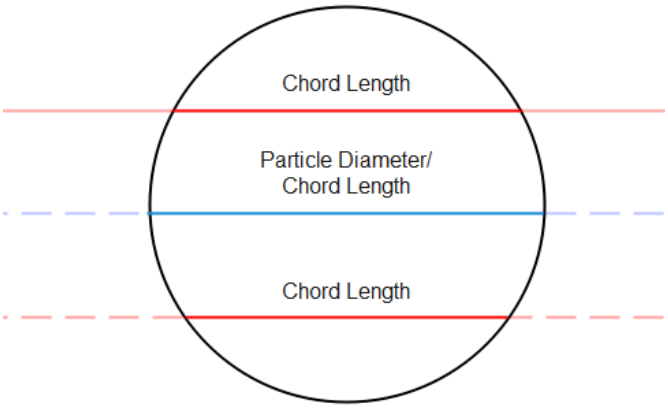

Figure 1-4: Spherical particle depicting both chord lengths and particle diameter. Chord length is the distance between any two points in the particle.

The chord length, however, could represent the line between any two points on the particle, making it not directly relatable to the particle size. This effect is especially pronounced in non-spherical needle-shaped particles where the orientation of the particle and the beam plays a crucial role in detecting the chord length (Figure 1-5) (Silva et al., 2013). The chord length is, therefore, a function of particle size and shape. Various attempts to relate the chord length to PSD have been made to varying levels of accuracy and repeatability (Li et al., 2006).

Feret's diameter is the distance between two parallel tangents at a given angle. This diameter is typically represented as a range of diameters, including the maximum (F_{max}) and minimum (F_{min}) (Rhodes, 2008). Similar to chord length, Feret's diameter (Figure 1-6) is heavily influenced by the direction of measurement and the orientation of the particles.

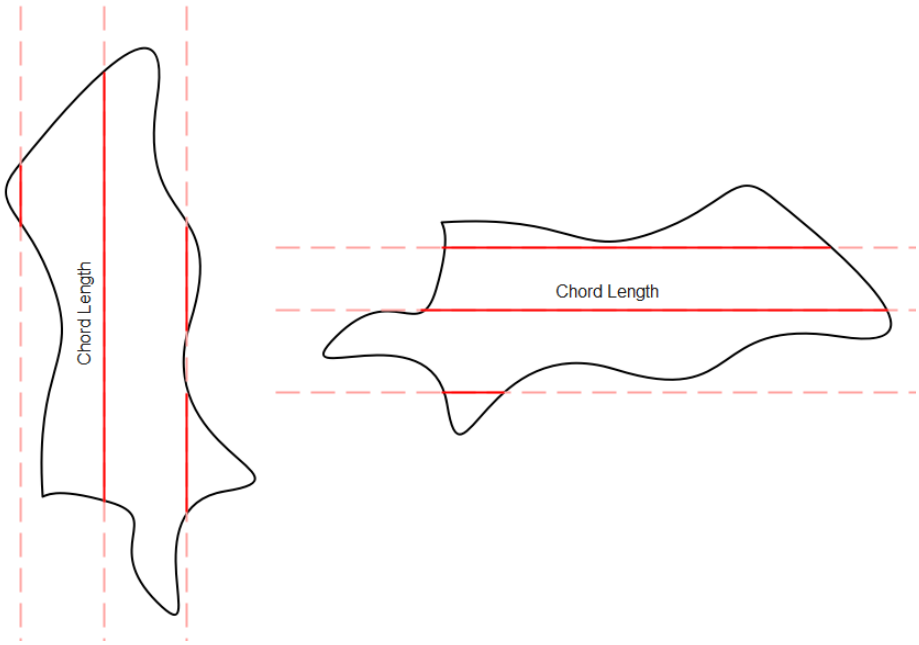

Figure 1-5: Chord lengths in non-spherical particle indicating the potential errors arising from both particle shape and orientation.

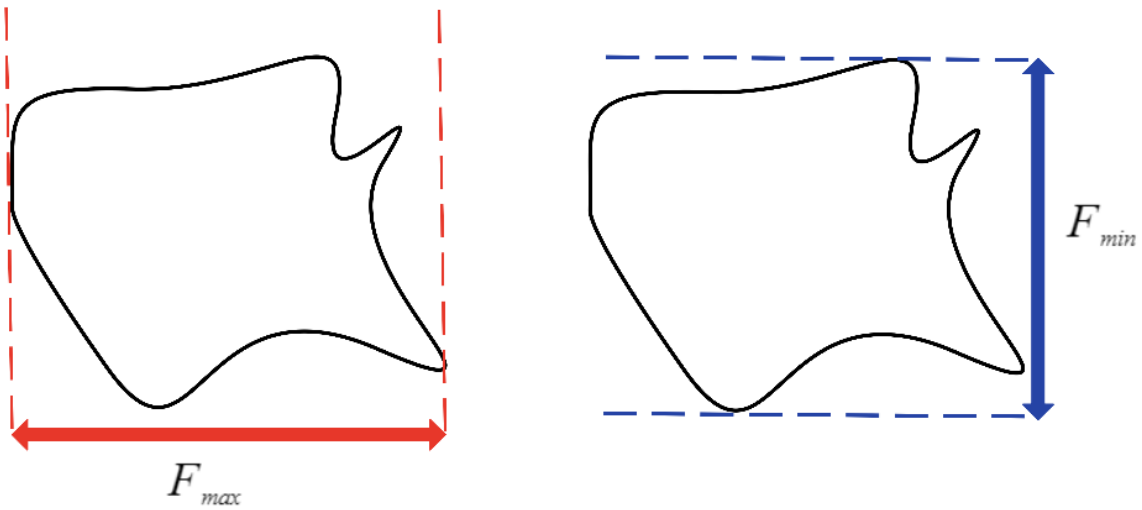

Figure 1-6: Diagram depicting the Feret diameter in an irregularly shaped particle.

Characterising a single particle does not capture the size variance within the bulk material. To this end, a population of particles are typically considered, which gives a particle size distribution (PSD). The two primary methods of displaying PSD are frequency distribution and cumulative distribution, with the latter being the integral of the former (Rhodes, 2008). From these representations of the particle size, average values representing the bulk material can be obtained. These average values are typically

communicated as percentiles (e.g. d_{10}: 10% , d_{50}: 50%, d_{90}: 90% where X% or particles are smaller than the reported diameter).

To summarise, particle or domain size characterisation proves challenging due to various techniques and approaches. Current approaches range from area or volume equivalent diameters (Laser diffraction or DLS) to chord length and Feret's diameter (FBRM). However, for practical application, single particle analysis is insufficient, necessitating the need to describe particle populations in the form of PSD.

1.3.2 Optical Microscopy

Optical microscopy is currently considered the most robust and dependable technique for analysing particles larger than 1 µm in the pharmaceutical industry (Rawle, 2014; Shekunov et al., 2007). The technique employs visible light to magnify particles, allowing for detailed image analysis of both particle size (> 1 µm) and shape. This section explores the advantages and disadvantages of the various forms of optical microscopy and image analysis.

The primary advantage of the technique lies in its high-resolution, non-destructive surface analysis of particles (Grubbs et al., 2021), enabling the analysis of both particle size and shape (Bosquillon et al., 2001; Grubbs et al., 2021; Shekunov et al., 2003, 2007).

However, despite its robustness, the various forms of optical microscopy are not without limitations. The main limitation of the technique is the application of image thresholding to circumvent the detection of particle clusters. This image analysis requires operator oversight and careful consideration to ensure consistent data analysis (Beekman et al., 2005; Rawle, 2014; Shekunov et al., 2007). Most crucially, however, is the limitation that it can only analyse the surface of compacted granular samples, thus requiring destructive sample preparation

methods to probe the core of granular compacts in the pharmaceutical industry (Bosquillon et al., 2001; Grubbs et al., 2021; Shekunov et al., 2003).

Historically, the high computational demands for processing lead to slow analysis time (Grubbs et al., 2021; Shekunov et al., 2007) due to the reliance on image processing software. Recent advancements in image processing have alleviated some of the pressure on computation; however, further optimisation is required to improve accuracy and reduce dependence on the operator. Additionally, ensuring a representative sample is both time and resource-intensive sampling, especially when analysing heterogeneous samples (Shekunov et al., 2003, 2007). Finally, particle orientation and agglomeration can prevent accurate quantification of particle size, leading to the need to employ other techniques, such as laser diffraction.

In conclusion, optical microscopy remains the gold standard for offline/in-process particle size and shape analysis in the pharmaceutical industry. The technique boasts high-resolution, non-destructive surface analysis of particle size and shape. However, its time and resource-intensive sampling, as well as requiring operator oversight for the image thresholding and analysis, must be considered (Table 1-1).

1.3.3 Laser Diffraction

Laser diffraction is a powerful and widely used technique for non-destructive particle size analysis of powders (0.001-2000 µm) (Ma et al., 2000). By passing a powder sample through the beam and analysing the scattered light as a function of the scattering angle, the technique provides information on particle size based on Mie or Fraunhofer diffraction theory (Rawle, 2001; Silva et al., 2013). Laser diffraction allows for the rapid and non-destructive analysis of

particle sizes of powders. This section discusses some limitations of the technique, specifically concerning the measurement of small particles (< 50 μm), non-spherical particles and the assumptions in the underlying analysis.

One major limitation of the technique arises from the need for accurate knowledge of the material refractive index (RI), especially for the measurement of smaller particles (< 50 um) (Beekman et al., 2005; Shekunov et al., 2007). The challenge presented stems from the laser's wavelength coupled with the method's reliance on Mie theory, which necessitates particle sizes akin to the wavelength for optimal performance. Laser diffraction instruments opt for red lasers, typically around ~ 630 nm, primarily due to their cost-effectiveness. However, other more expensive instruments may employ blue-violet (~ 400 nm) lasers with smaller wavelengths. Inaccuracies in the RI lead to substantial discrepancies in the measured particle size. To ensure reliable and meaningful results, rigorous calibration and precise knowledge of the RI is required.

Higher concentration samples can cause light obscuration, resulting in the overestimation of particle size. This phenomenon occurs due to increased light scattering and interference from neighbouring particles in bulk, reducing the reliability of the measurement. Addressing this limitation requires care to be given to the sample preparation methods to mitigate the effects of higher-concentration samples.

The technique relies on various assumptions for particle size analysis, which only holds in some practical applications (Rawle, 2001; Silva et al., 2013). The assumptions include considering all scattering particles are opaque, that light is only scattered at narrow angles, allowing for detection and assuming that the scattering magnitude for each particle is equal

(neglecting successive scattering events). Finally, laser diffraction is limited to the analysis of powders and cannot be applied to monitoring particle size changes in granular compacts.

In conclusion, laser diffraction is a powerful tool for the non-destructive analysis of particle size in powders (Table 1-1). However, it is essential to consider measurement limitations, including light obscuration from high-concentration samples and the various assumptions underpinning the analysis. Addressing these limitations requires rigorous calibration, improved modelling techniques, and the evaluation of the assumption employed.

1.3.4 Focused Beam Reflectance Measurement

FBRM is a powerful technique currently employed for monitoring chord particle lengths (0.1-1000 µm) in suspension in industries including pharmaceuticals, paints, and emulsions in real-time (Alshihabi et al., 2012; Coutant et al., 2010; Dave et al., 2017; Hermanto et al., 2010; Kail et al., 2009; Kumar et al., 2013). The technique detects backscattered light from suspended particles to measure the chord length distribution (CLD) (Hermanto et al., 2010; Kail et al., 2009; Kumar et al., 2013).

The technique offers multiple advantages for monitoring the CLD of particles in suspensions. The first primary advantage is non-destructive in-situ measurements, allowing for real-time monitoring of CLD during manufacturing. Finally, as it directly calculates the CLD, it does not require time and resource-consuming chemometric modelling.

Nonetheless, FBRM is hampered by numerous limitations primarily related to the relationship between chord length and particle size (Hermanto et al., 2010; Kail et al., 2009; Kumar et al., 2013; Silva et al., 2013). The chord length is calculated based on the reflection of light off a particle from a circulating beam, using the reflection time and scanning speed (Alshihabi et

al., 2012; Coutant et al., 2010; Dave et al., 2018; Hermanto et al., 2010; Kail et al., 2009; Li et al., 2006; Silva et al., 2013). As discussed previously, however, the chord length could represent the line between any two points on the particle, thus reducing the accuracy of the measurement, especially in non-spherical needle-shaped particles where the orientation of the particle and the beam plays a crucial role in the detection of the chord length (Silva et al., 2013).

Additionally, some practical issues, such as particle adherence to the analysis window leading to errors in analysis, further limit the technique (Kumar et al., 2013). This section explores the benefits of FBRM for real-time monitoring as well as discussing the various limitations of the technique.

Furthermore, there are practical limitations to the technique, specifically, adherence of particle to the probe window (Kumar et al., 2013). As the technique requires the emersion of the FBRM probe into the suspension, depending on the cohesive nature of the materials, adherence of particles to the probe is possible. This is known to cause multiple counting of the adhered particles thus adding bias to the data (Kumar et al., 2013). Finally, the requirement for materials in suspension prevents its application to the measurement of solid materials, specifically for OSDs (Silva et al., 2013).

These limitations however do not detract from the technique's ability for non-destructive, in-situ and real-time monitoring capability of CLD of particles in suspension (Table 1-1). For the sample which it is applicable to, FBRM is a powerful PAT for the indirect monitoring of PSD (Dave et al., 2018; Hermanto et al., 2010; Kail et al., 2009; Silva et al., 2013).

1.3.5 Near-infrared Spectroscopy

Near-infrared spectroscopy (NIRS) is a technique currently employed in the pharmaceutical industry for the non-destructive analysis and real-time monitoring of blend and content uniformity including particle size analysis (1-300µm) (Bär et al., 2018; Higgins et al., 2003; Pasikatan et al., 2001; Pauli et al., 2019; Stojanovska Pecova et al., 2021). It is currently employed in granulation, blending, and tabletting processes, providing valuable insights into the manufacturing process (Pauli et al., 2019).

The primary advantage to NIRS is its ability to non-destructively and contactless analyse sample in the process allowing for real-time monitoring, providing an invaluable PAT during the manufacturing process (Higgins et al., 2003; Pasikatan et al., 2001; Pauli et al., 2019). Additionally, its versatility, requiring little sample preparation and allowing for the analysis of a wide range of samples from powders and granules to liquids provides a distinct advantage.

Another advantage of NIRS is its ability to indirectly monitor particle size changes through chemometric modelling and calibration (Bär et al., 2018; Challa & Potumarthi, 2013; Pauli et al., 2019; Stojanovska Pecova et al., 2021). This is achieved through the establishment of correlations between NIR spectra and material properties, such as particle size, allowing for prediction through the application of various calibration algorithms such as partial least square (PLS) (Stojanovska Pecova et al., 2021). However, such algorithms require training data sets typically obtained from analogous techniques such as laser diffraction, to allow for property prediction in unknown samples solely based on their NIR spectra.

Despite the advantages, NIRS is hampered by various limitations. The penetration depth of the technique is in the order of a few millimetres (Pasikatan et al., 2001), thus limiting its

capabilities to surface or near-surface analysis. Additionally, the development of high quality chemometric models and calibrations consume significant resources including time and materials (Challa & Potumarthi, 2013). Calibration in NIRS requires development of chemometric models that relate spectral information with material, such as chemical composition, concentration, or physical characteristics such as particle size. These models are developed using various mathematical algorithms and statistical techniques, including partial least squares regression (PLSR) or principal component analysis (PCA).

In conclusion, NIRS is a compelling PAT for the non-destructive and contactless in-line analysis of particle or domain size in granular compacts. However, there are various disadvantages to the technique (Table 1-1) hindering its applicability namely indirect measurement and the need to resource-intensive chemometric modelling.

Table 1-1: Table depicting the various advantages and disadvantages of current PAT techniques for the monitoring and analysis of particle size.

TECHNIQUE	NIR	FBRM	OPTICAL MICROSCOPY	LASER DIFFRACTION
ASSUMPTIONS	Constant Concentration	Particle Sphericity, Constant Concentration	N/A	Opaque Particles, Narrow Scatter Angle
NON-DESTRUCTIVE	✓	✓	✓	✓
IN-SITU/IN-LINE	At-line/in-line	At-line/In-line	At-line/In-line	At-line/On-line
MEASUREMENT	Surface/Volume	Suspension	Surface	Surface/Near Surface
MEASUREMENT OF PARTICLE SIZE	Indirect 1-300µm	Indirect 0.1-1000 µm	Direct >1 µm	Direct 0.001-2000 µm
ADVANTAGES	non-destructive, in-line monitoring	non-destructive, in-line monitoring	non-destructive In-line monitoring	non-destructive, at-line monitoring
DISADVANTAGES	Penetration Depth, Indirect measurement Model Complexity	Indirect Measurement, Practical Challenges	Computationally Demanding, Particle Orientation Error	Light Obscuration, Inaccurate Analysis of Small Particles

1.3.6 Summary

To summarise, particle size has a pivotal role in the CQA of final product across industries, particularly in the pharmaceutical industry. Changes in particle size affects both dissolution rate (Figure 1-7) and compound stability of the product. PAT are therefore essential for monitoring particle size to ensure product quality and efficacy is maintained. There are various technologies employed in the pharmaceutical industry currently to monitor and detect any changes in particle size. However, these techniques exhibit significant limitations either from the eligible sample preparation methods to being offline or providing only indirect measurements of particle size (CLD etc) (Table 1-1).

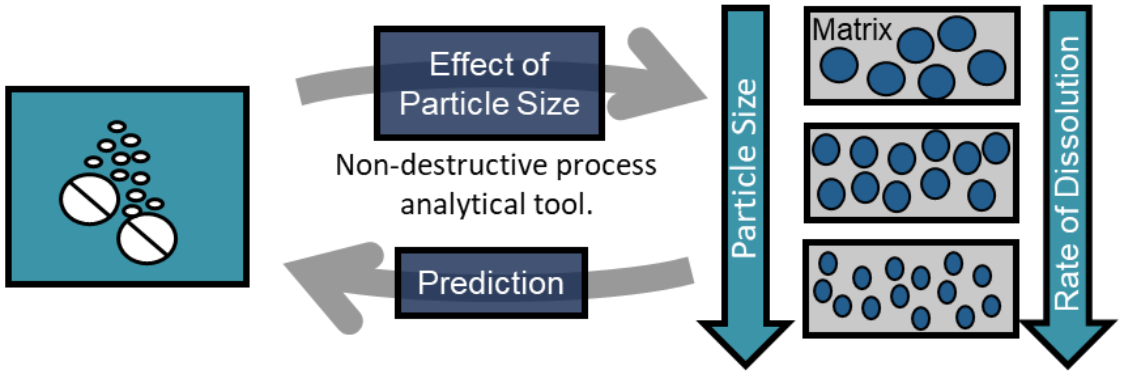

Figure 1-7: A novel non-destructive, in-situ PAT of the monitoring of particle size is required to ensure the maintenance of product quality and efficacy.

To respond to the demand for non-destructive in-situ analysis, a relatively new technique, terahertz time-domain spectroscopy (THz-TDS) has been explored in the pharmaceutical industry for the analysis of various CQA but also exhibits significant promise for particle size analysis in granular compacts during the manufacturing process. THz-TDS enables non-destructive, volume-based analysis, thus showing the required characteristics for a potent PAT for the monitoring of various CQA as well as the potential for the monitoring of particle size in the pharmaceutical industry.

1.4 Terahertz Time-Domain Spectroscopy

1.4.1 Introduction

Terahertz (THz) technology, specifically THz-TDS refers to a band of the electromagnetic spectrum between the microwave and infrared regions (Zeitler, 2016). THz technology allows for the study of various intermolecular and intramolecular vibrational resonances through THz radiation (Figure 1-8).

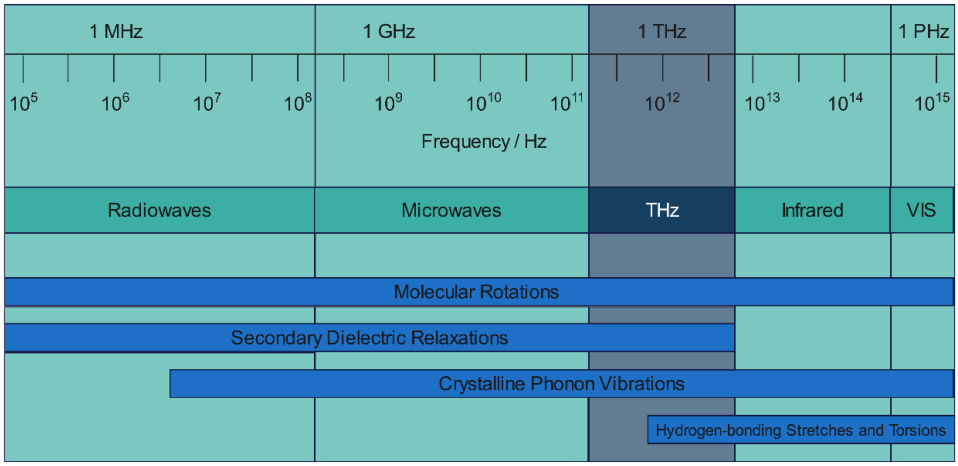

Figure 1-8: Diagram showing the different regions of the electromagnetic spectrum as well as the different physical properties that they couple to.

Notably, the radiation has shown partial penetration through most non-conducting materials, such as textiles, wood, plastics, and ceramics (Naftaly et al., 2019; Naftaly & Miles, 2005, 2007; Zeitler, 2016; Zeitler & Shen, 2012a). Additionally, the technique has been of significant interest in various industries especially in polymer and pharmaceutical applications. This interest is due to the use of coherent THz radiation to obtain both the RI and loss coefficient simultaneously (Bründermann et al., 2012; Stranzinger, Faulhammer, Li, Dong, Khinast, et al., 2019; Stranzinger, Faulhammer, Li, Dong, Zeitler, et al., 2019). In the polymer and plastic industry, THz-TDS has been proven to enhance product quality while reducing material waste during the manufacture of components and appliances (Engelbrecht et al., 2019; Naftaly et

al., 2019; Sommer et al., 2016a). The pharmaceutical industry has found applications for THz-TDS in the determination of porosity in pharmaceutical compacts (Bawuah et al., 2016, 2018; Bawuah, Markl, Farrell, et al., 2020) and the identification of polymorphic forms in both granular compacts and powder (Silva et al., 2017; Zeitler & Shen, 2012a). These applications require the accurate extraction of both the RI and loss coefficient to ensure precise material characterisation and successful implementation to industrial settings.

To summarise, THz-TDS exhibits significant potential in a range of industries due to its ability for non-destructive, volume-based analysis. Simultaneous extraction of the RI and loss coefficient can provide pivotal information on material properties. With these advantages, THz-TDS is an excellent candidate for the in-situ monitoring of particle size during the manufacturing process. Allowing for the increased efficiency in both formulation development and the manufacturing process for the pharmaceutical sector.

1.4.2 Extraction of RI & Loss Coefficient

The potential of THz-TDS in enabling advanced material characterisation necessitates the accurate analysis and interpretation of experimental data. One fundamental optical parameter that can be investigated with THz-TDS is the RI of a material. A comprehensive understanding of RI is crucial for characterisation of the composition and structure of complex materials.

Another crucial optical parameter obtained from THz-TDS analysis is the loss coefficient which is valuable for material characterisation and the determination of dielectric properties, through which diverse applications across various industries have developed.

A critical advantage of THz-TDS, due to its use of coherent detection, is the simultaneous determination of both the real RI and the loss coefficient. To achieve this in a transmission setup, measurement of a reference (empty purged chamber) and sample pulse (sample placed perpendicular, i.e., normal incidence, to the beam) are conducted in the time domain. Application of Fast Fourier Transform converts the data into the frequency domain facilitating subsequent analysis.

The refractive ($n(\upsilon)$) index can then be calculated using the following equation:

$$n(\upsilon) = 1 + \frac{(\phi_{\mathrm{s}}(\upsilon) - \phi_{\mathrm{r}}(\upsilon))c}{2\pi\upsilon \mathrm{L}} \tag{4}$$

Where:

- $n(\upsilon)$ is the frequency dependent real RI.
- $\phi_s(\upsilon)$ denotes the frequency dependent sample phase.
- $\phi_r(\upsilon)$ is the frequency dependent reference phase.
- c is the speed of light in a vacuum.
- υ is the frequency.
- L is the sample thickness.

The loss coefficient represents attenuation of the electromagnetic wave as it propagates through the material. The attenuation is caused by refraction at the interface between materials of differing refractive indices as well as transmission through a given material. The

Fresnel coefficients of reflection ($R(\upsilon)$) and transmission ($T(\upsilon)$) describe these processes, expressed by the following equations:

$$R(\upsilon) = \frac{(n(\upsilon) - 1)^2}{(n(\upsilon) + 1)^2} \tag{5}$$

$$T(\upsilon) = 1 - R(\upsilon) = 1 - \frac{(n(\upsilon) - 1)^2}{(n(\upsilon) + 1)^2} \tag{6}$$

Relating the attenuation of light through the material to the absorption coefficient (α_{abs}) as gives rise to the following equation:

$$\frac{I}{I_{\mathrm{o}}} = T(\upsilon)^{\mathbf{2}} exp(-\alpha_{\mathrm{abs}} L) \tag{7}$$

Where:

- I is the detected intensity.
- I_{o} is the initial intensity.
- α_{abs} is the absorption coefficient.

The loss coefficient (α_{loss}) can then be obtained by substitution of the transmission coefficient ($T(\upsilon)$) into Equation 7 as:

$$\alpha_{\mathrm{loss}}(\upsilon) = -\frac{2}{L} \ln\left(\left(\frac{n^2 + 1}{(n(\upsilon) + 1)^2}\right)\frac{E_{\mathrm{sam}}}{E_{\mathrm{ref}}}\right) \tag{8}$$

Where:

- E_{sam} is the sample electric field.

- E_{ref} is the reference electric field.

Furthermore, the loss coefficient can be employed to determine the extinction coefficient as follows:

$$K(\upsilon) = \frac{\alpha_{\mathrm{loss}}(\upsilon)c}{4\pi\upsilon} \tag{9}$$

The real $(\varepsilon(\upsilon)')$ and imaginary $(\varepsilon(\upsilon)'')$ parts of the dielectric constant (permittivity) can be subsequently obtained from the extinction coefficient and the refractive index in the following equations (Naftaly, 2014):

$$\varepsilon(\upsilon)' = n(\upsilon)^2 - K(\upsilon)^2 \tag{10}$$

$$\varepsilon(\upsilon)'' = 2n(\upsilon)K(\upsilon) \tag{11}$$

The full complex dielectric constant ($\varepsilon(\upsilon)$) can then be determined using:

$$\varepsilon(\upsilon) = \varepsilon(\upsilon)' - j\varepsilon(\upsilon)'' \tag{12}$$

Finally, the material conductivity ($\sigma(\upsilon)$) can be determined via the imaginary part of the complex dielectric constant where ε_0 is the vacuum permittivity.

$$\sigma(\upsilon) = \varepsilon''(\upsilon)2\pi\upsilon\varepsilon_0 \tag{13}$$

To summarise, THz-TDS enables the simultaneous extraction of both the real RI and loss coefficient. These optical properties provide valuable insights into material properties allowing for advanced material characterisation and accurate determination of dielectric properties.

1.4.3 Scattering in the Terahertz Domain

Scattering occurs when light travels through an inhomogeneous medium with a varying RI (Newton, 2013; Twersky, 1964; Xu, 2015), and results in transmission loss. The magnitude of scattering loss depends on the wavelength of light relative to the size of the scattering centres and on the differences in the RI. The ratio between wavelength and the size of scattering particles determines scattering behaviour and the choice of model that can be employed to quantify scattering. In cases where the distance between the scattering centres is comparable to the wavelength of the propagating light, Mie theory is applicable (Garet et al., 2014).

The observed loss coefficient (α_{loss}) is the sum of absorption (α_{abs}) and scattering contributions (α_{scatt}):

$$\alpha_{\mathrm{loss}} = \alpha_{\mathrm{abs}} + \alpha_{\mathrm{scatt}} \tag{14}$$

Therefore, if the absorption of the solid medium is known, then the scattering component can be obtained by simple subtraction.

Scattering in THz-TDS measurements has been previously investigated by both empirical fitting (Shen et al., 2008) and through a first principles scattering model originally derived by Raman (Clarke, 1968; Franz et al., 2008; Raman, 1949). Shen et al. modelled the loss spectra ($\alpha_{\mathrm{loss}}(\upsilon)$)

of granular compacts containing polyethylene powder and found that the spectra could be best modelled as a function of frequency (υ) using (Shen et al., 2008).

$$\alpha_{\text{loss}}(\upsilon) = B\upsilon^{A} \tag{15}$$

with A and B as fitting parameters. Numerous studies have utilised this model, including the non-destructive determination of tablet fragmentation during compaction (Skelbæk-Pedersen et al., 2020). Pederson et al. observed the fragmentation of various materials using THz-TDS combined with the model proposed by Shen et al. (Anuschek et al., 2023; Shen et al., 2008; Skelbæk-Pedersen et al., 2020). This approach, however, did not consider the effect of particle concentration and modelled the total loss coefficient (extinction) rather than the scattering contributions.

Franz et al. showed the application of a previously derived first principles model for determining scattering contributions to the loss coefficient. First proposed by Raman to describe the chromatic effects observed by Christiansen, it led to the development of the Christiansen model (Carlon, 1979; Clarke, 1968; Franz et al., 2008; Raman, 1949). This model required significant material knowledge, including the refractive indices of the suspension medium and scattering particle. Using these properties, the model could be fitted using two unknown parameters: the wavefront coverage by the scattering objects and the layer thickness (Clarke, 1968; Raman, 1949). Once fitted, Franz et al. could show the quantitative value of the estimated scattering contributions to the loss coefficient. The model, however, is predicated on several assumptions, such as neglecting the possibility of a photon encountering multiple scattering events during propagation through the sample. The model estimates the scattering from a single layer of particles and then estimates the total scattering

from the number of layers. This leads to a significant overestimation of scattering. Additionally, the original derivation was predicated on non-coherent analysis (i.e scattering events are independent of each other with regards to phase), which is false for THz-TDS.

However, the Christiansen model can also be effectively employed to manage asymmetric peak shapes (Franz et al., 2008). The model, despite its empirical nature, offers a simple means of understanding complex asymmetry in peak profiles, thereby facilitating accurate data analysis and interpretation when such features occur. In the context of this project the absence of such features renders this application irrelevant. Due to the various assumptions discussed and the absence of asymmetric features, the Christiansen scattering model was not considered for application to this project.

Previous investigations into the effect of an inhomogeneous distribution of particles in paint emulsions have been of significant interest in the past few decades. Fitzwater et al. derived a theoretical model describing light scattering based on Mie theory. They attempted to account for the concentration of inhomogeneities (J. C. Auger & Stout, 2012, 2013) by assuming a spherical area around the scattering particle dependent on the difference in the RI between the matrix and emulsion particles as well as on the wavelength (J. C. Auger & Stout, 2012). As particle concentration increases, the interparticle distance decreases leading to the saturation of scattering contributions due to ballistic vs non-ballistic propagation of photons through the media (Chapter 4).

Latimer et al. (Latimer & Wamble, 1982) employed Mie theory to model the transmission loss in granular compacts and investigate its relationship with particle size and concentration. The study revealed that scattering does not increase linearly with concentration; the scattering

particles are closer to each other at higher concentrations, causing photons to travel ballistically through the scattering medium, reducing scattering efficiency. This behaviour leads to saturation and a subsequent fall in scattering. Furthermore, they suggested that the particle size is not expected to affect the scattering strength, as the total volume of scattering material remains constant. Latimer et al. also analysed experimentally cells containing known concentrations of latex spheres suspended in water, showing that the extinction coefficient increased before reaching saturation. However, they could not extract the scattering loss due to a lack of knowledge of the material absorption.

A study by Grinchuk et al. (Grinchuk, 2003) used diffuse reflectance measurements to determine scattering from a painted polyvinyl chloride board. The analysis showed saturation of scattering at higher concentration levels. They applied a percolation theory approach to explain this saturation as a function of the interparticle distance, clarifying that the original methods for the determination of scattering were developed with the scattering of a single particle in mind (Grinchuk, 2003). This model and experimental evidence of such phenomena have yet to be investigated for compacted materials using THz-TDS.

1.4.4 Effect of Dynamic Range on Spectral Measurements

The dynamic range (DR) of a spectrometer is a critical parameter which refers to the ratio between the highest and lowest measurable signal across a range of frequencies or wavelengths (Jepsen & Fischer, 2005). The DR (attenuated sample signal equal to the noise floor (Jepsen & Fischer, 2005)) of a measurement varies between different samples and instruments due to the differences in sample absorbance, preparation and the emitter/detector employed. In THz-TDS, the DR plays a pivotal role in both the accuracy and limitations of a given measurement, as it is a determining factor in the range of absorbance

values that can be detected reliably (Jepsen & Fischer, 2005; Naftaly, 2009; Withayachumnankul et al., 2007; Withayachumnankul, 2014).

Jepsen et al (Jepsen & Fischer, 2005) demonstrated a method for the quantitative determination of the dynamic range in THz-TDS to prevent the misinterpretation of experimental data when absorbance exceeds the maximum dynamic range (Jepsen & Fischer, 2005). The maximum measurable absorbance ($\alpha_{\max}$) is calculated using the following equation:

$$\alpha_{\max} = \frac{2 \ln\left[DR \frac{4n}{(n+1)^2}\right]}{L} \quad (16)$$

Where:

- $\alpha_{\max}$ is the maximum measurable absorbance.
- DR is the dynamic range of the instrument.
- n represents the RI of the sample.
- L denotes the sample thickness.

Accurate determination of the maximum measurable absorbance is crucial in THz-TDs measurements, as any data which exceeds the maximum absorbance is incorrect and can lead to erroneous conclusions (Jepsen & Fischer, 2005; Naftaly, 2009; Withayachumnankul et al., 2007; Withayachumnankul, 2014). From Equation 16 the maximum absorbance at a given frequency can be calculated and plotted to ensure correct interpretation of THz-TDS spectra (Figure 1-9).

In conclusion, the dynamic range and maximum measurable absorption is essential for accurate THz-TDS data analysis. Implementation of the method proposed by Jepsen et al. ensures the reliability and validity of THz-TDS data interpretation.

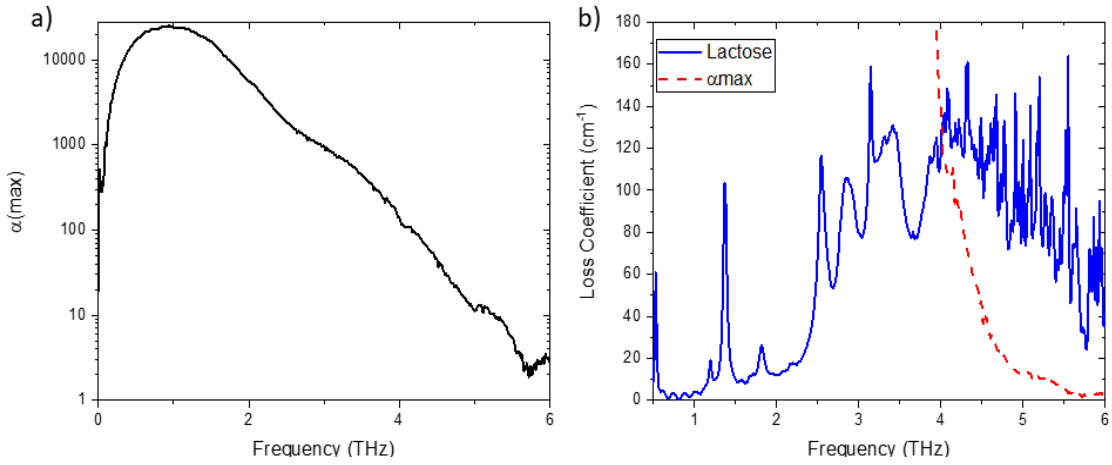

Figure 1-9: a) α-max showing the detectable limit of the spectrometer b) alpha-lactose monohydrate loss spectrum with α-max where any data beyond is not valid.

1.4.5 Effective Medium Theories

Effective medium theories (EMT) are models employed to approximate the behaviour of complex heterogeneous samples. These models provide valuable insights into material properties such as (but not limited to) effective RI, effective loss, and porosity in mixed media. Some of these models are widely utilised in material science to explore the behaviour of heterogeneous materials.

One such example are linear mixing models which operate by assuming homogeneity in mixed media and calculate material properties as the average of the constituent materials based on their volume fraction. Such theories, however, have accuracy limitations as they do not account for light-matter interactions such as multiple scattering. These models despite their limitations are valuable for providing approximate materials properties allowing for the development of fundamental understanding of physical phenomena. Examples of linear

mixing models for the estimation of material absorption (α_{abs}) and effective RI (n_{eff}) can be seen in the following equations (Chapter 4):

$$n_{\mathrm{eff}} = \sum V_{\mathrm{i}}\, n_{\mathrm{i}} \tag{17}$$

$$\alpha_{\mathrm{abs}} = \sum V_{\mathrm{i}}\, \alpha_{\mathrm{i}} \tag{18}$$

Where:

- I denotes volume fractions of constituent materials.
- nI_{i} represents RI of constituent materials.
- I_{i} is the absorption of constituent materials.

Another example of an EMT is the zero-porosity approximation (ZPA) which is employed to estimate sample porosity (f_{ZPA}) as can be seen in the following equation (Bawuah, Markl, Farrell, et al., 2020; Markl et al., 2018):

$$f_{\mathrm{ZPA}} = \frac{n_{\mathrm{extracted}} - n_{\mathrm{intrinsic}}}{1 - n_{\mathrm{intrinsic}}} \tag{19}$$

Where:

- $n_{\mathrm{intrinsic}}$ represents the intrinsic RI of the solid material.
- $n_{\mathrm{extracted}}$ is the measured RI.

The ZPA is particularly useful as a simple estimation of sample porosity or if the sample porosity is known, the intrinsic RI of a given formulation/mixture can be estimated. However, the model assumes that the sample has a constant thickness, and that the material density is known. The requirement of material density is to obtain a linear calibration curve to determine the intrinsic refractive index from nominal (dimensional) porosity measurements.

Another approach for the determination of porosity using THz-TDS involves employing the Bruggeman effective medium approximation, which follows from the Maxwell Garnett approximation (Bawuah, 2020). However, it should be noted that the applicability of the Maxwell Garnett method is confined to samples characterised by relatively small void spaces and is therefore not considered for this project. The initial form of the Bruggeman model, often termed the traditional Bruggeman effective medium theory, it is predicated on the assumption of pore sphericity and a sample porosity (f_{TB}) within the range of 10-15% (Bawuah, 2020). This variant of the Bruggeman model can be expressed as:

$$f_{TB} = \frac{1}{1 - \left(\frac{1 - n^2_{\text{extracted}}}{1 + 2n^2_{\text{extracted}}}\right)\left(\frac{n^2_{\text{intrinsic}} + 2n^2_{\text{extracted}}}{n^2_{\text{intrinsic}} - n^2_{\text{extracted}}}\right)} \tag{20}$$

The second Bruggeman variant employed for the determination sample porosity is the anisotropic Bruggeman effective medium theory (f_{AB}) as seen in equation 32. Unlike the traditional model, this variant incorporates a depolarisation constant (g), offering insights into pore morphology beyond spherical assumptions (where g = 1/3). Nevertheless, the current assumption that scattering contributions are negligible poses a challenge to EMT. As shown in Chapter 5, such scattering contribution does have an impact on the extracted refractive index.

$$f_{AB} = \frac{1}{1 - \left(\frac{1 - n^2_{\text{extracted}}}{1 + g n^2_{\text{extracted}}}\right)\left(\frac{n^2_{\text{intrinsic}} + g n^2_{\text{extracted}}}{n^2_{\text{intrinsic}} - n^2_{\text{extracted}}}\right)} \quad (21)$$

To summarise, EMT, play a vital role in the estimation of material properties in mixed media. While the models have limitations, they remain powerful tools for the analysis of composite materials allowing for the development of novel applications.

2 Aims & Objectives

This thesis aims to investigate the scattering of terahertz radiation in single- and multi-component powder compacts and the applications of terahertz time-domain spectroscopy for particle size estimation in OSD. This body of work can be separated into three objectives (Figure 2-1), described below:

- **To develop and fabricate samples allowing for the isolation of particle size and concentration of spherical particles in a two-component matrix.** Polymer pellets were fabricated using borosilicate microspheres suspended in a PTFE powder matrix. The blends were compacted at a pressure specially chosen to minimise samples porosity, allowing for the isolation of particle size and concentration effects. Ten pellet batches of five particle size distributions at six concentration levels were fabricated. The chapter discusses the development of the sample fabrication procedure and the reasons for the chosen materials.

- **Develop a fundamental understanding of the effect of particle size and concentration on THz-TDS scattering.** This objective is addressed by investigating the effect of both particle size and concentration on THz-TDS scattering and RI using the previously fabricated polymer samples. An experimental fitting model first developed by Shen et al. is employed to determine the fitting coefficients dependence on particle size and concentration. A theoretical hypothesis is proposed to describe the trends observed based on the propagation of photons through a mixed medium.

- **Apply the newly developed understanding to complex pharmaceutical compacts to estimate particle size.** Complex pharmaceutical compacts consisting of multiple excipients and an API compacted at various pressures are analysed. It was found that API agglomeration was present at two of the three particle sizes analysed. Using the knowledge from the previous objective, power law fitting was applied. The fitted coefficient was plotted against near-infrared chemical imaging (NIR-CI) mean particle size and was found to follow a linear trend. This study demonstrated the applicability of THz-TDS to non-destructively estimate particle size changes with the aid of a calibration curve.

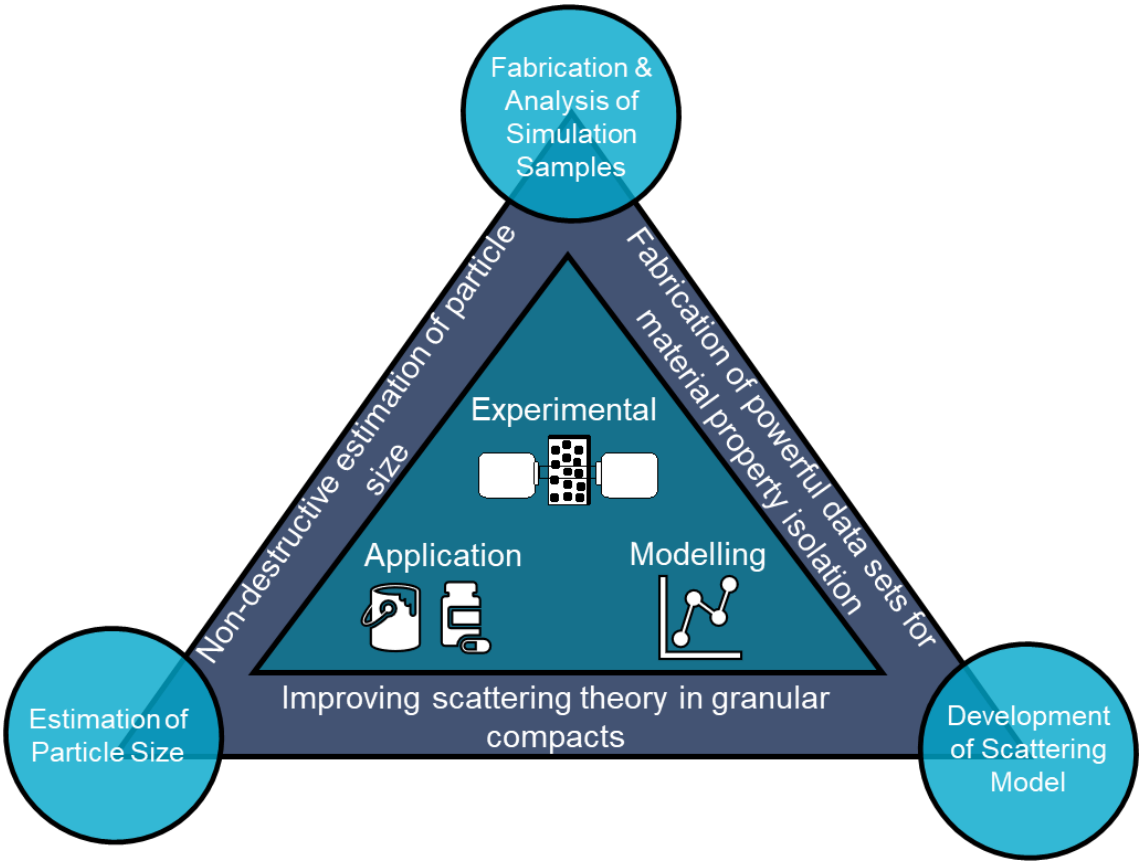

Figure 2-1: Diagram depicting the vision for the project. Beginning from the creation of a data set allowing for the isolation of particle size and concentration. Then applying this data to improve the fundamental understanding of scattering in granular compacts before using this newfound understanding in more complex compacts provided by the pharmaceutical industry.

3 Polymer Pellet Fabrication for Accurate THz-TDS Measurements

3.1 Chapter Summary

This chapter discusses the steps to determine the matrix material utilised in microsphere compacts. Matrix material was chosen to ensure accurate measurements and to isolate chosen properties/characteristics such as concentration and particle while minimising sample porosity. This chapter is based on the following publication:

> K. N. Murphy, M. Naftaly, A. Nordon, and D. Markl, "Polymer Pellet Fabrication for Accurate THz-TDS Measurements," Appl. Sci., vol. 12, no. 7, p. 3475, 2022, doi: 10.3390/app12073475.

Keir N Murphy (Doctoral Candidate) contribution to the peer-reviewed paper:

a. Responsible for the entire experimental work and data analysis that includes the design of the experimental procedure, creation and subsequent analysis of all samples and presented data.
b. Wrote the entire manuscript and implemented any corrections and comments provided by the co-authors.

3.2 Introduction

In THz-TDS, highly absorbing materials, such as many pharmaceutical drug substances, have strong THz absorption, making transmission measurements difficult and creating the need for dilution by a low-loss material such as a non-polar polymer (Smith & Arnold, 2011; Zeitler, 2016). The absorbing material must be mixed homogeneously with the polymer and then compacted at pressure to create a solid sample with minimal porosity. There have been various applications for this method of sample preparation such as the dilution of active pharmaceutical ingredients, explosive material, and biological samples (Özer et al., 2014; Pierno et al., 2013; Puc et al., 2018). Several sample properties can be a potential source of error in THz-TDS analysis, with the most critical attributes being sample porosity, uniformity of sample thickness, surface roughness and structural integrity.

Sample porosity must be minimised as it affects the accuracy of the RI obtained from terahertz measurements (Bawuah, Markl, Farrell, et al., 2020; Bawuah, Markl, Turner, et al., 2020; Markl et al., 2017, 2018; Markl, 2017; Naftaly et al., 2020; Withayachumnankul, 2014). Porosity refers to the volume ratio of material to void space in the pellet. The inclusion of air in a compact lower the measured RI (Markl et al., 2018).

Variations in pellet thickness and surface planarity can degrade the accuracy of the extracted optical constants. Sample thickness is used in the extraction of the RI and thus is a potential source of error (Withayachumnankul et al., 2007; Withayachumnankul, 2014). In the case of pellets, however, it is well known that pellets experience material- and pressure-dependent axial relaxation, leading to a change in sample thickness and, in some cases, to porosity (Bawuah, Markl, Farrell, et al., 2020; Bawuah, Markl, Turner, et al., 2020). The pellets,

therefore, must be allowed to relax for a certain period before THz analysis to minimise this source of error.

While sample porosity is minimised by increasing the applied pressure, high compaction pressure can cause cracking, lamination, and capping. Lamination and capping refer to the breakage of samples during ejection from the die, where capping is the breakage of the top and lamination is the splitting of the sample into layers (Bawuah, Markl, Farrell, et al., 2020; Bawuah, Markl, Turner, et al., 2020; Sun, 2005; C. Y. Wu et al., 2008). These defects can result in additional interfaces for refraction and reflection that produce variations between samples. Pellets should be created at a pressure that results in a pellet with a tensile strength of at least 2 MPa (Bawuah, Markl, Farrell, et al., 2020). This value is generally used in the pharmaceutical industry to ensure that pharmaceutical tablets have the required structural integrity to survive further handling and transport. In terms of THz-TDS, the sample also requires a certain strength to ensure that samples do not change structurally between fabrication and measurement.

This study investigates pellet preparation for accurate determination of RI and loss coefficient by THz-TDS. This study highlights the issues that must be considered in the fabrication of polymer pellets for THz-TDS analysis. These include compaction pressure required to minimise sample porosity, time needed for completion of axial relaxation and the effect of particle size. This study also indicates the suitability of both PTFE and high-density polyethylene (HDPE) as a polymer matrix for accurate determination of the RI and loss coefficient of the test material, respectively.

Pellets were created using two commonly used matrix materials: PTFE and polyethylene (PE) powders. A series of such pellets was created utilising a range of compaction pressures to investigate the optimal compaction setting to minimise porosity and to prevent pellet lamination or capping. The pellets were created in a well-controlled environment employing a compaction simulator (force- and displacement-controlled hydraulic press), and the results were compared to a standard hydraulic press with and without applying a vacuum. The pellets were monitored for axial relaxation before THz-TDS analysis to obtain both the pellets RI and loss coefficient, followed by breaking force testing to determine tensile strength.

3.3 Materials and Methods

3.3.1 Materials

Three pellet materials were used, PTFE (Sigma Aldrich, free-flowing) and two grades of HDPE powder differing in particle size (Sigma Aldrich, ultra-high molecular weight, surface-modified, powder). These materials (PTFE and HDPE) were chosen due to their extensive use in current sample preparation methods for the dilution of highly absorbing materials. The particle size and true density values of these materials are given in Table 3-1.

Table 3-1: Three polymer materials used for pellet fabrication, with particle size (d_{50}) and solid true density (pycnometric density) at 25°C provided by the material supplier.

Name	Material	Avg. particle size (μm)	Manufacturer true density (g/cm^{-3})
PTFE	PTFE	1	2.15
HDPE1	PE	42	0.94
HDPE2	PE	125	0.94

3.3.2 Methods

3.3.2.1 Sample Preparation

The study analysed pellets fabricated from PTFE and two grades of HDPE. The polymer materials were compacted using a compaction simulator (HB50, Huxley-Bertram Engineering, Cambridge, UK; London, UK) or a standard hydraulic press (SGS 10 TON, Hydraulic Shop Press SHBP10M, Derby, UK) with and without the application of a vacuum. Batches of ten plane parallel pellets were created for each polymer material with a diameter of 9 mm and a thickness of approximately 1 mm. The compaction simulator applies a set force, F, to the die resulting in a pressure (MPa) dependent on the cross-sectional area of the cylindrical die, A:

$$P = \frac{F}{A} = \frac{m_{applied}\, g}{A} \tag{22}$$

With $m_{applied}$ and g defined as mass and gravity, respectively. For hydraulic presses, the applied force is typically given in terms of the applied mass, m_{applied} (tons; 1 t = 9.8 kN = 154 MPa for a pellet with a diameter of 9 mm)

The pellets made on the vacuum hydraulic press were compacted at two pressures (139 & 159 MPa) for each polymer material. A 1 min dwell time for the hydraulic press samples was used. These two pressures represent the commonly used compaction pressures (Zeitler, 2016) for hydraulic press sample preparation.

Seven compaction pressures (157, 235, 319, 352, 392, 436 and 478 MPa) were studied for each polymer material using the compaction simulator. The chosen pressure range on the compaction simulator begins at the typical compaction pressures used on hydraulic presses for sample preparation. The main benefit of the compaction simulator is the ability to have

greater control over various compaction properties such as the force applied to the powder as well as the dwell time and compaction profile used. In this case, a 15 s profile was utilised with a 5 s dwell time at maximum load.

3.3.2.2 True Density Measurements

The true density of all powder polymer materials was measured using a gas pycnometer (MicroUltrapyc 1200e, Quantachrome Instrument, Graz, Austria) using nitrogen gas. All measurements obtained were conducted in triplicate.

3.3.2.3 THz-TDS Measurements

THz-TDS measurements were conducted on a commercial system (TeraPulse Lx, Teraview), with a frequency (υ) resolution of 0.04 THz. All measurements were performed in a nitrogen-purged chamber. Sample thickness (L) was measured using a micrometer ($\pm\ 0.005\ mm$) prior to the TDS measurement and was used for the calculation of the frequency-dependent RI ($n(\upsilon)$) and loss coefficient ($\alpha(\upsilon)$). The frequency-domain field amplitude ($E(\upsilon)$) and phase ($\varphi(\upsilon)$) for the sample (sam) and reference (ref) pulse were obtained from the time-domain data by applying zero padding (next power of 2), apodisation (Hamming approximation) and fast Fourier transform (Jepsen, 2019; Jepsen et al., 2011; Neu & Schmuttenmaer, 2018). Then, ($n(\upsilon)$) and ($\propto (\upsilon)$) of each sample were calculated using the standard equations (Jepsen et al., 2011):

$$n(\upsilon) = 1 + \frac{(\phi_{\mathrm{sam}}(\upsilon) - \phi_{\mathrm{ref}}(\upsilon))c}{2\pi\upsilon \mathrm{L}} \tag{23}$$

$$\alpha_{\mathrm{loss}} = -\frac{2}{L}\ln\left(\left(\frac{n^2+1}{(n(\upsilon)+1)^2}\right)\frac{E_{\mathrm{sam}}}{E_{\mathrm{ref}}}\right) \tag{24}$$

3.3.2.4 Sample Porosity Analysis

The ZPA EMT was employed for porosity calculations (f_{ZPA}). ZPA was employed due to the simple and well controlled formulation allowing for a standard linear model to be used. ZPA uses the intrinsic RI ($n_{\mathrm{Intrinsic}}$) of the material (solid material) and the extracted RI ($n_{\mathrm{extracted}}$) to calculate sample porosity:

$$\mathrm{f_{ZPA}} = \frac{\mathrm{n_{extracted}} - \mathrm{n_{Intrinsic}}}{1 - \mathrm{n_{Intrinsic}}} \tag{25}$$

Unlike powders, literature values for PTFE do not typically account for compacted samples, therefore there is a clear need for experimental determination. The intrinsic refractive index ($n_{\mathrm{Intrinsic}}$) employed in the model refers to the refractive index of the powder in its solid state, which may differ from the bulk refractive index .The intrinsic RI value in this instance for PTFE was set to the highest RI extracted due to the RI being consistently higher than the literature value as would be expected for powder vs solid material.

This intrinsic RI was obtained for PTFE samples compacted at 159 MPa using the hydraulic press with a vacuum. It is assumed that the porosity of the PTFE samples is close to zero when the RI is maximised.

3.3.2.5 Axial Relaxation Measurements

Axial relaxation (r) was measured for pellets compacted at ~159MPa for all materials and compaction methods. Pellet thickness was measured using a micrometre ($\pm\, 0.005\, mm$) immediately after compaction, then one and four weeks after compaction. Using the

thicknesses measured one week (L_1) and four weeks (L_4) after compaction, the axial relaxation R was calculated as a percentage of the post-compaction thickness ($L_{(\mathrm{pc})}$).

$$r = \left(100 - \left(\frac{L_{(1,4)}}{L_{(\mathrm{pc})}}\right)\right) - 100 \tag{26}$$

3.3.2.6 Tensile Strength Measurements

The breaking force of each pellet was measured using a high-load hardness tester (Kraemer Elektronick HC6.2, Darmstadt, Germany). Using the extracted breaking force value, h, and sample diameter (d_s), the tensile strength, σ_t, for the pellets was then calculated:

$$\sigma_t = \frac{2h}{\pi d_s L} \tag{27}$$

3.3.2.7 Raman Spectroscopy

Transmission mode Raman spectroscopy was conducted employing a state-of-the-art Bruker Bravo Raman spectrometer (Billerica, Massachusetts, United States). Spectra was acquired within the spectral range of 400 to 3000 cm^{-1}, for both a PTFE pellet compaction at 392 MPA as well as a sample of extruded PTFE.

3.4 Results

3.4.1 Gas Pycnometery Measurements

Pycnometric density (ρ_{true}) for all polymer materials is presented in Table 3-2. The measured values were the same as those provided by the manufacturers, except for PTFE, which was lower.

Table 3-2 Solid true density of PTFE and the two HDPE grades. Measured values are the mean ± one standard deviation (n=3).

Name	Manufacturer True Density (g/cm^{-3})	True Density (g/cm^{-3})
PTFE	2.15	2.07 ± 0.01
HDPE1	0.94	0.96 ± 0.02
HDPE2	0.94	0.95 ± 0.01

3.4.2 Polytetrafluoroethylene

Full frequency spectra for both RI and loss coefficient for PTFE can be seen in Figure 3-1. It is evident at low frequencies that the PTFE pellets are in good agreement with the loss coefficient of solid material, whereas the RI is slightly higher. Oscillations in the pellet spectra are artefacts due to internal reflections within the sample, producing a Fabry-Perot effect. The oscillation period or free spectral range (FSR) is determined by the sample thickness and RI, given by (Duvillaret et al., 1996, 1999):

$$FSR = \frac{c}{2n_{\mathrm{extracted}}} \tag{28}$$

For subsequent analysis, mean values over a range (2.45-2.55 THz) were used due to the lack of spectral features and relatively high signal-to-noise ratio (SNR).

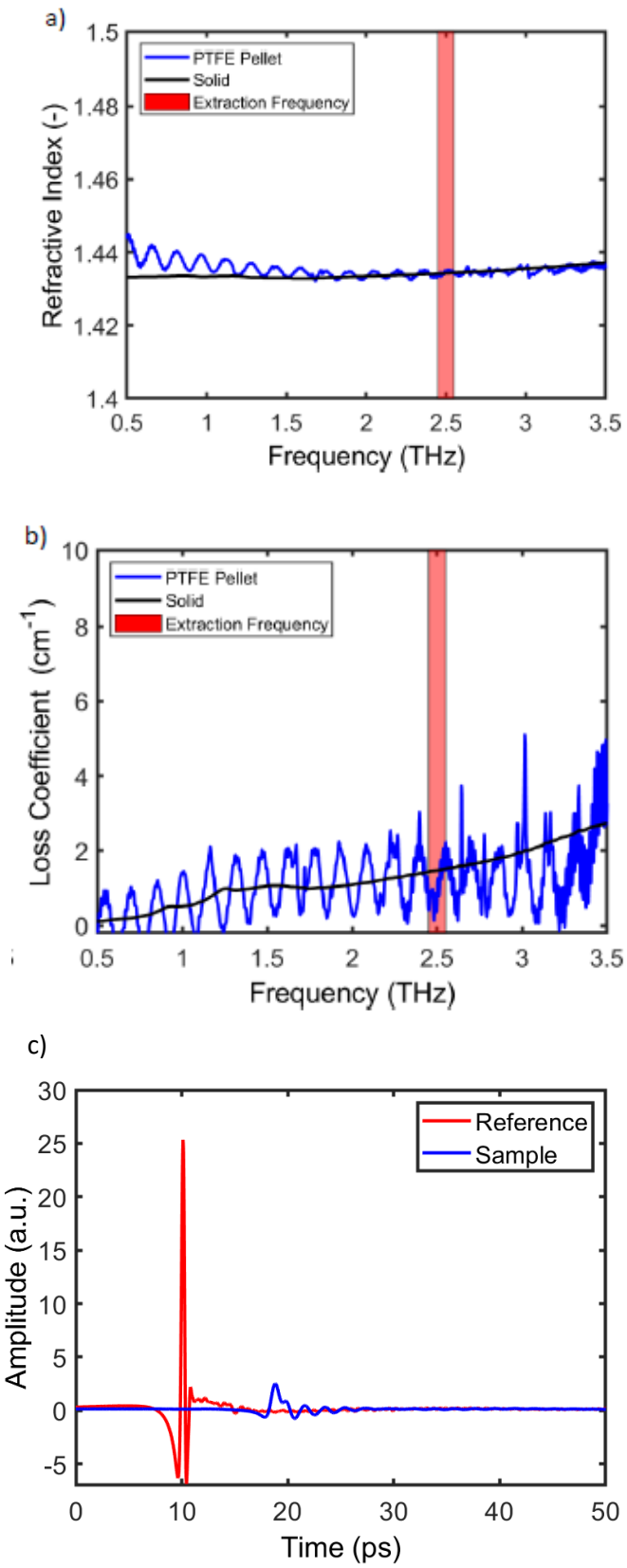

Figure 3-1: RI (a) loss coefficient (b) and time domain (c) spectra of PTFE pellets. Oscillations in spectra are artifacts due to internal reflections. Solid material was sourced from extruded PTFE. Frequency resolution of 0.04 THz.

Figure 3-2 presents the RI (a) and loss coefficient (b) of PTFE pellets compacted at various pressures (159, 235, 319, 352, 392, 436 and 478 MPa). The refractive indices of pellets made using the compaction simulator (Figure 3-2a)) are either in good agreement or slightly above the values in the literature, except for the pellets that were compacted at a pressure of 159 MPa. Consistently higher RI values suggest a difference in material density compared with the values in the literature (Busch et al., 2014; D'Angelo et al., 2014; Sommer et al., 2016b; Wietzke et al., 2011; Yamamoto et al., 2004). Raman spectra of the PTFE pellets and solid reference samples were acquired to determine whether a change in amorphous or crystalline character had occurred (Figure A-1(Appendix)); no such change was observed. Therefore, the increased RI is attributed to the different production methods used for the powder compared with that for the solid polymer.

The loss coefficient values for compaction pressures >350 MPa are within the reference ranges. It can also be observed that higher compaction pressures lead to more consistent loss coefficient values. The RI value at a compaction pressure of 159 MPa is significantly lower than expected and exhibits high variability across ten pellets. This lower RI suggests a large sample porosity created by inter-particle pores. These inter-particle pores reduce in size with increasing compaction pressure. The measured RI approaches the RI of the solid material as the porosity decreases with increasing compaction pressure. Evidence of surface defects can be observed in microscope images (Figure A-2(Appendix)). The high calculated standard deviation is due to cracks or surface defects in the samples produced at this lower pressure, which are particularly noticeable in those made using the compaction simulator. These defects cause inaccuracies in the determination of the calculated RI due to changes in beam path by

introducing an additional interface. The cracks in these samples also affect the loss coefficient, which is higher in samples compacted at lower pressures.

The samples fabricated using the hydraulic press with a vacuum had refractive indices either slightly above or in agreement with the values in the literature. Loss coefficient values were also in good agreement with the values in the literature. However, it should be noted that creating samples in such a die requires care when releasing the pressure to prevent sample cracking. The dwell time difference between the compaction methods must also be considered, as the hydraulic press had a larger dwell time than the compaction simulator, thus explaining the better performance at lower pressures. The increased loss coefficient for pellets produced at lower compaction pressures with the compaction simulator is driven by increased scattering from pores within the sample.

The hydraulic press without a vacuum performed well at 139 MPa, with RI and loss coefficient values either matching or slightly above literature values. However, the samples produced using a compaction pressure of 159 MPa have a significantly lower RI, suggesting either an increase in sample porosity or the inclusion of structural defects in the sample. These structural defects are also seen in the increased loss coefficient (Figure 3-2 b)).

The sample porosity for PTFE pellets produced using the compaction simulator and the hydraulic press at all compaction pressures is shown in Figure 3-2 (c). The ZPA was employed to calculate sample porosity from RI. An additional investigation into the sample porosity of PTFE pellets involved THz-TDS analysis of dry and paraffin oil-soaked pellets. The paraffin oil (RI = 1.475 (Naftaly, 2020)) will fill surface-connected pores and increase the RI due to decreased sample porosity. This investigation suggested minimal open (surface-connected)

pores (Figure A-3 (Appendix)) (Naftaly et al., 2020). As PTFE is opaque to visible light, microscope imaging can be deployed to identify pores close to the sample surface. Microscope imaging of PTFE samples compacted at >350 MPa showed minimal porosity (Figure A-2a) (Appendix)). Furthermore, due to the RI values matching or exceeding that of solid PTFE, it is clear that these pellets have close to zero porosity, indicating that PTFE is a suitable material for fabricating compressed pellets with minimal porosity at high pressure >390 MPa.

PTFE pellets fabricated in the compaction simulator and hydraulic press without a vacuum do not undergo significant axial relaxation one week after compaction (Figure 3-2 d)). Pellets fabricated in the hydraulic press with a vacuum (HPV) exhibit more significant axial relaxation between zero and one week after compaction. This increase in relaxation is potentially due to the post-compaction swelling of open pores. Therefore, due to the axial relaxation of PTFE pellets being negligible for those produced with the compaction simulator and the hydraulic press without a vacuum, it is clear that THz-TDS analysis can be conducted one week after compaction, allowing for repeated analysis.

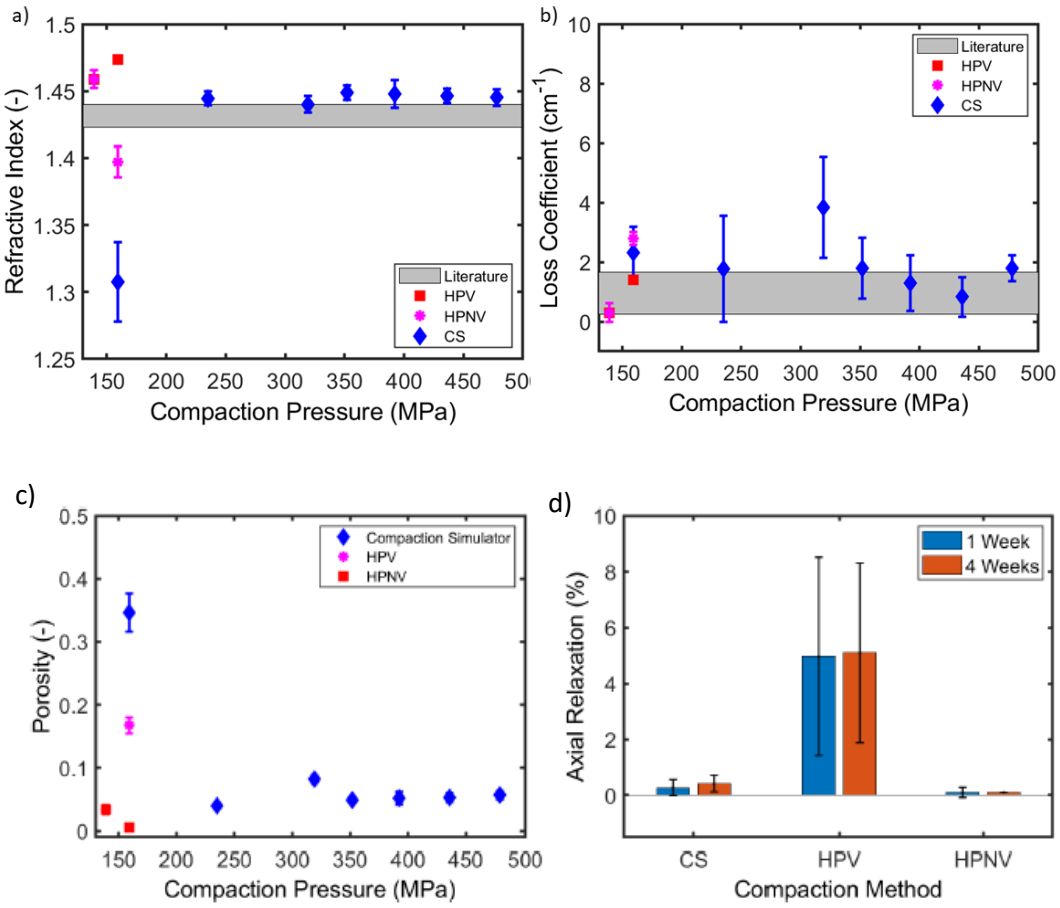

Figure 3-2: Refractive index (a) loss coefficient (b) Sample porosity (c) and axial relaxation (d) of PTFE pellets compacted at various pressures. Optical parameters were extracted at 2.45-2.55 THz. Three compaction methods were used: hydraulic press with a vacuum (HPV) and without a vacuum (HPNV) as well as a compaction simulator (CS). Literature values for both RI and loss coefficient are shown as a grey band. The literature is presented as a band reflecting the range of values for solid material quoted in the literature (Busch et al., 2014; D'Angelo et al., 2014; Sommer et al., 2016b; Wietzke et al., 2011; Yamamoto et al., 2004). Values plotted are the mean with the error bars depicting ± one standard deviation (n = 10).

3.4.3 Polyethylene

The full frequency spectra for both RI and loss coefficient for HDPE can be seen in Figure 3-3. It is evident that the HDPE pellets contain significant porosity as the RI is significantly lower than that for the solid reference material. The HDPE2 pellets have much higher loss values due to increased scattering in materials comprising a larger particle size. The increase in scattering phenomena as a function of frequency can be attributed to the dimensions of

particles or surface irregularities approaching parity with the wavelength of light at higher frequencies. As HDPE2 is more strongly absorbing, the Fabry-Perot oscillations are suppressed at higher frequencies because internal echoes are absorbed as they propagate through the material. The loss coefficient for the HDPE1 pellets is in good agreement with that of the solid reference material below 2 THz; however, higher frequencies are more affected by the scattering from particles, leading to significant excess loss above 1 THz. For subsequent analysis, mean values over a range (2.45-2.55 THz) were used due to the lack of spectral features and relatively high SNR.

Refractive indices extracted at 2.45-2.55 THz for HDPE1 (a) and HDPE2 (b) are presented in Figure 3-4 as a function of compaction pressure. The results indicate that the RI for both HDPE grades is significantly lower than the literature values. The lower RI suggests significant porosity in all samples, meaning that the polymer is unsuitable for accurate determination of RI. Samples made with the hydraulic press show slightly higher refractive indices than the compaction simulator; this increase is independent of the application of a vacuum. There is no distinguishable difference in RI between samples of the two grades.

Loss coefficients for HDPE1 (c) and HDPE2 (d) are presented in Figure 3-4 as a function of compaction pressure. The loss coefficient for the HDPE1 grade is in good agreement with the reference loss coefficient values, indicating low scattering. However, pellets made from HDPE2 exhibit significantly higher loss, which is attributed to increased scattering from the larger particle size. The loss coefficient remains constant because porosity is constant over the compaction pressure range (Figure 3-5). The variation is significantly higher for pellets produced at compaction pressures >350 MPa,

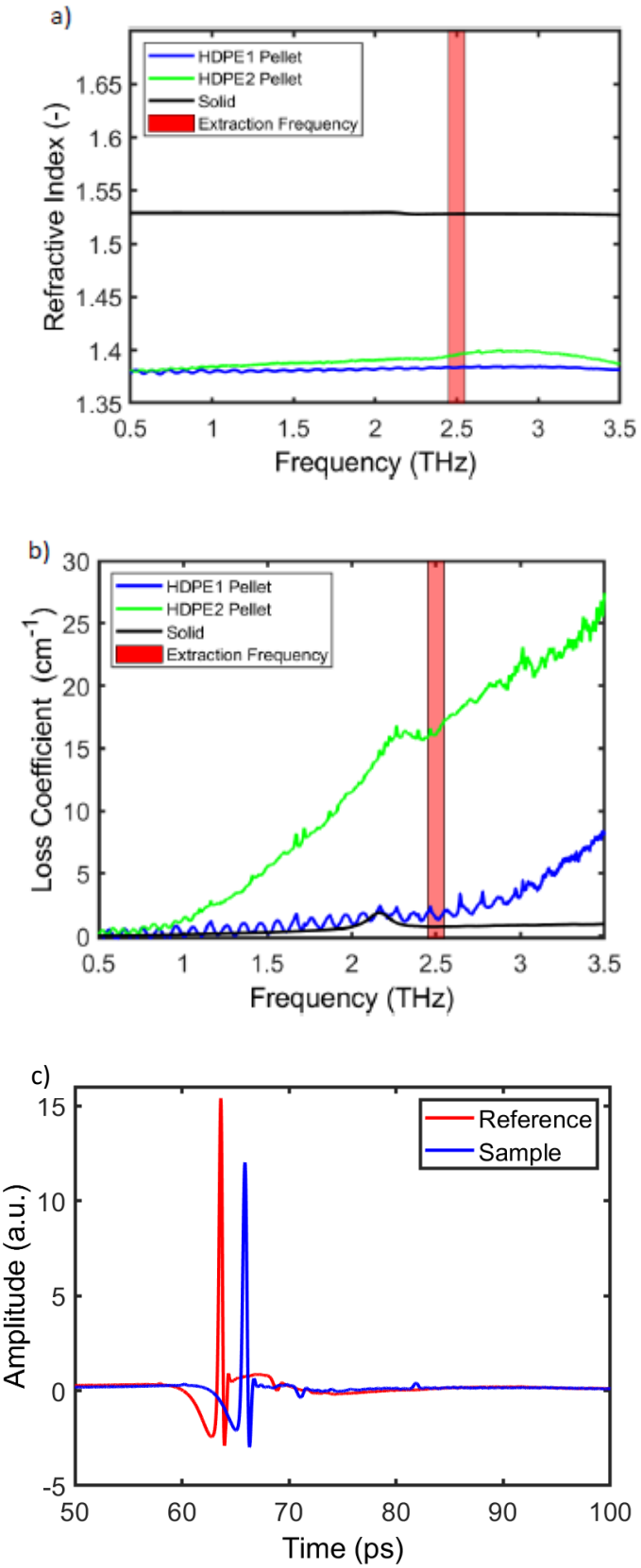

Figure 3-3: Spectra of HDPE pellets showing the (a) RI and (b) loss coefficient. Oscillations in spectra are artifacts due to internal reflections.

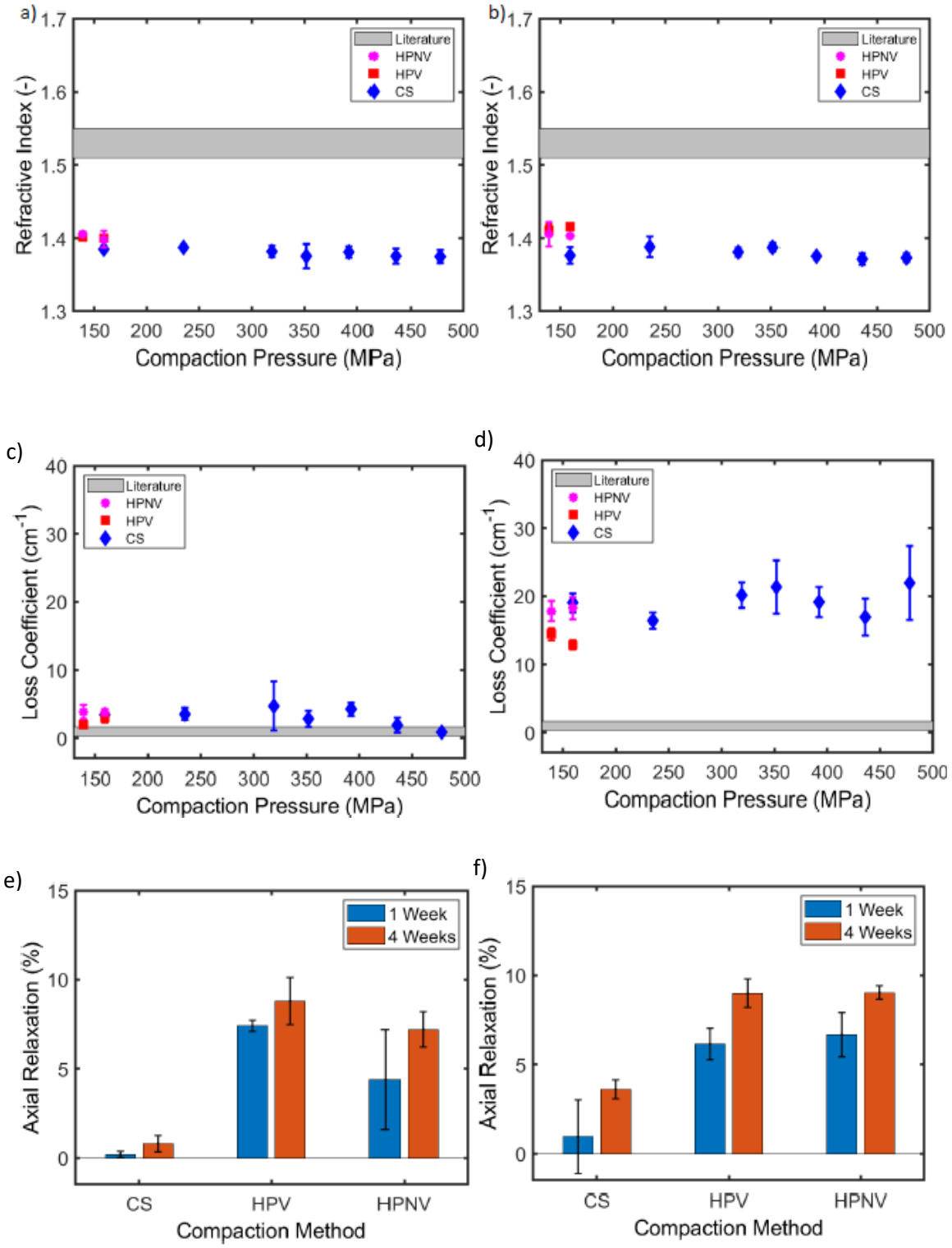

Figure 3-4: RI and loss coefficient extracted at 2.45-2.55 THz for (a, c) HDPE1 and (b, d) HDPE2 pellets compacted at various pressures. Additionally Axial relaxation for (e) HDPE1 and (f) HDPE2 pellets compacted at 159 MPa are shown. Three compaction methods were used: hydraulic press with a vacuum (HPV) and without a vacuum (HPNV) as well as a compaction simulator (CS). Reference values for solid RI are shown as a grey band. Values plotted are the mean with the error bars depicting ± one standard deviation ($n = 10$).

potentially due to microstructural defects because of high compaction pressure. These factors suggest that compaction pressures >350 MPa are unsuitable for sample preparation of this material.

The sample porosity for the HDPE pellets produced using the compaction simulator and the hydraulic press across all compaction pressures is shown in Figure 3-5. The ZPA was employed to calculate sample porosity from the RI. As can be seen from Figure 3-5, there is no significant difference in porosity between HDPE1 and HDPE2 batches. These porosity values are too large to extract accurate THz optical parameters. The inclusion of pores reduces the calculated effective RI and the pores scattering leads to an increased loss coefficient value.

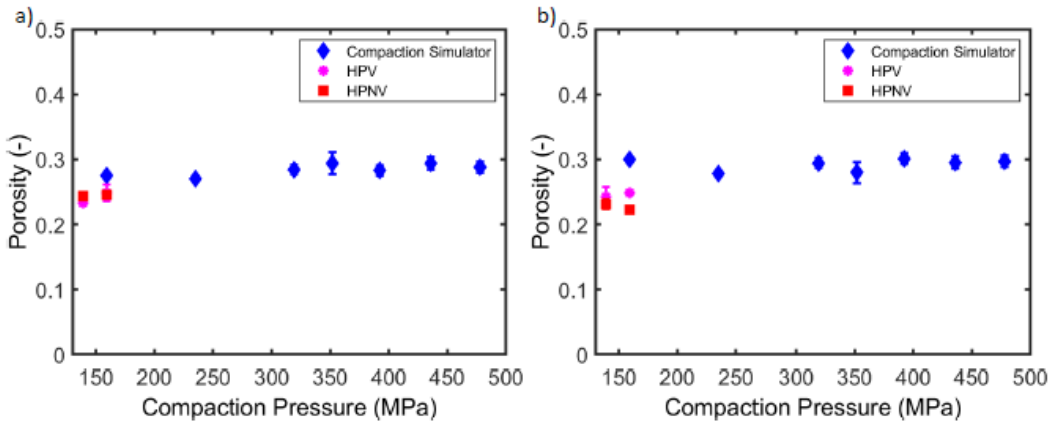

Figure 3-5 Sample porosity for (a) HDPE1 and (b) HDPE2 pellets compacted at 159 MPa. Three compaction methods were used: hydraulic press with a vacuum (HPV) and without a vacuum (HPNV) as well as a compaction simulator (CS). Values plotted are the mean with the error bars depicting ± one standard deviation ($n = 10$).

The HDPE pellets undergo significantly more axial relaxation one week after compaction (Figure 3-4 (e) and (f)) compared with that of PTFE pellets. Axial relaxation in HDPE samples continues to 4 weeks after compaction, with samples made using the hydraulic press (longer dwell times) showing more significant relaxation. Applying a vacuum leads to significantly

more elastic relaxation in HDPE1 (lower particle size) compared with HDPE2 (higher particle size). It is evident that particle size has a significant effect on the axial relaxation. Larger particle sizes will relax to a greater extent and show more significant differences between one and four weeks after compaction. Therefore, due to the axial relaxation of HDPE being significant for pellets produced using all compaction methods, it is clear that THz-TDS analysis should be conducted four weeks after compaction, allowing for repeated analysis.

In summary, the samples produced by all compaction methods show significant porosity, making them unsuitable for the accurate extraction of RI or loss coefficient values.

3.4.4 Tensile Strength

The tensile strengths of pellets of all grades compacted at 392 MPa were determined, showing a distinct difference in the strength of the pellets. PTFE and HDPE1 pellets exhibit significantly higher tensile strength than HDPE2 pellets (Table 3-3). This difference cannot be attributed to porosity since the porosity values of the two grades are similar within error. This change in tensile strength can be attributed to the different particle sizes. For HDPE, small particle sizes would be preferable for sample preparation, both in terms of tensile strength and reduced scattering. As both PTFE and HDPE1 have tensile strengths higher than 2 MPa, they would both be suitable for experimental handling, provided that they are compacted at >392 MPa. However, it must be noted that the handling of HDPE1 was inferior to that of PTFE. It was observed that, during the handling of HDPE1 pellets, the surface visibly crumbled and left residue on gloves, meaning repeated analysis of samples would lead to lower reproducibility.

Table 3-3 Tensile strength from hardness testing for all polymer materials. Pharmaceutical minimum standard for tensile strength of final product is 2 MPa.

Name	Tensile Strength (MPa)
PTFE	3.162 ± 0.050
HDPE1	2.142 ± 0.055
HDPE2	0.846 ± 0.058

3.5 Discussion

The results demonstrate that PTFE is preferred over HDPE for use as a matrix material due to the lower porosity of PTFE pellets. The PTFE samples have a high tensile strength, indicating that they are structurally robust when compacted at >392 MPa, allowing for repeated analysis and ease of handling.

The optimal compaction pressure for fabricating PTFE samples with the compaction simulator appears to be greater than 350 MPa to avoid lamination or capping. However, a lower compaction pressures should be used with a hydraulic press if the operator-controlled pressure release is well regulated to prevent the sample from being broken. The dwell time utilised by the compaction methods must also be considered, as a lower compaction pressure with a sufficiently long dwell time will achieve the same performance as a higher pressure with shorter a dwell time.

The particle size of the materials has a significant effect on tensile strength, axial relaxation, sample porosity and scattering. Smaller particle sizes would be preferable for scattering reduction and higher tensile strength.

Comparing the performance of the compaction simulator and the hydraulic press suggests that the hydraulic press is superior in creating lower porosity samples. This is primarily driven by the effect of dwell time, as the compaction simulator was set to a shorter dwell time compared with the hydraulic press, where the operator directly controls the dwell time. No noticeable advantage was observed by applying a vacuum to the die regarding the final porosity values. This is attributed to the axial relaxation after compaction, as a higher compaction pressure causes more significant axial relaxation (Bawuah et al., 2018; Markl et al., 2018) and greater changes in porosity. Analysis immediately after compaction is not recommended as changes in porosity will lead to a reduced reproducibility. However, using a vacuumed die for PTFE samples would be the preferred choice for minimising the effect of porosity if THz-TDS analysis must be carried out immediately after compaction and repeated analysis is not required.

Finally, there is a significant difference between the optical parameters extracted from the two HDPE grades. It is therefore advisable to create reference samples of pure matrix polymer for each batch of material.

3.6 Conclusions

The fabrication of polymer pellets for the accurate measurement of THz parameters was investigated. PTFE and HDPE pellets were created using various compaction pressures; measurements for THz-TDS, tensile strength, axial relaxation, and porosity were performed. Three compaction methods were used to assess their performance: hydraulic press with and without a vacuum, as well as a compaction simulator. Additionally, two different grades of HDPE to assess uniformity between grades and the effect of particle size was investigated.

PTFE was the preferred material for use as a matrix due to its low porosity and high tensile strength. It was found that a compaction pressure >350 MPa was required to prevent lamination/capping in compaction simulator samples. HPDE grades produce samples with significant porosity at all compaction pressures, making RI and loss coefficient extraction less accurate. There were noticeable differences in the extracted optical parameters between grades of HDPE, suggesting that inter-batch material variations reinforce the need for reference samples to be created for each batch of polymer. The particle size in HDPE primarily affected the resulting tensile strength and scattering loss of the material, with smaller particles producing pellets with higher tensile strength and lower loss coefficients. Pellets can increase in thickness after compaction for up to four weeks, meaning that THz-TDS analysis should be conducted after this period to ensure reproducible results.

Compaction using the hydraulic press resulted in noticeably superior samples, with a vacuum providing no noticeable benefits, apart from reduced porosity in PTFE pellets immediately after compaction. This performance improvement is primarily due to an increase in dwell time compared with that used for the compaction simulator (Wünsch et al., 2020). The ability to control the aspects of compaction in the simulator and recording of the in-die parameters such as thickness and diameter provide distinct advantage.

4 The Effect of Particle Size and Concentration on Low-Frequency Terahertz Scattering in Granular Compacts

4.1 Chapter Summary

This chapter investigates the fundamental relationships between particle size, concentration, and scattering contributions to the loss coefficient. Specially fabricated samples developed in the previous chapter are used to isolate and investigate required properties, laying the foundation for a particle size model and its application to pharmaceutical compacts. This chapter is based on a publication:

K. N. Murphy, M. Naftaly, A. Nordon, and D. Markl, “Effect of particle size and concentration on low-frequency terahertz scattering in granular compacts [Invited].” Optical Materials Express, vol. 13,no. 8, p. 2251, 2023, doi 10.1364/ome.494825

Keir N Murphy (Doctoral Candidate) contribution to the peer-reviewed paper:

a. Responsible for the entire experimental work and data analysis that includes the design of the experimental procedure, creation and subsequent analysis of all samples and presented data.
b. Wrote the entire manuscript and implemented any corrections and comments provided by the co-authors.

4.2 Introduction

Granular compacts are employed in various industries (Naftaly et al., 2019; Naftaly, 2014; Zeitler, 2016; Zeitler, 2012a), including but not limited to the pharmaceutical, food and chemical industries. These industries utilize granular compacts in multiple forms, from drug delivery vectors to catalytic materials and breakfast cereals (Naftaly, 2014; Zeitler, 2012b). Analytical techniques have been applied to control the quality and precision of such products, primarily with the aid of spectroscopic techniques. With spectroscopic measurements, various chemical and physical material properties can be determined, such as chemical structure, material homogeneity, and the inclusion of impurities or air voids introduced by the manufacturing process (Markl et al., 2017, 2018; Markl, 2017; Stranzinger, et al., 2019). The accuracy and precision of spectroscopic measurements can be significantly reduced by measurement errors caused by light scattering, which may lead to inaccurate interpretations and conclusions. The scattering of light in granular compacts is complex (Born et al., 2014, 2015; Born, 2017); rather than address it, data analysis often assumes little or negligible scattering, even when it is present and affects the accuracy of measurements.

This study systematically investigated the effect of particle size and concentration on THz scattering in granular compacts. A set of compacts was devised and fabricated, making it possible to vary the size and concentration of particles in a well-controlled manner. Granular compacts were fabricated using glass microspheres suspended in a PTFE matrix and compacted to create compacts with negligible porosity. Transmission THz-TDS was used to measure frequency-dependent scattering. The study quantified the dependence of the scattering contribution on particle size and concentration. The work studied the power-law dependence of scattering on frequency, identified the dependence of the power-law

coefficients on particle size and concentration, and investigated the saturation of scattering at higher concentrations as discussed in Chapter 1.4.3.

4.3 Materials & Methods

4.3.1 Materials

Microspheres of borosilicate glass having five size distributions (Cospheric LLC, 2.2 g/cm^{-3}, 38 – 45, 90 – 106, 125 - 150, 150 – 180 and 180 – 212 µm) were used with PTFE powder (Sigma Aldrich, free flowing, mean particle size 1 µm, 2.2 g/cm^{-3}) as the matrix material. PTFE was chosen as the matrix material due to its ability to create samples of negligible porosity under sufficient compaction pressure, ensuring precise control of the scattering properties of the sample set. The glass spheres were chosen due to their well-controlled particle size distributions, spherical shape, and sufficiently different RI from the PTFE matrix material.

4.3.2 Methods

4.3.2.1 Sample Preparation

Compacts were fabricated from borosilicate glass microspheres suspended in a PTFE powder matrix using a compaction simulator (HB50, Huxley-Bertram Engineering, Cambridge, UK; London, UK). For each size distribution of the glass microspheres, compacts were produced containing microspheres at six different concentrations in PTFE (2.5, 5, 10, 15, 20 & 30% w/w), and were allowed one week to undergo elastic relaxation to ensure reproducible analysis. Blends were created using an addition-based blending method to ensure a uniform distribution of microspheres confirmed by microscopy (Figure B-1 (Appendix)). The volume fraction, I, was subsequently calculated (2, 4, 9, 12, 17, 26 % v/v), using the mass (m_{glass} & m_{PTFE}) and true density (p_{glass} & p_{PTFE}) of components (Equation 29).

$$C = \frac{{}^{m_{\text{glass}}}/_{p_{\text{glass}}}}{{}^{m_{\text{glass}}}/_{p_{\text{glass}}} + {}^{m_{\text{PTFE}}}/_{p_{\text{PTFE}}}} \quad (29)$$

Batches of ten plane parallel compacts with a diameter of 9 mm and a thickness of 1 mm were fabricated for each particle size and concentration using 392 MPa of pressure (Murphy et al., 2022b). An additional batch of compacts was fabricated using pure PTFE to obtain the reference optical parameters (Murphy et al., 2022b).

4.3.2.2 THz-TDS Measurements

The method for THz-TDS measurements for each compact is outlined in Section 3.3.2.3.

4.3.2.3 Extraction of THz Scattering

By combining the absorption of solid borosilicate glass obtained from windows ($\alpha_{\text{abs,glass}}$) and PTFE ($\alpha_{\text{abs,PTFE}}$), it is possible to estimate the absorption contributions for the compacts at a given concentration (C %v/v) of microspheres by applying a linear mixing model.

$$\alpha_{\text{abs}} = C\ \alpha_{\text{abs,glass}} + (1 - C)\ \alpha_{\text{abs,PTFE}} \quad (30)$$

Subtracting the estimated absorption contributions from the measured loss coefficient of each compact yields the scattering contribution of the microspheres:

$$\alpha_{\text{scatt}} = \alpha_{\text{loss}}(\upsilon) - \alpha_{\text{abs}} \quad (31)$$

4.3.2.4 Estimation of THz Scattering at High Concentrations

The optical properties of media with high concentrations of borosilicate microspheres were measured using index-matching fluid. As it was not possible to prepare compacts with a concentration >30 %v/v of microspheres, a different method was used for these

measurements, using a liquid matrix instead. First, a cuvette was filled with microspheres, their transmission was measured, and the effective RI and loss coefficient were calculated. Then, the cuvette was filled with paraffin oil ($n_{\mathrm{paraffin}} \sim 1.5$), which has a similar RI to PTFE ($n_{\mathrm{PTFE}} \sim 1.45$), allowing for comparison between sample preparation methods. Using the linear mixing formula, the difference between the two values of the effective RI provides the volume fraction, f_{open}, of spheres in the cuvette.

$$f_{\mathrm{open}} = \frac{\Delta n_{\mathrm{eff}}}{(n_{\mathrm{paraffin}} - 1)} \tag{32}$$

where Δn_{eff} is the RI difference between the spheres in air and paraffin. With the volume fraction of the spheres, the estimated absorption can be calculated, allowing for the estimation of scattering at higher concentrations as outlined in the previous section.

4.4 Results & Discussion

An example of the frequency-dependent RI and loss coefficient of compacts consisting of borosilicate glass microspheres suspended in a PTFE matrix can be seen in Figure 4-1. The frequency range of valid data was 1.2 THz, the maximum obtainable for these samples given the system's DR (Jepsen, 2005). It should be noted that the PTFE data shown in Figure 4-1 does not exhibit the same oscillations as in Figure 3-1. This is due to the data shown being an average of ten pellets, thus smoothing the effect of the observed fabry-perot oscillations.

The scattering loss as a function of microsphere concentration for all sphere sizes is plotted at 0.6, 0.8 and 1 THz in Figure 4-2. These frequencies were chosen to show variation across the frequency range.

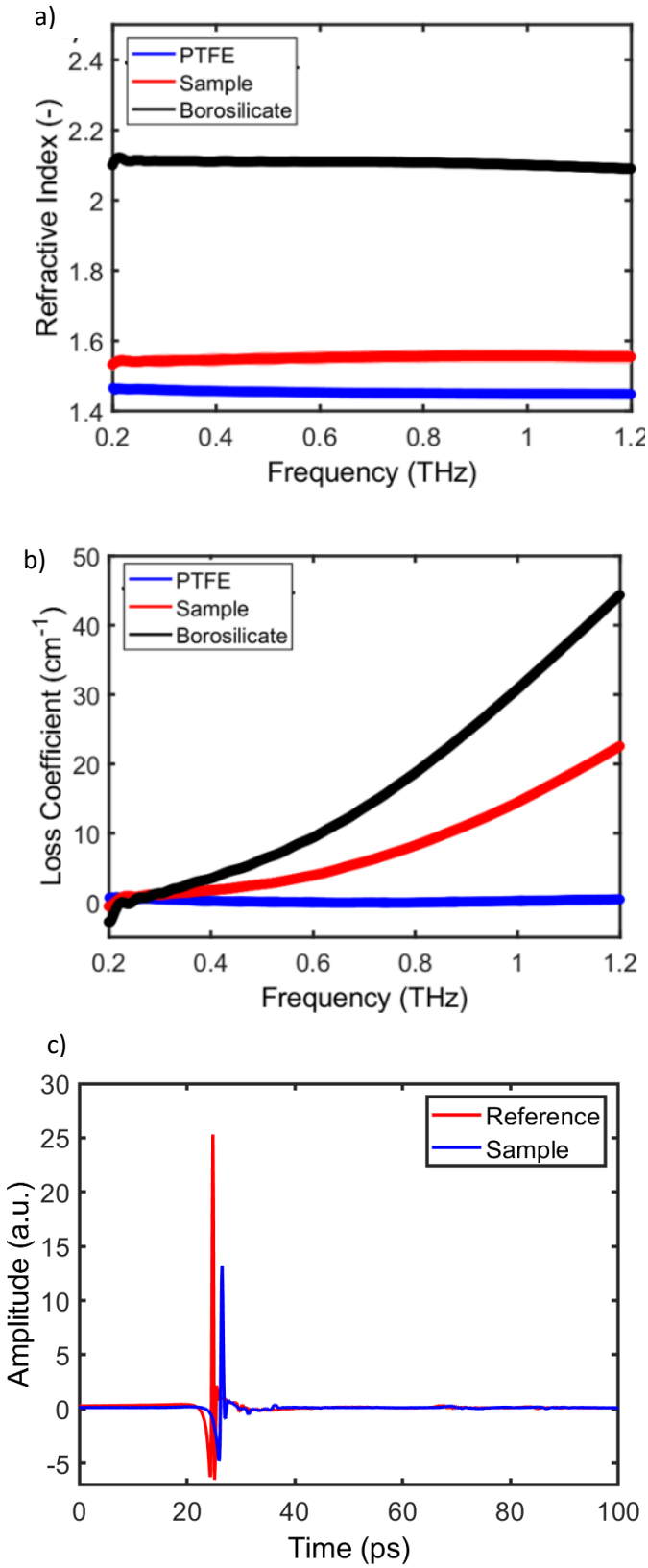

Figure 4-1: a) RI, b) loss coefficient and c) time domain spectra of compacts consisting of borosilicate glass microspheres (90-106 µm, 15 %v/v) in a PTFE matrix, pure PTFE samples and borosilicate windows. The values plotted are the mean and standard deviation (number of samples: $N_{\mathrm{sam}} = 10$, $N_{\mathrm{PTFE}} = 10$; $N_{\mathrm{boro}} = 5$).

The scattering contribution to the measured loss coefficient was evaluated using Equation 31 and knowledge of the microsphere concentration and the absorption by glass and PTFE. The calculated scattering values are plotted in Figure 4-2 as a function of concentration for all sphere sizes at three frequencies. It is evident that at low concentrations, scattering increases linearly; however, at higher concentrations, scattering becomes saturated. This is attributed to each additional microsphere acting as an individual scattering centre at low concentrations, giving rise to a linear dependence of scattering with concentration. At higher concentrations, however, photons will undergo multiple scattering from many microspheres so that individual microspheres contribute less to the total scattering loss, thus giving rise to saturation. Further, it is informative to consider photon propagation through the compact, which may occur ballistically (no scattering) or via scattering interactions. At low concentrations, photons propagate ballistically through the matrix, at high concentrations close to fully dense packing, the photons again propagate ballistically through adjacent glass microspheres. In the intermediate regime, photons are predominately scattered.

As discussed above, scattering is expected to increase linearly at low concentrations until the onset of scattering saturation. When the concentration approaches fully dense packing (maximum packing of spheres in a given volume (74 %v/v)), scattering is expected to decrease linearly. To experimentally observe the fall of the scattering after the onset of saturation, the method described in Section 4.3.2.4 was used to measure scattering for each particle size. This facilitated the evaluation of scattering for concentration levels > 30 %v/v. The normalized curves show that the onset of saturation is independent of both particle size and frequency (Figure 4-3). In contrast, the drop in scattering at high concentrations is size-dependent.

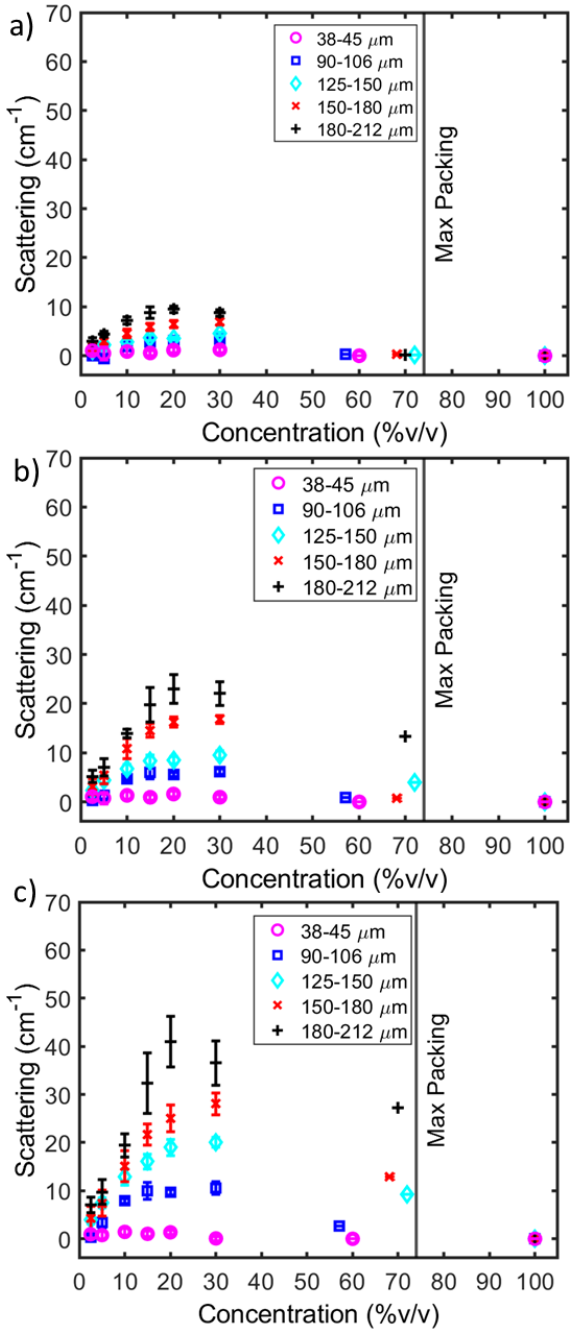

Figure 4-2: Scattering contributions for each particle size at a) 0.6 THz, b) 0.8 THz and c) 1 THz. Values plotted are the mean with error bars representing the standard deviation (N = 10, <30% v/v). Additionally maximum packing of spheres (face-centered cubic lattice, 74%v/v) was plotted as a vertical line.

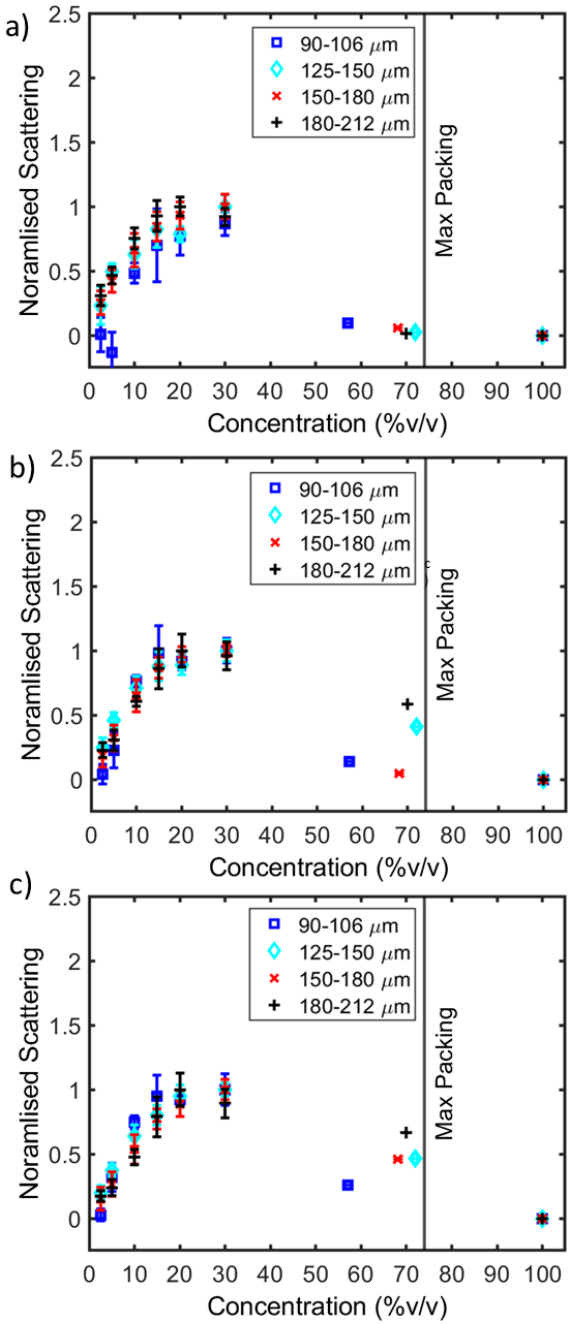

Figure 4-3: Scattering contributions normalised to the highest value per particle size for a) 0.6 THz, b) 0.8 THz and c) 1 THz. Values plotted are the mean with error bars representing the standard deviation (N = 10, <30 % v/v). For clarity, the lowest particle size distribution was removed as the normalised process introduced significant error bars due to the limit of detection. The figure with the lowest particle size is given in Figure B-2 of the appendix. Additionally maximum packing of spheres (face-centered cubic lattice, 74 %v/v) was plotted as a vertical line.

The power law fit followed the methods proposed by Shen et al. (Shen, 2008) with two fitting coefficients (A & B, Equation 15) However, unlike Shen et al. (Shen, 2008), the power law was applied to the scattering component only and not to the total of scattering and absorption (Figure 4-4).

Investigating the coefficients obtained from the power law fitting reveals their dependence on particle size and concentration (Figure 4-5). The power law fit was applied to all concentration levels to determine its applicability even after the saturation of scattering. The pre-exponential factor B increases both with concentration and particle size (Figure 4-5), reflecting the increase in scattering strength. Exponent A, in contrast, increases with particle concentration but is independent of the size of the spheres. This agrees with the findings in Figure 4-3 and shows that the form of scattering behaviour is independent of particle size. Once again, a linear increase at low concentrations before the onset of saturation occurs is observed.

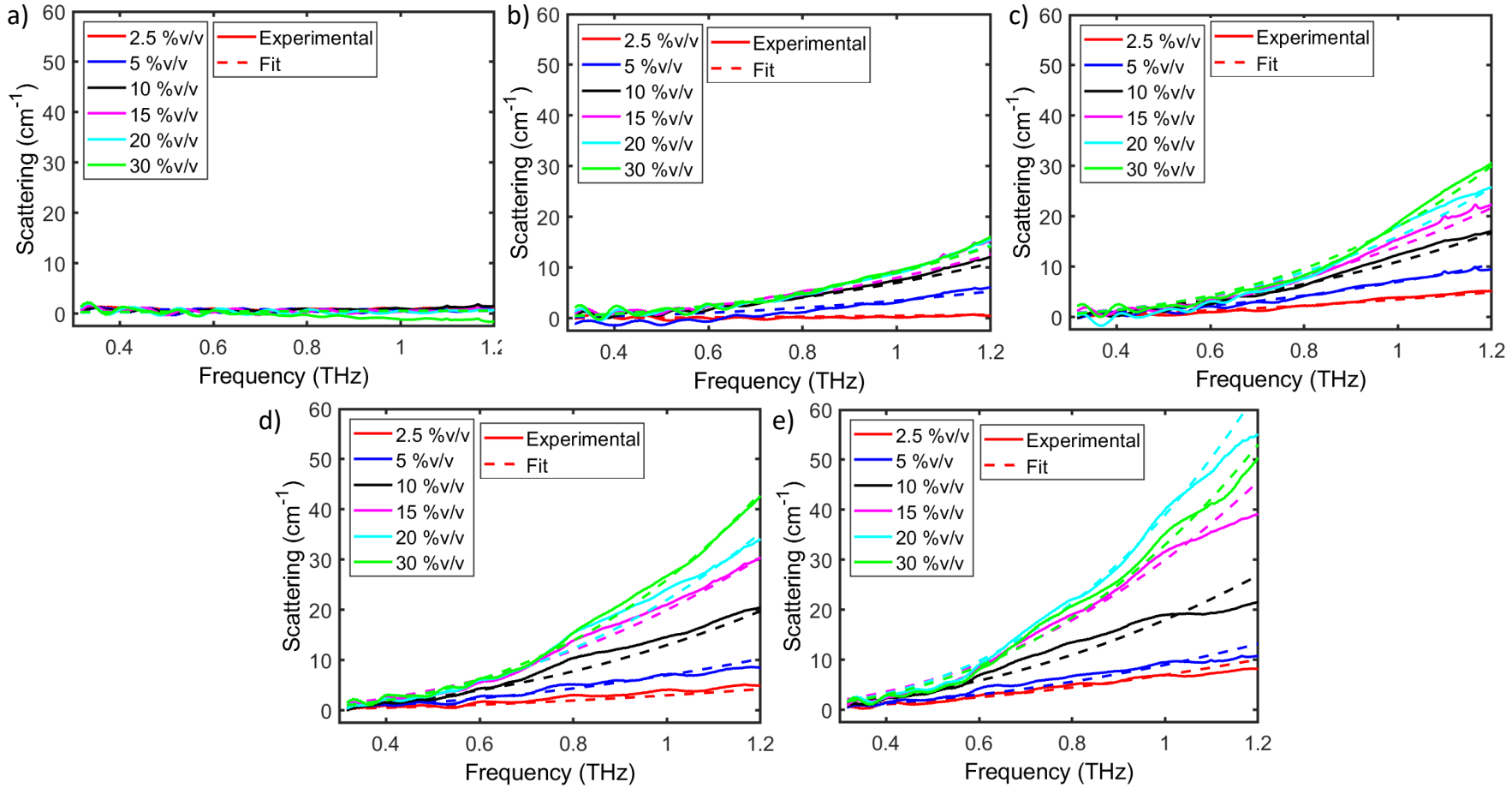

Figure 4-4: Power law fitted to scattering spectra a) 38 – 45 µm, b) 90 – 106 µm, c) 125 – 150 µm, d) 150 – 180 µm and e) 180 – 212 µm.

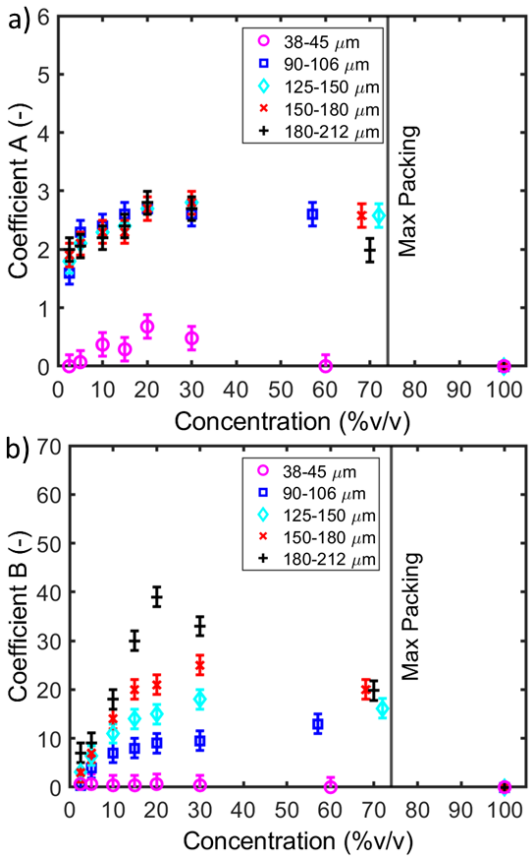

Figure 4-5: Coefficients a) A & b) B from applying the power law (Eq. 2) to the estimated scattering contributions. Values plotted are the mean and estimated confidence intervals. Additionally maximum packing of spheres (face-centered cubic lattice, 74 %v/v) was plotted as a vertical line.

The effect of scattering on the behaviour of the effective RI was also investigated. The frequency-averaged RI for all concentration levels of borosilicate microspheres can be seen in Figure 4-6. According to the linear mixing model, the RI is expected to be linearly dependent on the concentration of microspheres:

$$n_{\text{eff}} = C\, n_{\text{glass}} + (1 - C)\, n_{\text{PTFE}} \tag{33}$$

varying between the RI of PTFE ($n_{\mathrm{PTFE}} = 1.45$) and solid borosilicate glass ($n_{\mathrm{glass}} = 2.45$). At low concentrations, the refractive index indeed increases linearly. However, at higher concentrations > 15 %v/v, it becomes nonlinear. At high concentrations, > 50 %v/v, close to the maximum packing density, the refractive index exceeds the linear model.

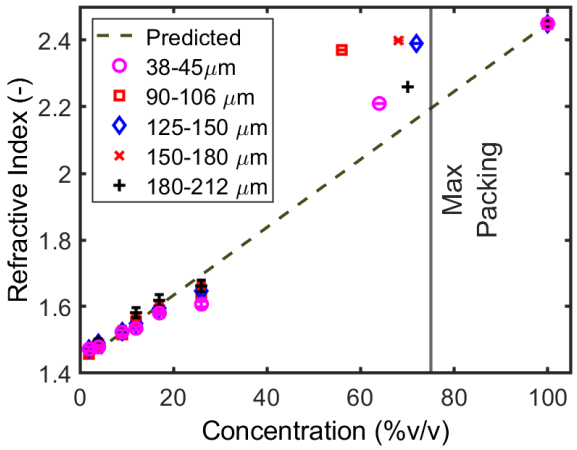

Figure 4-6: Frequency averaged RI (1 THz) for all particle sizes and concentrations. The values plotted are the mean and standard deviation (n=10, < 30%v/v). Additionally maximum packing of spheres (face-centered cubic lattice, 74%v/v) was plotted as a vertical line.

This behaviour may be explained by considering the path length of scattered photons. At low concentrations, photons are less likely to undergo multiple scattering, where photons travelling through the sample have their paths prolonged, leading to more complex trajectories. At the highest concentrations, photons experience multiple scattering, leading to slower propagation through the sample and, thus, a higher RI.

4.5 Conclusion

In this study, a systematic investigation was conducted of THz scattering in granular compacts with varying particle sizes and concentrations. Granular compacts were fabricated, formed of spherical particles in a solid medium with negligible porosity. Particle size and concentration

were controlled and varied with high accuracy and reproducibility. THz-TDS was used to investigate the effect of varying particle size and concentration on scattering. Using the measured optical properties of borosilicate glass, scattering contributions to the loss coefficient were isolated, allowing the effect of particle size and concentration on scattering to be quantified.

It was found that scattering increased linearly at lower concentrations. Scattering saturated at higher concentrations, reaching a maximum level dependent on the particle size. However, normalised scattering curves showed that the onset of saturation is independent of the particle size.

By applying the power law function to the scattering component, the dependence of the power law coefficients on particle size and concentration was revealed. It was found that the pre-exponential factor increased as a function of both concentration and particle size. The dependence on concentration was linear at low concentrations until the onset of saturation. The exponent was similarly dependent on concentration but independent of particle size.

The effective RI becomes sublinear with increasing particle concentration. At concentrations close to maximum density, it exceeds the linear model. This finding indicates that calculations based on the measured effective RI, such as porosity, are liable to have errors in samples with large scattering objects and high concentrations.

These findings may be explained by considering ballistic versus scattered photon propagation through the compact. At lower particle concentrations, most photons travel ballistically (without scattering). As the particle concentration increases, scattering increases linearly until the onset of saturation due to multiple scattering. As the concentration of microspheres

increases further and approaches fully dense packing, scattering falls again as photons increasingly travel ballistically through the glass. Future investigations into the effect of scattering will include particles of varied shapes as well as with bimodal particle size distributions.

5 Quantification of Agglomeration in Pharmaceutical Compacts by Terahertz Spectroscopy

5.1 Chapter Summary

This chapter applies the knowledge from the previous chapter to estimate particle size changes in complex pharmaceutical compacts using a simple empirical model with a calibration technique.

Declaration of contributions from collaborators:

a. Pharmaceutical samples were provided by Johnson & Johnson and Ghent University for analysis.
b. Acquisition of near-infrared chemical imaging (NIR-CI) and analysis was conducted by Dr Alexander Rychaert. Only the analysis required to understand the results was included.

5.2 Introduction

Tabletting in the manufacturing process is preferred due to being favourable for both the patients and the pharmaceutical industry due to their accurate dose, long shelf life, and ease of transportation (Gohel, 2005; Swarbrick, 2019). During tablet manufacturing, the API needs to be homogeneously dispersed in the formulation blend to ensure that each tablet contains the desired amount of API. This is especially challenging while processing micronised API where a decreasing particle size causes an increase in particle-specific surface area, leading to stronger cohesive and adhesive forces. Therefore, the increase in interparticle surface forces, such as electrostatic and Van der Waals forces, can make powders more prone to agglomeration, raising the risk of content uniformity failure. This risk is particularly prevalent for poorly soluble APIs, where micronisation is applied to improve dissolution performance and in turn, their bioavailability (Hartley et al., 1985; Hoffmann et al., 2015).

It is, therefore, evident that an analytical tool for the in-situ detection of agglomeration is crucial. While particle size estimation or the estimation of a change in particle size has been attempted with THz-TDS, it is still an underdeveloped application (F. M. Wu et al., 2015). From the previous application of a power law to model scattering in terahertz spectra, the pre-exponent has been shown to be dependent on both particle size and concentration. If the concentration is consistent the B fitting coefficient will change with particle size only. Using a technique such as NIR-CI, the fitting coefficient can be calibrated, allowing for an estimation of the particle size change in the compact. It is worth noting that the technique does not distinguish which constituent material has changed in particle size, only that there has been one. This is due to THz-TDS transmission being volume-based and, therefore, being representative of the bulk and not that of constituent materials.

In this study, THz-TDS was applied to evaluate and quantify the presence of API agglomeration in a complex pharmaceutical formulation. Tablets were fabricated at various compaction pressures ranging from 52 to 416 MPa at multiple API particle size distributions. Tablets that showed API agglomeration were further assessed utilising THz-TDS evoking the previously developed power law allowing for the estimation of agglomerate size in pharmaceutical compacts.

5.3 Materials and Methods

5.3.1 Materials, Formulation & Manufacture

The formulation under study consisted of 13.3% (w/w) API (J&J proprietary compound), a large content of α-lactose monohydrate (SuperTab® 11SD, DFE Pharma, Goch, Germany), microcrystalline cellulose (MCC, Avicel® PH102, FMC biopolymer, Philadelphia, USA), crospovidone (Polyplasdone XL-10, Ashland, Covington, KY, USA) and magnesium stearate (Liga magnesium stearate MF-2V, Peter Greven, Bad Münstereifel, Germany). Exact concentrations for each component are unavailable as the formulation is proprietary. The tablets were manufactured on a continuous, direct compression line and were compressed to fabricate shallow concave tablets with a diameter of 7 mm and thickness ranging from 3.5-4.5 mm. The compression force was varied at seven levels: 52, 104, 156, 208, 260, 312, and 416 MPa. Three different API batches were used for the manufacturing of the tablets; each batch varied in API particle size distribution derived from laser diffraction (Table 5-1). Unfortunately, as the formulation is proprietary additional information regarding particle size distribution is unavailable.

Table 5-1: Percentile values of particle size distributions (d_{10}, d_{50} & d_{90}) for batches A-C.

Batch Name	d_{10} (µm)	d_{50} (µm)	d_{90} (µm)
Batch A	14	30	55
Batch B	24	40	66
Batch C	21	50	95

Methods

5.3.1.1 THz-TDS Measurements

The method for THz-TDS measurements for each compact is outlined in Section 3.3.2.2.

5.3.1.2 Nominal porosity

The tablet density (ρ) of each tablet was calculated from its weight and dimensions as:

$$\rho = \frac{m}{V} = \frac{m}{2V_c + \pi\left(\frac{d}{2}\right)^2 (L - 2H_c)} \quad (34)$$

where m is the mass, V_c is cup volume of the punch tip, d is tablet diameter, L is tablet. thickness, H_c is cup height of the punch tip and V is volume.

5.3.1.3 Terahertz Time Domain Spectroscopy Porosity Analysis

Nominal sample porosity was modelled with extracted refractive index measurements to determine the intrinsic RI of the material (n_1), i.e. RI at a zero-porosity tablet (Bawuah, et al., 2020). This intrinsic refractive index is the refractive index of the blend at zero porosity. The zero-porosity approximation (ZPA) (Equation 35) was employed to relate sample porosity (ρ) and the effective RI (n_{eff}) of the sample extracted from the THz-TDS measurement of the tablet.

$$\rho = \frac{n_{\text{eff}} - n_1}{1 - n_1} \quad (35)$$

5.3.1.4 Assay

API content of five tablets per batch was determined using a gradient reversed-phase ultra high-performance liquid chromatography with UV detection (UHPLC–UV) method. Each individual tablet was mixed with a 900 mL solution containing 0.75% (w/v) sodium lauryl sulphate in 0.05 M sodium phosphate buffer pH 6.8 for 2 h. Subsequently, a 5 mL mixture was filtered through a 0.45 µm regenerated cellulose filter. The UHPLC equipment used for analysis was a Nexera X3 (Shimadzu, Kyoto, Japan) with a C-18 column (Acquity, 150 x 2.1mm, 1.7 µm) connected to a PDA detector (λ = 238 nm; SPD-M40, Shimadzu, Kyoto, Japan).

5.3.1.5 NIR Reflectance of Powders

NIR spectra of the pure powder compounds were collected in reflection mode using a diode array system SentroPAT FO (Sentronic, Dresden, Germany). This NIR spectrometer was coupled via a fibre-optic cable to a SentroProbe DLR RS NIR (Sentronic, Dresden, Germany). The acquisition of a single spectrum was performed with an integration time of 9 ms, and an average of fifty spectra was taken**.**

5.3.1.6 NIR-Chemical Imaging of Tablets

The API homogeneity for all API batches was evaluated using a NIR-CI device (VLNIR with OLES56 lens, Specim, Finland) equipped with a halogen lamp. An image of the top, bottom, and inside of each tablet was acquired. The inside of a tablet was measured at different heights by manually slicing layers from the top of the tablet. All spectral data processing occurred in MATLAB (MathWorks® version R2019a, Natick, Massachusetts, USA), using the

HYPER-Tools package (Mobaraki, 2018). Principal component analysis (PCA) was executed on the pre-processed spectra to analyse the chemical composition at each pixel on the image. Then, the pure spectra of the original components were evaluated for similarity to the loadings of the tablets' spectra. NIR-CI images that demonstrated agglomeration were further analysed in Python 3.10 to estimate the agglomerate size.

5.4 Results

5.4.1 THz-TDS Measurements

The full loss coefficient frequency spectrum for an exemplary compacted pharmaceutical tablet can be observed in Figure 5-1. It is evident that the spectrum of the formulation is lactose-dominated with no API-related spectral features (i.e. chemical information) observed. The frequency range was limited to 1.7 THz as this is the maximum valid frequency before the noise floor is reached. For the purposes of analysis, due to the absence of spectral features, loss coefficient plots are extracted at 1 THz (Figure 5-1).

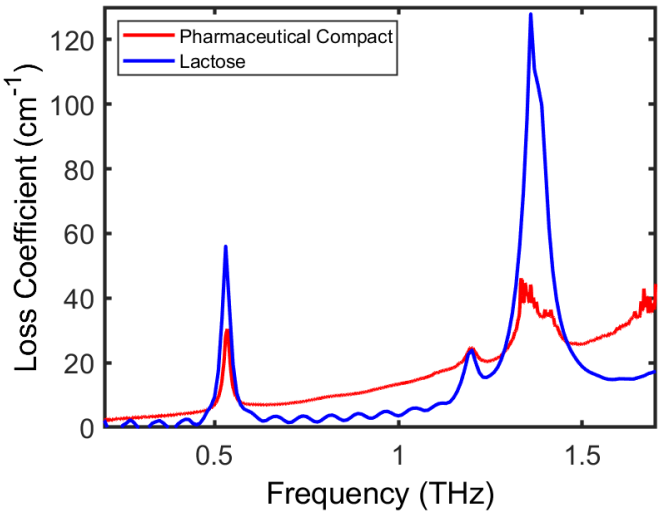

Figure 5-1: Loss coefficient spectra of pharmaceutical tablet (Batch A, 416 MPa, Tablet 1) and pure lactose.

5.4.2 Porosity Determination using THz-TDS Analysis

The effective RI in the THz region indicates alterations in porosity. Generally, higher RI values were observed for higher compaction pressures due to denser tablets (Figure 5-2). Batches A and B have a larger standard deviation, especially at higher compaction pressures, compared to batch C (highest $d_{50} = 50$ µm). The relationship between RI and porosity can be approximated by a linear function across this porosity range (Bawuah, Markl, Turner, et al., 2020; Markl et al., 2017, 2018; Markl & Zeitler, 2017).

With the application of the ZPA, the intrinsic refractive indices for the different batches can be determined. From Table 5-2 it is evident that the intrinsic refractive index increases with manufacturer d_{50} values. This increase is primarily driven by a decrease in standard deviation of the data set. The RI of the compacts rises with increasing compaction pressure (Figure 5-3).

Table 5-2: Intrinsic RI values for batches A-C. Values shown are the calculated intrinsic refractive index form ZPA.

Batch Name	Intrinsic RI
Batch A ($d_{50} = 30$ µm)	1.736
Batch B ($d_{50} = 40$ µm)	1.753
Batch C ($d_{50} = 50$ µm)	1.782

The increase in RI is attributed to reduced sample porosity with increasing compaction pressure (Figure 5-2). It is also observed that the RI increase with compaction pressure follows the commonly observed exponential relationship between compaction pressure and porosity, e.g. described by the Gurnham equation (Reynolds et al., 2017). Finally, it is observed in Figure 5-3

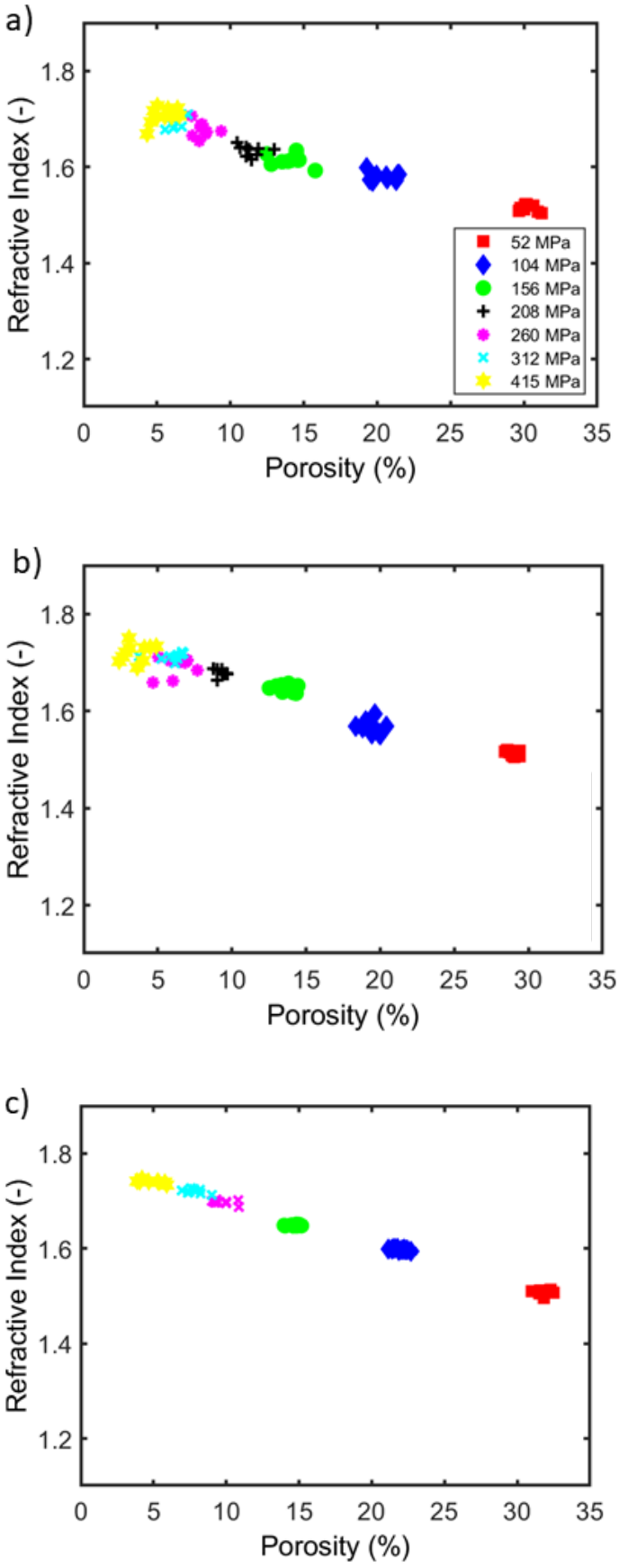

Figure 5-2: Effective RI (1 THz) and nominal porosity of the batches A ($d_{50} = 30$ µm) (a), B ($d_{50} = 40$ µm) (b) and C ($d_{50} = 50$ µm).

that RI is independent of particle size (Chapter 4). Surprisingly, the scattering contributions of particles become less significant with increasing particle size, resulting in an overall decrease in the loss coefficient (Figure 5-3). This contradicts the theory that a rise in particle size leads to more pronounced scattering. Since there is no noticeable change in the RI values (optical density) and the tablet assay (Figure C- (Appendix)) has confirmed uniform API content throughout the batch, this change in loss can only be attributed to a change in domain size or shape. Therefore, the higher loss coefficient values suggest some form of uncontrolled agglomeration taking place in batches A and B with the two lowest API particle sizes. The presence of agglomeration was subsequently evaluated by taking NIR-CI images of the tablets.

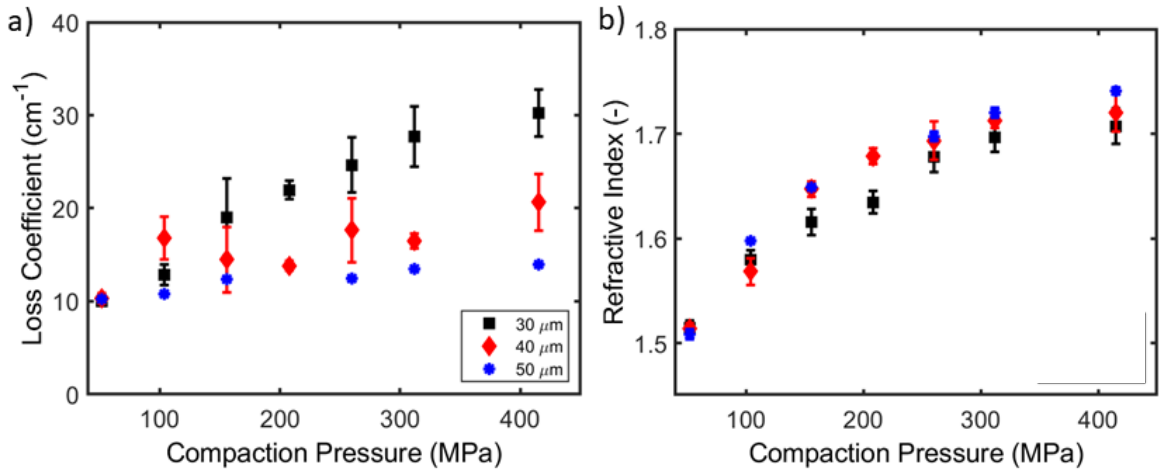

Figure 5-3: Loss coefficient extracted at 1 THz (a) and effective RI (b) for each of the particle size batches at various compaction pressures. Values plotted are the mean and standard deviation (n= 10).

5.4.3 Near-infrared Chemical Imaging

NIR-CI images were recorded for tablets compressed at the highest and lowest compression force for all API particle sizes. A representative NIR-CI image of the inside of a tablet for all three batches A, B & C ($d_{50,A} = 30$ µm, $d_{50,B} = 40$ µm & $d_{50,C} = 50$ µm) compressed at the lowest pressure is shown in Figure 5-4. For all tablets, a PCA was performed for each tablet and a score map and a corresponding loadings plot were generated.

For batch A, the score map of PC1 and PC2 shows two features where the colour deviates from the remaining tablet surface. This is most pronounced in the PC2 score map, where two green-yellow dots can be observed. These spots correspond to a higher absorbance of the API, confirming that the two features are related to API agglomerates. Although the effect was less pronounced for batch B, a smaller yellow dot in the score map of PC2 (Figure 5-4) with a similar loading plot (Figure 5-4) was also observed, demonstrating the presence of API agglomerates in these tablets.

On the contrary, differently coloured features were not observed for batch C. In the score maps of the different PCs, a more homogenous distribution of similar colours was observed. This indicates less spectral variability between the different pixels, and a homogenous blend composition is present. In addition, the loadings of the PCs of batch C do also not correspond to the API spectrum. Therefore, it can be concluded that API agglomeration only occurred for the tablets manufactured with the two smallest API particle sizes.

The presence of API agglomeration can further explain the observed larger error bars for the loss coefficient values for the two smallest API size batches (Figure 5-5). Since the beam waist of the THz-TDS is smaller than the diameter of the tablet (2 mm), it is possible that some agglomerates are not or only partially captured in the analysis, leading to a larger deviation in loss coefficient.

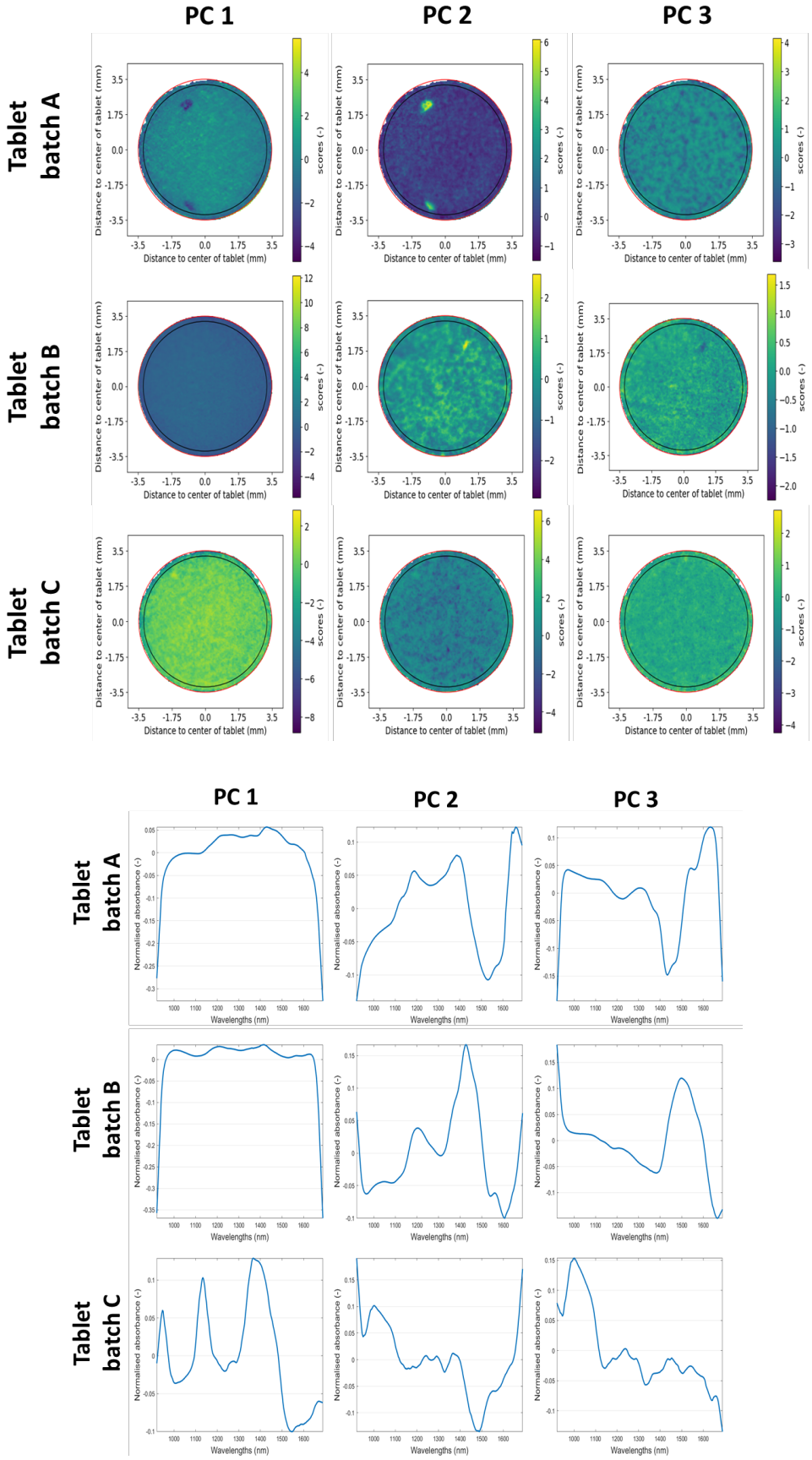

Figure 5-4: Score map (top) and corresponding loadings (bottom) plot for NIR-CI images recorded from the inside of a tablet manufactured at the lowest compression pressure (52 MPa) for the batches A, B and C. NIR analysis carried out by Dr Alexander Rychaert (Ghent University, Belgium).

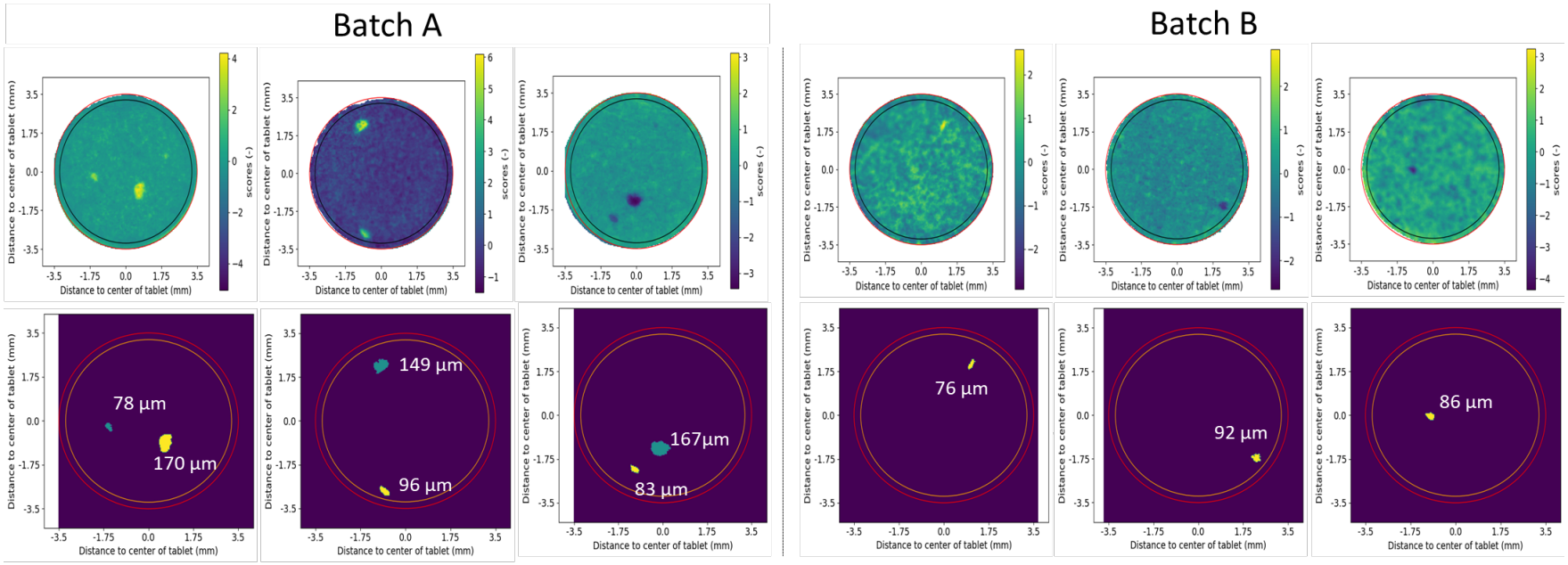

Figure 5-5: PC score map (top) and the corresponding image to show the demarcated agglomeration area (below) to estimate the agglomeration size for batch A ($d_{50} = 30$ µm) (left) and batch B ($d_{50} = 40$ µm). NIR analysis carried out by Dr Alexander Rychaert (Ghent University, Belgium).

As a next step, the NIR-CI images that showed API agglomeration were further analysed to estimate the agglomerate size. A few examples are displayed in Figure 5-5 for batches A, B & C from the inside of tablets compressed at 52 MPa. For the smallest API particle size (Batch A), the estimated agglomeration size for these three images varied from 78 to 182 µm with a mean of 132 µm. For the 40 µm batch, the agglomerate size varied between 76 and 92 µm with a mean of 85 µm based on three NIR-CI images. In general, the API agglomerate size increased for decreasing API particle size, which is in line with the finding of Hausner et al. (Hausner, 2022).

5.4.4 Particle Size Estimation by THz-TDS

Figure 5-6 illustrates the relationship between the power law fitting coefficient B (Equation 15) and the estimated agglomerate size by NIR-CI for all batches. Fitting was conducted as though no spectral features were present. It is worth noting that the linear fit intersects the origin, reflecting the absence of scattering particles when the coefficient is non-existent. It is evident that there is a strong linear relationship (R^2= 0.90482) between the Shen Coefficient

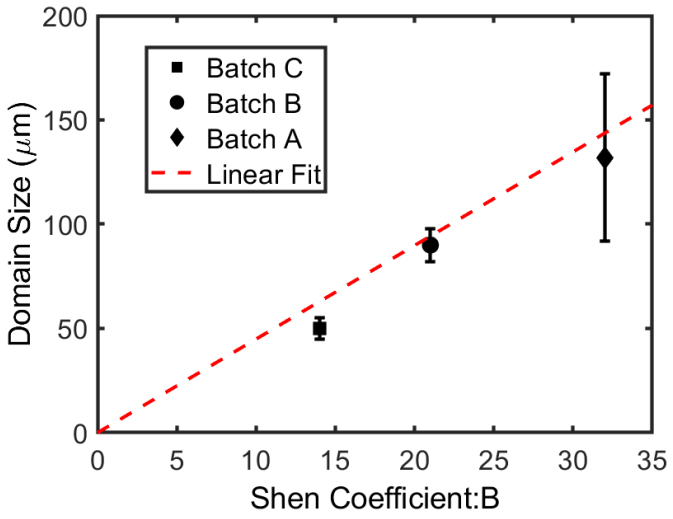

Figure 5-6: Shen coefficient calibration with NIR-CI results for all batches with the linear fit passing through the origin. Values plotted are the mean and standard deviation ($n = 5$). R^2= 0.90482, $y = 4.4899x$.

and particle size in compacts with the same concentration level. Using this linear relationship, the particle size can be estimated non-destructively using THz-TDS as can be seen in Table 5-3.

The estimated particle size by THz-TDS is in good agreement with the NIR-CI results. These results clearly demonstrate the ability of THz-TDS to non-destructively estimate changes in particle size or agglomerate size in pharmaceutical compacts. Estimation of particle size relies on a constant concentration of compacts and a calibration curve using NIR-CI or other particle size measurements.

Table 5-3: Estimated particle size for each formulation batch for both NIR-CI (n=5 (416 MPa)) and THz-TDS (n=10 (416 MPa)). * Batch C has no error due to laser diffraction measurement. NIR analysis carried out by Dr Alexander Rychaert (Ghent University, Belgium).

Batch Name	NIR-CI Mean Agglomerate Size (µm)	THz-TDS Mean Domain Size (µm)
Batch A ($d_{50} = 30$ µm)	132 ± 40	130 ± 8
Batch B ($d_{50} = 40$ µm)	90 ± 8	88 ± 8
Batch C ($d_{50} = 50$ µm)	50	55 ± 8

5.4.5 Conclusions

In this study, RI and loss coefficient of tablets manufactured at various compaction pressures ranging from 52 to 416 MPa using multiple API particle size distributions was determined using THz-TDS. API agglomeration was observed for tablet batches consisting of the two smallest API particle sizes and was subsequently quantified using NIR-CI. The power law fit was used to non-destructively estimate the API agglomerate size and was found to be in good agreement with the NIR-CI measurements. The power law model has shown that THz-TDS can be utilised to estimate particle size changes in pharmaceutical tablets non-destructively with a suitable calibration. Such a technique can be invaluable in formulation development and process control of pharmaceutical tablets. Future work would involve the application of the

power law model to other formulations to assess its applicability for widespread use. In addition, the effect of API agglomeration on tablet quality attributes such as disintegration and dissolution can be assessed.

6 Observation of spurious spectral features in mixed-powder compressed pellets measured by terahertz time-domain spectroscopy.

6.1 Chapter Summary

This chapter discusses an unexpected finding encountered at the end of the project. It was found that spurious features are encountered in the loss coefficient upon expanding the dynamic range of the analysis. The samples measured were identical to those fabricated for Chapter 4 (section 4.3.2.1). This phenomenon is further investigated with different materials confirming the presence of the features. This chapter is based on a publication:

K. N. Murphy, D. Markl, A. Nordon, and M. Naftaly, "Observation of spurious spectral features in mixed-powder compressed pellets measured by terahertz time-domain spectroscopy.," *IEEE Transactions on Terahertz Science and Technology*, vol. 13, no. 5, pp. 569-572, Sept. 2023, doi: 10.1109/TTHZ.2023.3290118.

Keir N Murphy (Doctoral Candidate) contribution to the peer-reviewed paper:

a. Responsible for all experimental work and data analysis, including designing the experimental procedure, creating and subsequent analysis of all samples and presented data.
b. Wrote the entire manuscript and implemented any corrections and comments provided by the co-authors.

6.2 Introduction

As discussed previously, highly absorbing materials are typically produced in the form of powders and must be compressed into pellets to enable quantitative spectroscopic measurements. They often have multiple strong polymorphic form-specific absorption features, such that pellets of practical thickness exceed the dynamic range of THz-TDS instruments at frequencies above 2 THz (Jepsen, 2005). Consequently, in order to study the vibrational spectra of these materials over extended frequency bands, they are often mixed with a THz-transparent dilutant powder such as PE or PTFE (Zeitler, 2016). Studying spectra of organic materials in mixed powder compressed pellets using THz TDS is a widely employed and well-established technique. In using this method, it is assumed that the measured THz spectra of target materials are not altered by the sample preparation process, which includes factors such as material concentrations, mixing, and compaction.

In this study, a possible issue that may arise when employing this approach is brought to light. Additionally, observations of spurious loss features in the samples fabricated in Chapter 4, section 4.3.2.1 as well as alpha-lactose monohydrate suspended in a PTFE powder matrix identical to that of the borosilicate microsphere compacts, are recorded. The intensity and frequency of these features are seen to be dependent on grain size and concentration.

6.3 Results

THz-TDS transmission measurements were conducted using a Teraflash Pro (Toptica) spectrometer, with the beam path purged with dry air. The THz beam path used four parabolic mirrors arranged in a Z-configuration. All mirrors were F/2, with 25 mm mirror diameter and 50 mm effective focal length. Sample diameter was 9 mm; samples were placed in the focal

plane between mirrors two & three. Figure 6-1 shows the source amplitude spectrum and its noise floor. The frequency-dependent loss coefficient ($\alpha_{\text{loss}}(\nu)$) and RI ($n(\nu)$) were extracted in an identical fashion that was employed in Chapter 4, section 4.3.2.2. In Chapter 4, measurements of THz scattering in compacts consisting of PTFE powder and borosilicate glass microspheres with a range of microsphere sizes and concentrations. Loss spectra and refractive indices of these compacts were measured at frequencies in the range 0.2 - 1.2 THz, and the scattering effects were analysed as a function of grain size and concentration (Chapter 5).

a)

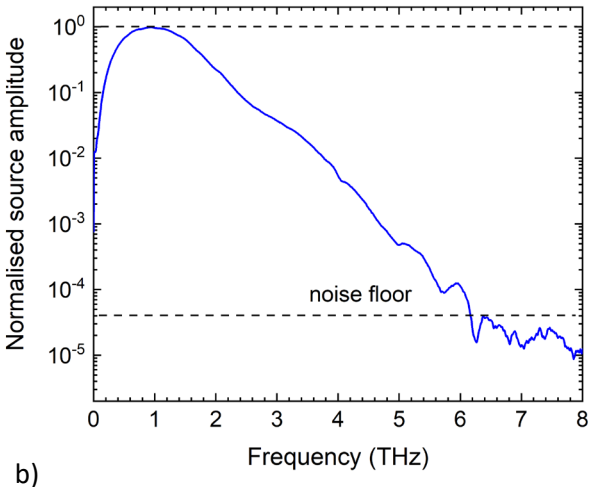

b)

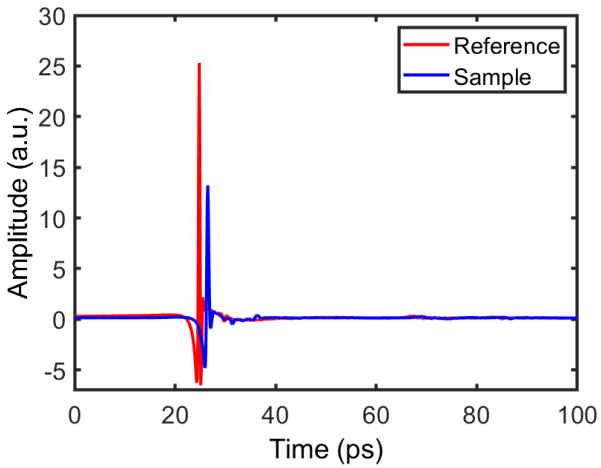

Figure 6-1: a) Normalised source amplitude and its noise floor b) time-domain spectra of borosilicate microspheres (90-106 µm, 15 %v/v) in a PTFE matrix.

Subsequently, the frequency range of the study was extended to 4.0 THz. Unexpected loss features were seen in the spectra of the samples; some examples are shown in Figure 6-2 (a) and (b). In the frequency range examined, the absorption spectra of both PTFE and borosilicate glass are monotonically rising functions. Therefore, the loss spectra are expected to appear as a featureless rising edge. The observed features must, therefore, be considered spurious, arising from beam propagation through the sample material rather than due to absorption. These features depended on the grain size and concentration, as seen in Figure 6-2 (a) and (b).

Figure 6-2 c) shows the refractive indices of these samples. As expected, the refractive indices of two samples containing 20% glass microspheres are similar, below 2 THz and are higher than that of the sample containing 10% glass microspheres. At the frequencies where sharp loss features occur, there is a corresponding pronounced rise in the RI. Note that phase unwrapping may be ambiguous where there is a steep change in the RI, as occurs at 2.3 THz for the sample containing 20% v/v beads of 90-106 μm (red line), where phase unwrapping is a mathematical process applied after FFT due to the introductions of phase discontinuities. Such cases may be clarified by examining multiple samples with comparable properties. This is particularly relevant for mixed-powder samples, such as these, because they often exhibit strong narrow loss peaks accompanied by steep dispersion of the RI.

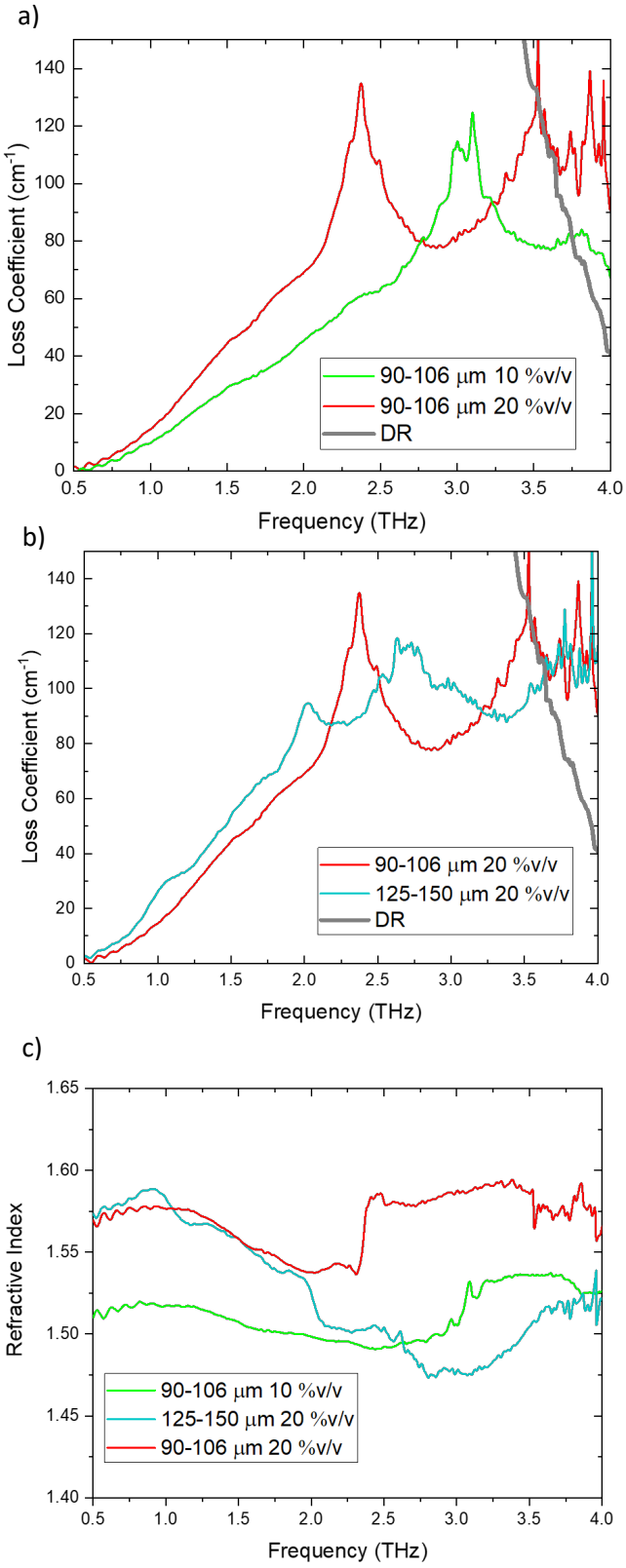

Figure 6-2: Loss coefficient measured by THz-TDS in compressed pellets of PTFE and glass microspheres. Spectra of samples with a) varying glass microspheres volume/volume (v/v) concentration (10 and 20 %v/v) and b) varying grain size ranges, i.e., 90-106 µm and 125 µm, are shown. The refractive index of the pellets is also shown (c). The dynamic range limit (DR) was calculated according to Jepsen et al (Jepsen, 2005).

An explanation of these spurious spectral features may be arrived at by considering the effects of variable optical thickness of the material experienced by different parts of the traversing THz beam due to the inhomogeneous nature of the mixed-powder compacts.

Variations in the optical thickness of the sample give rise to spurious loss features in the transmission spectrum because a time-domain trace containing multiple pulse peaks can be regarded as a convolution of a single pulse with a number of delta functions. In the frequency domain, this is translated to the product of the Fourier transform (FT) of a single pulse with the FT of a set of delta functions, as shown in Figure 6-3. The dependence of the observed spurious spectral features on the grain size and concentration may be explained by the geometrical effects of these parameters on the beam path length variability through the sample material.

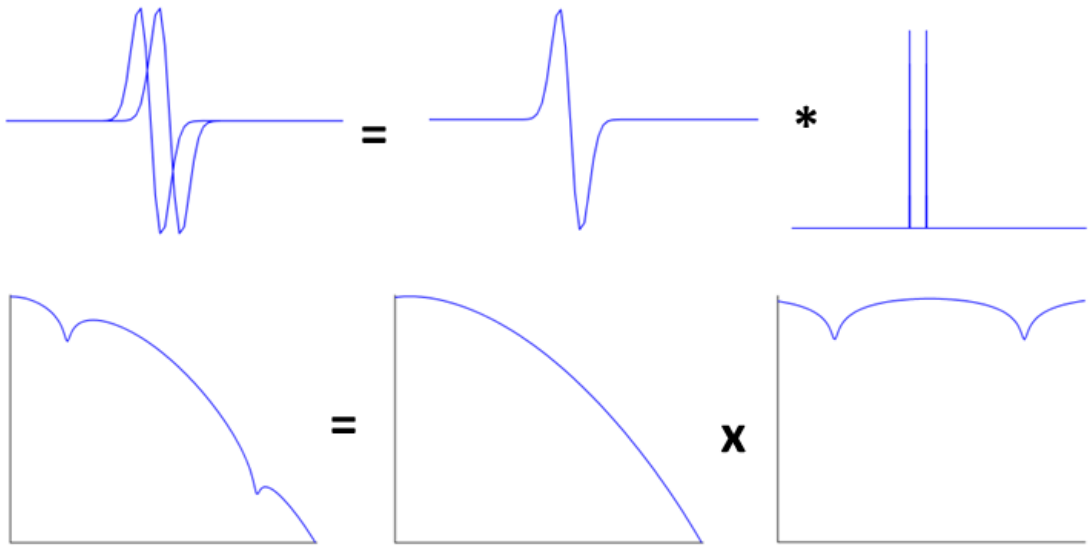

Figure 6-3: Model data explaining the appearance of spurious loss features due to path length difference in the sample material. The convolution of the two functions is denoted with the symbol *

To verify the presence of this effect in a material that is more relevant to spectroscopic studies, pellets consisting of PTFE were examined (Sigma Aldrich, free flowing, mean grain size 1 µm, 2.2 g cm^{-3}) and varying concentrations of α-lactose monohydrate (Sigma Aldrich, D_{50} = 50 µm

(Naftaly et al., 2020). Figure 6-4a) presents the loss coefficients as measured, and Figure 6-4b) shows them normalised to the peak at 1.4 THz for ease of comparison. In Figure 6-4b), the spectrum of the pure lactose pellet shows reduced scattering loss at frequencies above ~2 THz due to the higher homogeneity of this material. Two spurious features are observed in pellets containing 20% and 30% lactose; the profile of the feature at 3.3 THz differs between the two concentrations, whereas the feature at 2.9 THz remains constant. It may be supposed that the grain size determines the frequency of spurious features in lactose-PTFE pellets, as it appears to be in the glass-PTFE pellets in Figure 6-2, and that, therefore, their overlap with the absorption bands is coincidental. Figure 6-4c) shows and exhibits anomalous dispersion corresponding to the lactose absorption peaks. In addition, at frequencies corresponding to spurious loss features, the RI shows a pronounced dip.

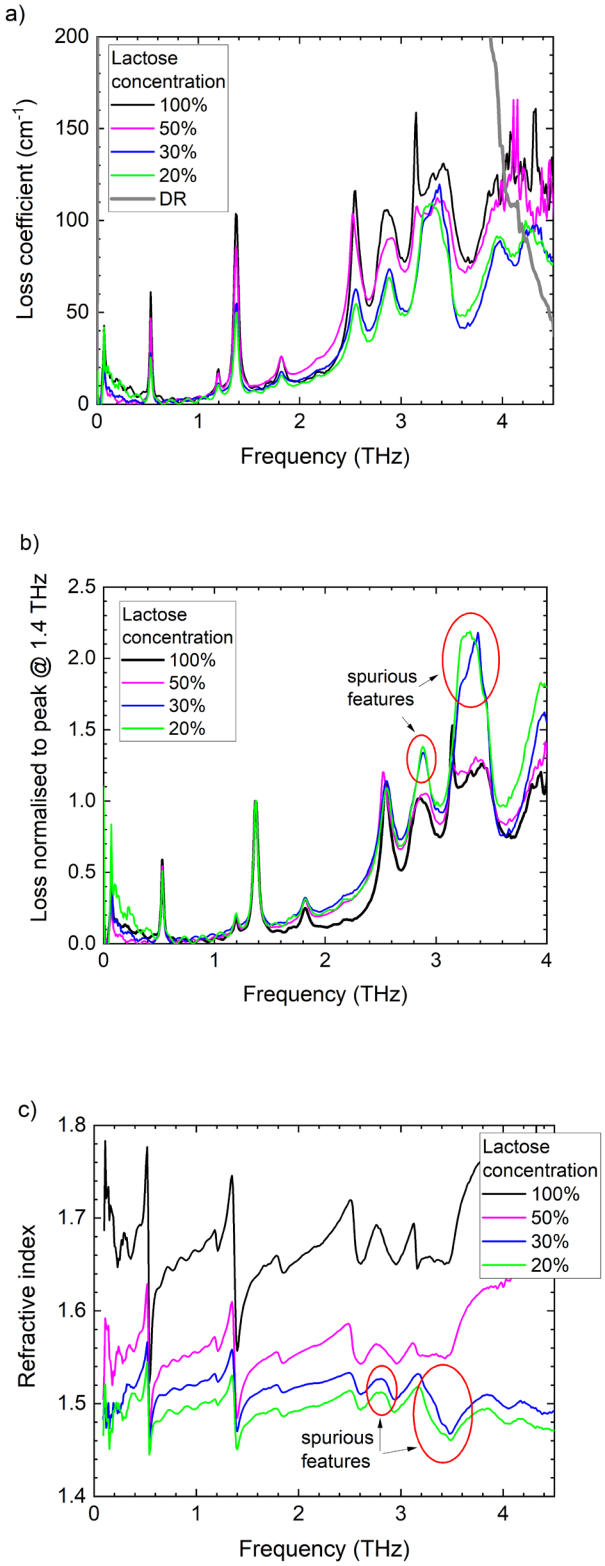

Figure 6-4: a) Loss coefficient measured in mixed PTFE and lactose pellets with different concentrations of lactose; DR limit was calculated from (Jepsen, 2005) is also shown. b) Loss spectra of pellets shown in (a) normalized to the peak at 1.4 THz for ease of comparison. Spurious features are highlighted. c) refractive indices of pellets shown in (a).

6.4 Conclusions

THz TDS in transmission is widely used for spectroscopic measurements on powders of biochemical and pharmaceutical materials. A common method for preparing such materials for measurements is to dilute them with THz-transparent powder and compress the mixture into pellets. In this study, spurious loss features in such pellets were observed.

Loss features that do not arise from absorption in the constituent materials were observed in two types of mixed-powder pellets: PTFE-glass microspheres and PTFE-lactose. The features were seen to be dependent on grain size and concentration. An explanation of the effect due to the variability of the optical path length through the inhomogeneous pellet material is proposed. When employing THz TDS for transmission studies of mixed-powder pellets, it is advisable to examine a range of samples with different concentrations of constituent powders and, if possible, with different grain sizes. Similar considerations may apply to FTIR measurements, which are also based on detecting the optical path length through the sample and employing a FT to obtain spectral information.

Work is currently underway to clarify the dependence of loss peak frequency and intensity on the grain size, concentration, and material. It is expected that the frequency and profile of the spurious features may be used to estimate the size and concentration of scatterers in granular materials.

7 Conclusions and Future Outlook

7.1 Conclusion

This thesis has studied the relationship of THz scattering from granular compacts, with the main application of utilising THz-TDS for the non-destructive estimation of particle size in such samples. Such an application would allow for in-situ measurements during the manufacturing process, increase the speed of formulation development, and ensure the quality of the final product.

Samples were required to isolate both particle size and concentration to determine the applicability and sensitivity of the technique for particle size measurement. To this end, various polymer compacts were created and analysed using THz-TDS to determine the optimal material and compaction pressure to minimise the effects of sample porosity while preventing microstructure defects introduced by high compaction pressure. Ten tablet batches for seven compaction pressures and three grades of polymers were fabricated using a compaction simulator. It was found that PE samples showed significant porosity at all compaction pressures, which limited their use as matrix material. PTFE, however, exhibited minimal sample porosity and sufficient hardness, allowing for handling over a longer period. Finally, axial relaxation of the polymer materials was analysed as multiple THz-TDS measurements over a longer period were scheduled, meaning that changes in sample porosity after the first measurement would lower the reproducibility of results. It was found that for PTFE, one week of relaxation post-compaction was necessary before analysis. This study is also useful for the broader terahertz science community as PE and PTFE are commonly used materials to prepare samples for THz studies.

Using the previously determined parameters, samples of borosilicate microspheres at six concentration levels and five particle sizes were fabricated. Subsequent light microscope images were taken to ensure homogenous distributions of microspheres throughout the bulk and confirm minimal porosity throughout the matrix material. After one week, to allow for axial relaxation, the samples were subsequently analysed using THz-TDS. The frequency domain RI and loss coefficient were extracted following the extraction procedure discussed in Chapter 1.

The scattering contributions to the loss coefficient for the samples were then estimated using optical-grade borosilicate windows. This extracted scattering was further investigated for its relationship to particle size and concentration. Scattering in the terahertz region depended solely on the concentration of microspheres (volume fraction) in the sample. Furthermore, it was also found that the scattering contributions increase linearly at low concentrations before the onset of saturation and subsequent fall at higher concentrations. It was hypothesised that this phenomenon was related to photons' ballistic vs non-ballistic travel through the sample. At lower particle concentrations, most photons travel ballistically (without scattering). As the particle concentration increases, scattering increases linearly until the onset of saturation due to multiple scattering. As the concentration of microspheres increases further and approaches fully dense packing, scattering falls again as photons increasingly travel ballistically through the glass.

Furthermore, the samples created provided an opportunity to investigate for the first time the dependence on the fitting coefficients of the Shen power used previously to correct for scattering in granular compacts. It was found that coefficient A solely depended on sample concentration, whereas the B coefficient was related to both the concentration and particle

size. The B coefficient provided a further opportunity as if the concentration of the mixed compact remained constant; the B coefficient could be employed to detect a particle size change or, with the aid of a calibration technique, allow for the non-destructive estimation of particle size in granular compacts.

The next step involved applying the newfound scattering knowledge to more complex materials. To this end, pharmaceutical compacts provided by Ghent University were analysed using THz-TDS. Upon initial inspection of the loss coefficient, it was found that the manufacturer-provided particle size distribution needed to be corrected, assuming that all other aspects of the compact were constant. Furthermore, from the loss coefficient and the variance within the batch, it was hypothesised that uncontrolled agglomeration was present in the compacts. Subsequent assay determined that the API content was uniform among all analysed compacts, suggesting that the change was solely due to particle size or shape. NIR-CI was then applied to the compacts, which showed significant agglomeration and was in agreement with the initial hypothesis from the THz-TDS analysis. Finally, a linear relationship was achieved by applying Shen's' power law to the loss coefficient and with the NIR-CI to calibrate the coefficient to particle size. This study demonstrated the applicability of THz-TDS to detect particle size changes in compacts with a consistent formulation and with the aid of a calibration technique such as NIR-CI or microscopy to provide particle size estimation in granular compacts.

Finally, measurements allowing for a higher dynamic range were conducted during the studentship placement at the National Physical Laboratory. The findings were exciting and concerning in equal measure. Spurious features were found at the higher frequencies, changing both as a function of particle size and concentration. It was hypothesised that this is

due to the variation in optical path length when analysing mixed samples. Upon FFT, spurious features can be observed, leading to concerns for measurement reproducibility.

7.2 Future Work

This work lays the foundation for expansion from an application and a fundamental science approach. Specifically, the following studies would be of great interest:

- **Investigation of power law to additional formulations to determine its applicability to industry.** While the application of Shen's power law as a proof of concept has been demonstrated in an earlier chapter, the variance between formulations may pose unique challenges to adoption in industry. Expanding the study to various formulations and materials from other industries is crucial to generating confidence in the technique and may increase the uptake from industry.

- **Expansion of particle size distributions of microsphere samples, including bimodal distributions.** Expanding the particle size distributions is crucial in identifying the sensitivity of the technique for particle size change detection. Furthermore, including bimodal distribution may prove interesting as, in some industrial cases, it may be useful to use such distributions (e.g., pharmaceutical samples).

- **Use different glasses for the microsphere compact to simulate the effect of RI difference on THz scattering.** One of the main obstacles in scattering analysis is the dependence of the scattering magnitude on the RI difference between media. Such a relationship has yet to be explored in as controlled manner as it is possible with the microsphere compacts developed during this project. Such a study could further lay the foundations for a more comprehensive scattering model.

- **Further investigation into the appearance of the spurious features described in a previous chapter.** Further investigation into this phenomenon's causes would include creating various samples from various industries with subsequent THz-TDS with extreme bandwidth, allowing for a large dynamic range. Such an investigation would increase awareness of the phenomenon and potentially lead to future developments to mitigate or remove the effect of the extraction process. While being a concerning discovery from a reproducibility standpoint, it potentially provides a new method for particle size estimation in mixed samples. As the spurious features are dependent on particle size and concentration, with the aid of the microsphere compacts designed, developed, and analysed in this project, it may be possible to estimate particle size from the location in the frequency spectrum with sophisticated modelling.

8 Appendix

8.1 Appendix A

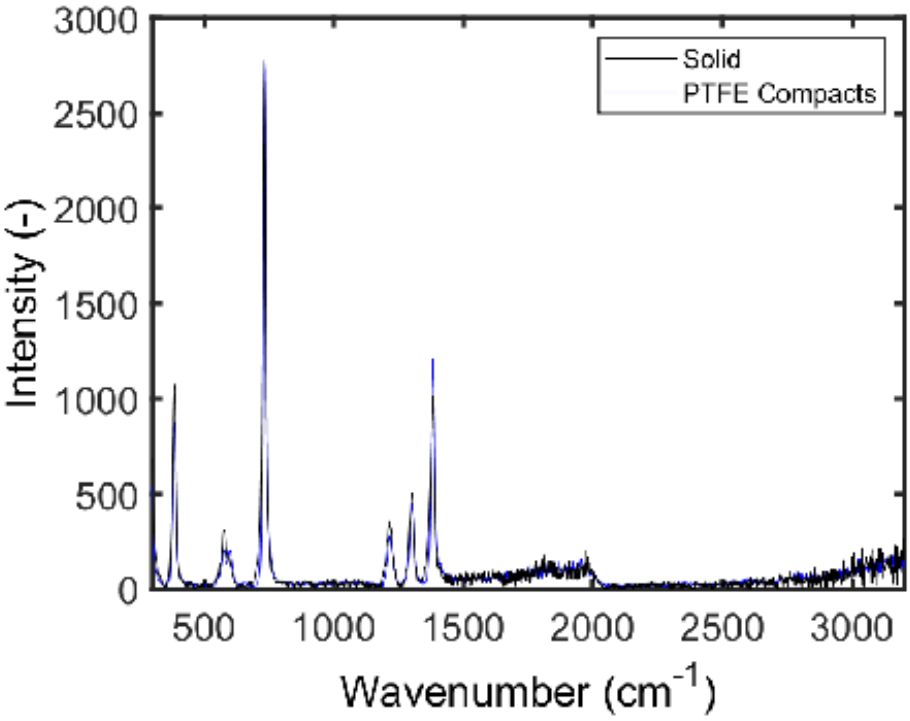

Figure A-1: Raman spectra (Bruker Bravo, Billerica, Massachusetts, United States) of PTFE pellets and solid PTFE showing no changes in crystalline or amorphous character.

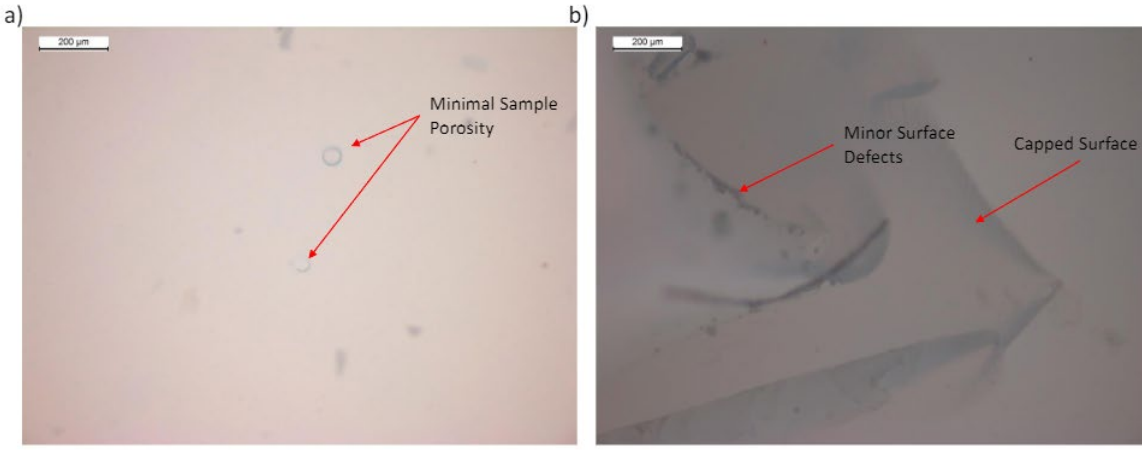

Figure A-2: Microscope images of PTFE pellets showing minimal samples porosity and capping evidence on the surface of the pellets compacted at lower pressures. a) PTFE pellet produced with a compaction pressure of 392 MPa with minimal sample porosity and b) PTFE pellet produced with a compaction pressure of 235 MPa with surface imperfections/capping.

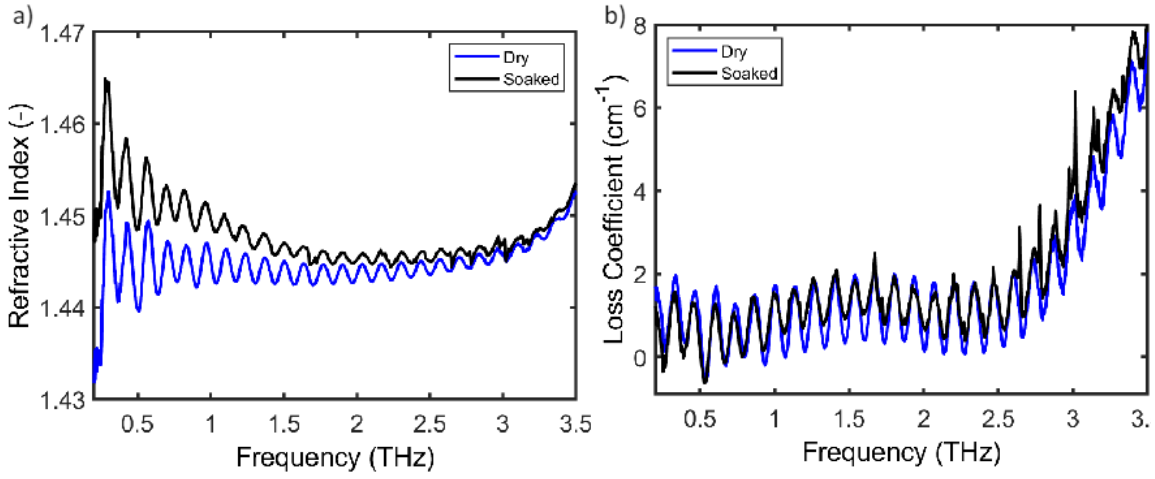

Figure A-3: THz-TDS optical parameters of the dry and paraffin-soaked pellets. a) RI and b) loss coefficient.

8.2 Appendix B

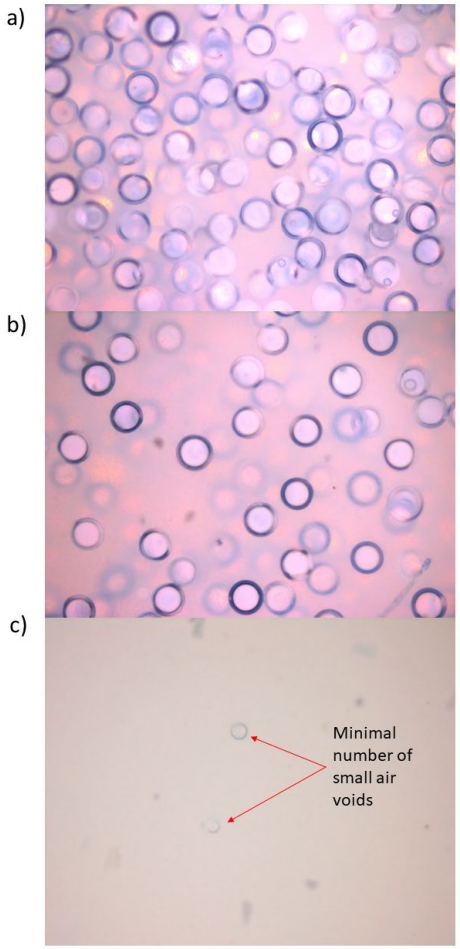

Figure B-1: Light microscope images of a) borosilicate microsphere suspended in a PTFE powder matrix showing homogenous distribution of microspheres (30 %v/v) b) borosilicate microsphere suspended in a PTFE powder matrix showing homogenous distribution of microspheres (10 %v/v) c) PTFE powder compact showing minimal number of small air voids in samples post axial relaxation.

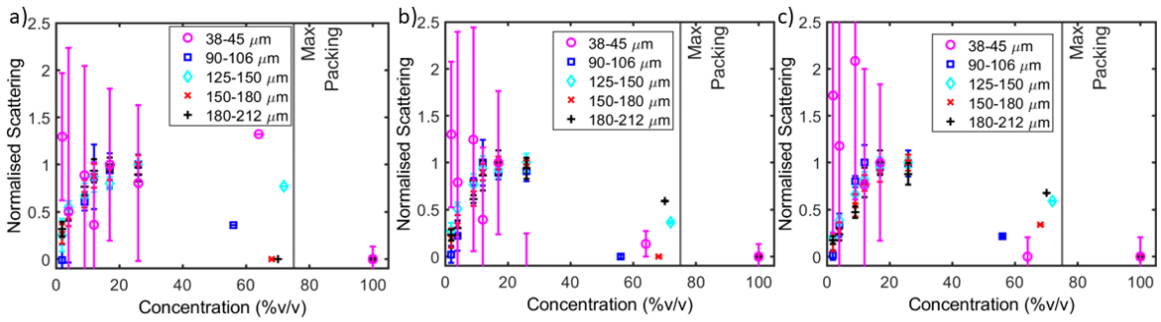

Figure B-2: Normalized scattering contributions for a) 0.6 THz, b) 0.8 THz and c) 1 THz. Values plotted are the mean with error bars representing the standard deviation (n = 10).

8.3 Appendix C

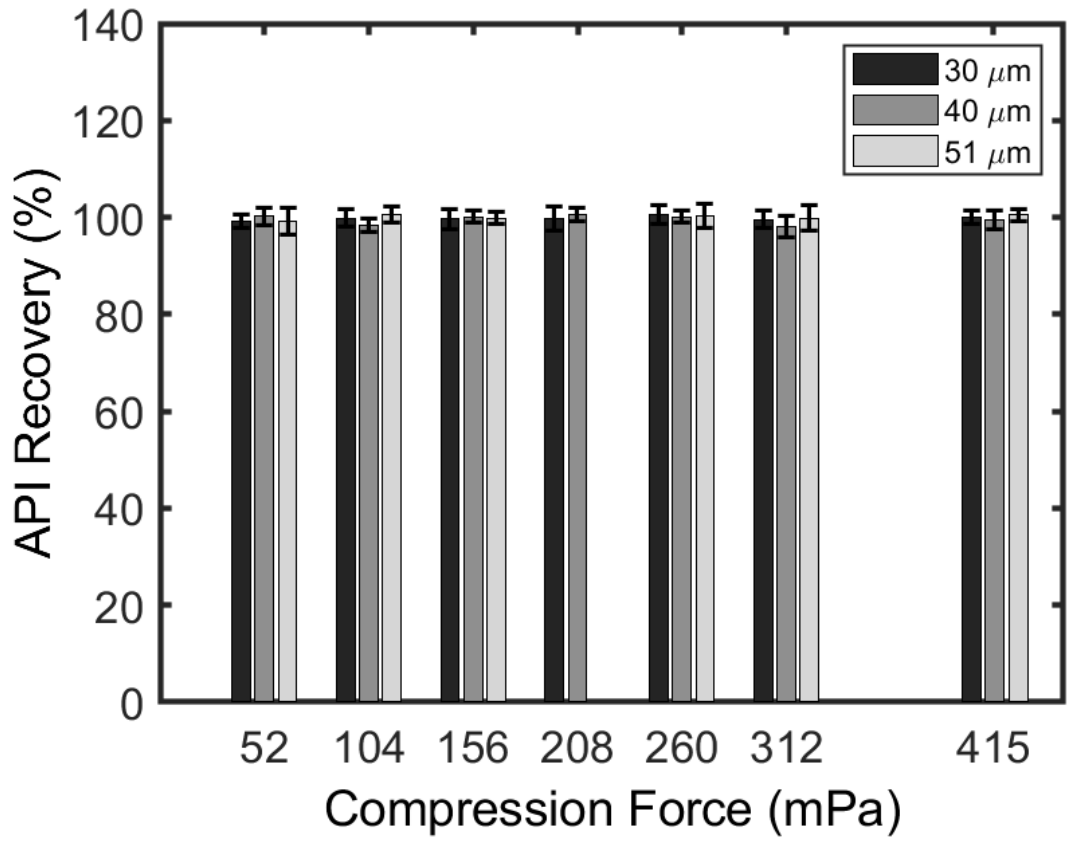

Figure C-1: API recovery as a function of compression force for all batches.

9 References

Alshihabi, F., Vandamme, T., & Betz, G. (2012). *Predicting physical properties of pharmaceutical compacts using focused beam reflectance measurement (FBRM). Journal of Drug Delivery Science and Technology,* (Vol. 22, Issue 6). https://doi.org/https://doi.org/10.1016/S1773-2247(12)50091-2.

Anuschek, M., Skelbæk-Pedersen, A. L., Kvistgaard Vilhelmsen, T., Skibsted, E., Zeitler, J. A., & Rantanen, J. (2023). Terahertz time-domain spectroscopy for the investigation of tablets prepared from roller compacted granules. *International Journal of Pharmaceutics*, (Vol. 642), 1–10. https://doi.org/10.1016/j.ijpharm.2023.123165

Auger, J. C., & Stout, B. (2012). Dependent light scattering in white paint films: Clarification and application of the theoretical concepts. *Journal of Coatings Technology and Research*, *9*(3), 287–295. https://doi.org/10.1007/s11998-011-9371-9

Auger, J. C., & Stout, B. (2013). Discussion on dependent light scattering phenomenon in white paint films. *Journal of Coatings Technology and Research*, *10*(6), 929–931. https://doi.org/10.1007/s11998-013-9539-6

Auger, J.-C., & Stout, B. (2013). Response to "Dependent light scattering in white paint films: clarification and application of the theoretical concepts." *J. Coat. Technol. Res*, *10*(6), 923–927. https://doi.org/10.1007/s11998-011-9731-9

Bär, D., Debus, H., Brzenczek, S., Fischer, W., & Imming, P. (2018). Determining particle size and water content by near-infrared spectroscopy in the granulation of naproxen sodium. *Journal of Pharmaceutical and Biomedical Analysis*, *151*(1), 209–218. https://doi.org/10.1016/j.jpba.2018.01.005

Bawuah, P., Karttunen, A.-P., Markl, D., Ridgway, C., Korhonen, O., Gane, P., Zeitler, J. A., Ketolainen, J., & Peiponen, K. E. (2018). Investigating elastic relaxation effects on the optical properties of functionalised calcium carbonate compacts using optics-based Heckel analysis. *International Journal of Pharmaceutics*, *544*(1), 278–284. https://doi.org/10.1016/j.ijpharm.2018.04.043

Bawuah, P., Markl, D., Farrell, D., Evans, M., Portieri, A., Anderson, A., Goodwin, D., Lucas, R., & Zeitler, J. A. (2020). Terahertz-Based Porosity Measurement of Pharmaceutical Tablets: a Tutorial. *Journal of Infrared, Millimeter, and Terahertz Waves*, *41*(4), 450–469. https://doi.org/10.1007/s10762-019-00659-0

Bawuah, P., Markl, D., Turner, A., Evans, M., Portieri, A., Farrell, D., Lucas, R., Anderson, A., Goodwin, D. J., & Zeitler, J. A. (2020). A Fast and Non-destructive Terahertz Dissolution Assay for Immediate Release Tablets. *Journal of Pharmaceutical Sciences*, *110*(1), 1–10. https://doi.org/10.1016/j.xphs.2020.11.041

Bawuah, P., Tan, N., Tweneboah, S. N. A., Ervasti, T., Axel Zeitler, J., Ketolainen, J., & Peiponen, K. E. (2016). Terahertz study on porosity and mass fraction of active pharmaceutical ingredient of pharmaceutical tablets. *European Journal of Pharmaceutics and Biopharmaceutics*, *105(1)*, 122–133. https://doi.org/10.1016/j.ejpb.2016.06.007

Beekman, A., Shan, D., Ali, A., Dai, W., Ward-Smith, S., & Goldenberg, M. (2005). Micrometer-scale particle sizing by laser diffraction: Critical impact of the imaginary component of refractive index. *Pharmaceutical Research*, *22*(4), 518–522. https://doi.org/10.1007/s11095-005-2494-x

Born, P., & Holldack, K. (2017). Analysis of granular packing structure by scattering of THz radiation. *Review of Scientific Instruments*, *88*(5), 1-12. https://doi.org/10.1063/1.4983045

Born, P., Holldack, K., & Sperl, M. (2015). Particle characterization using THz spectroscopy. *Granular Matter*, *17*(5), 531–536. https://doi.org/10.1007/s10035-015-0578-9

Born, P., Rothbart, N., Sperl, M., & Hübers, H. W. (2014). Granular structure determined by terahertz scattering. *Europhysics Letters*, *106*(4), 1-5. https://doi.org/10.1209/0295-5075/106/48006

Bosquillon, C., Lombry, C., Preat, V., & Vanbever, R. (2001). Comparison of particle sizing techniques in the case of inhalation dry powders. *Journal of Pharmaceutical Sciences*, *90*(12), 2032–2041. https://doi.org/10.1002/jps.1154

Bründermann, Erik & Hübers, Heinz-Wilhelm & Kimmitt, Maurice. (2012). Terahertz Techniques. 10.1007/978-3-642-02592-1.

Burgess, D. J., Duffy, E., Etzler, F., & Hickey, A. J. (2004). Particle size analysis: AAPS workshop report, cosponsored by the food and drug administration and the United States pharmacopeia. *AAPS Journal*, *6*(3), 1-12. https://doi.org/10.1208/aapsj060320

Busch, S. F., Weidenbach, M., Fey, M., Schäfer, F., Probst, T., & Koch, M. (2014). Optical Properties of 3D Printable Plastics in the THz Regime and their Application for 3D Printed THz Optics. *Journal of Infrared, Millimeter, and Terahertz Waves*, *35*(12), 993–997. https://doi.org/10.1007/s10762-014-0113-9

Carlon, H. R. (1979). Christiansen effect in IR spectra of soil-derived atmospheric dusts. *Applied Optics*, *18*(21), 3610–3614.

Challa, S., & Potumarthi, R. (2013). Chemometrics-based process analytical technology (PAT) tools: Applications and adaptation in pharmaceutical and biopharmaceutical industries. *Applied Biochemistry and Biotechnology*, *169*(1), 66–76. https://doi.org/10.1007/s12010-012-9950-y

Clarke, R. H. (1968). A Theory for the Christiansen Filter. *Applied Optics* , *7*(5), 861–868.

Clegg, I. (2020). Specification of Drug Substances and Products. In Riley M. Christopher, Rosanske W. Thomas, & Reid George (Eds.), *Specification of Drug Substances and Products: Development and Validation of Analytical Methods, Second Edition*. Elsevier Ltd. https://doi.org/10.1016/B978-0-08-102824-7.00007-5

Coutant, C. A., Skibic, M. J., Doddridge, G. D., Kemp, C. A., & Sperry, D. C. (2010). In vitro monitoring of dissolution of an immediate release tablet by focused beam reflectance measurement. *Molecular Pharmaceutics*, *7*(5), 1508–1515. https://doi.org/10.1021/mp1001476

D'Angelo, F., Bonn, M., Gente, R., Koch, M., & Turchinovich, D. (2014). Ultra-broadband THz time-domain spectroscopy of common polymers with THz air-photonics. *Conference on Lasers and Electro-Optics Europe - Technical Digest*, *22*(10), 2924–2926. https://doi.org/10.1364/oe.22.012475

Dave, K., Luner, P. E., Forness, C., Baker, D., Jankovsky, C., & Chen, S. (2017). Feasibility of Focused Beam Reflectance Measurement (FBRM) for Analysis of Pharmaceutical Suspensions in Preclinical Development. *AAPS PharmSciTech*, *19*(1), 155–165. https://doi.org/10.1208/s12249-017-0819-9

Duvillaret, L., Garet, F., & Coutaz, J. L. (1996). A reliable method for extraction of material parameters in terahertz time-domain spectroscopy. *IEEE Journal on Selected Topics in Quantum Electronics*, *2*(3), 739–745. https://doi.org/10.1109/2944.571775

Duvillaret, L., Garet, F., & Coutaz, J.-L. (1999). Highly precise determination of optical constants and sample thickness in terahertz time-domain spectroscopy. *Applied Optics*, *38*(2), 409-415. https://doi.org/10.1364/ao.38.000409

Engelbrecht, S., Tybussek, K. H., Sampaio, J., Böhmler, J., Fischer, B. M., & Sommer, S. (2019). Monitoring the Isothermal Crystallization Kinetics of PET-A Using THz-TDS. *Journal of Infrared, Millimeter, and Terahertz Waves*, *40*(3), 306–313. https://doi.org/10.1007/s10762-019-00570-8

Franz, M., Fischer, B. M., & Walther, M. (2008). The Christiansen effect in terahertz time-domain spectra of coarse-grained powders. *Applied Physics Letters*, *92*(2), 2–4. https://doi.org/10.1063/1.2831910

Garet, F., Hofman, M., Meilhan, J., Simoens, F., & Coutaz, J. L. (2014). Evidence of Mie scattering at terahertz frequencies in powder materials. *Applied Physics Letters*, *105*(3), 1-4. https://doi.org/10.1063/1.4890732

Gohel MC, Jogani PD. A review of co-processed directly compressible excipients. J Pharm Sci. 2005 Apr 16;8(1):76-93. PMID: 15946601.

Grinchuk, P. S. (2003). Scattering of radiation in a heterogeneous medium near the percolation threshold. *Physica B: Condensed Matter*, *338*(1), 252–255. https://doi.org/10.1016/j.physb.2003.08.004

Grubbs, J., Tsaknopoulos, K., Massar, C., Young, B., O'Connell, A., Walde, C., Birt, A., Siopis, M., & Cote, D. (2021). Comparison of laser diffraction and image analysis techniques for particle size-shape characterization in additive manufacturing applications. *Powder Technology*, *391*(1), 20–33. https://doi.org/10.1016/j.powtec.2021.06.003

Gupta, S., Igne, B., Omar, T., Román-Ospino, A. D., Hausner, D., & Muzzio, F. (2022). Multi-layer Raman chemical mapping to investigate the effect of API particle size and blending shear rate on API domain sizes in pharmaceutical tablets. *International Journal of Pharmaceutics*, *624*(1), 1-15. https://doi.org/10.1016/j.ijpharm.2022.122052

Hartley, P. A., Parfitt, G. D., & Pollack, L. B. (1985). The role of the van der Waals force in the agglomeration of powders containing submicron particles. *Powder Technology*, *42*(1), 35–46. https://doi.org/10.1016/0032-5910(85)80036-X

Hausner, D., & Muzzio, F. (2022). *Multi-layer Raman chemical mapping to investigate the effect of API particle size and blending shear rate on API domain sizes in pharmaceutical tablets*. *624*(1), 1-15. https://doi.org/10.1016/j.ijpharm.2022.122052

Hermanto, M. W., Chow, P. S., & Tan, R. B. H. (2010). Implementation of focused beam reflectance measurement (FBRM) in antisolvent crystallization to achieve consistent product quality. *Crystal Growth and Design*, *10*(8), 3668–3674. https://doi.org/10.1021/cg100533n

Higgins, J. P., Arrivo, S. M., Thurau, G., Green, R. L., Bowen, W., Lange, A., Templeton, A. C., Thomas, D. L., & Reed, R. A. (2003). Spectroscopic approach for on-line monitoring of particle size during

the processing of pharmaceutical nanoparticles. *Analytical Chemistry*, *75*(8), 1777–1785. https://doi.org/10.1021/ac0207980

Hoffmann, M., Wray, P. S., Gamble, J. F., & Tobyn, M. (2015). Investigation into process-induced de-aggregation of cohesive micronised API particles. *International Journal of Pharmaceutics*, *493*(1–2), 341–346. https://doi.org/10.1016/j.ijpharm.2015.07.073

Jepsen, P. U. (2019). Phase Retrieval in Terahertz Time-Domain Measurements: a "how to" Tutorial. *Journal of Infrared, Millimeter, and Terahertz Waves*, *40*(1), 395–411. https://doi.org/10.1007/s10762-019-00578-0

Jepsen, P. U., Cooke, D. G., & Koch, M. (2011). Terahertz spectroscopy and imaging - Modern techniques and applications. *Laser and Photonics Reviews*, *5*(1), 124–166. https://doi.org/10.1002/lpor.201000011

Jepsen, P. U., & Fischer, B. M. (2005). Dynamic range in terahertz time-domain transmission and reflection spectroscopy. *Optics Letters, 30*(1), 29–31. https://doi.org/10.1364/OL.30.000029

Kail, N., Marquardt, W., & Briesen, H. (2009). Process analysis by means of focused beam reflectance measurements. *Industrial and Engineering Chemistry Research*, *48*(6), 2936–2946. https://doi.org/10.1021/ie800839s

Kumar, V., Taylor, M. K., Mehrotra, A., & Stagner, W. C. (2013). Real-time particle size analysis using focused beam reflectance measurement as a process analytical technology tool for a continuous granulation-drying- milling process. *AAPS PharmSciTech*, *14*(2), 523–530. https://doi.org/10.1208/s12249-013-9934-4

Latimer, P., & Wamble, F. (1982). Light scattering by aggregates of large colloidal particles. *Applied Optics* , *21*(13), 2447–2455. https://doi.org/10.1364/AO.21.002447

Li, M., Wilkinson, D., & Patchigolla, K. (2006). Obtaining particle size distribution from chord length measurements. *Particle and Particle Systems Characterization*, *23*(2), 170–174. https://doi.org/10.1002/ppsc.200601026

Ma, Z., Merkus, H. G., De Smet, J. G. A. E., Heffels, C., & Scarlett, B. (2000). New developments in particle characterization by laser diffraction: Size and shape. *Powder Technology*, *111*(1), 66–78. https://doi.org/10.1016/S0032-5910(00)00242-4

Maclean, N., Khadra, I., Mann, J., Williams, H., Abbott, A., Mead, H., & Markl, D. (2022). Investigating the role of excipients on the physical stability of directly compressed tablets. *International Journal of Pharmaceutics: X*, *4*(1), 1–9. https://doi.org/10.1016/j.ijpx.2021.100106

Markl, D., Sauerwein, J., Goodwin, D. J., van den Ban, S., & Zeitler, J. A. (2017). Non-destructive Determination of Disintegration Time and Dissolution in Immediate Release Tablets by Terahertz Transmission Measurements. *Pharmaceutical Research*, *34*(5), 1012–1022. https://doi.org/10.1007/s11095-017-2108-4

Markl, D., Strobel, A., Schlossnikl, R., Bøtker, J., Bawuah, P., Ridgway, C., Rantanen, J., Rades, T., Gane, P., Peiponen, K. E., & Zeitler, J. A. (2018). Characterisation of pore structures of pharmaceutical tablets: A review. In *International Journal of Pharmaceutics* 538(1), 188–214. Elsevier B.V. https://doi.org/10.1016/j.ijpharm.2018.01.017

Markl, D., & Zeitler, J. A. (2017). A Review of Disintegration Mechanisms and Measurement Techniques. *Pharmaceutical Research*, *34*(5), 890–917. https://doi.org/10.1007/s11095-017-2129-z

Martin Rhodes. (2008). Particle Size Analysis. In Martin Rhodes (Ed.), *Introduction to Particle Technology* (2nd ed., Vol. 1, pp. 1–28). Wiley. https://doi.org/10.1002/9780470727102.ch1

Mobaraki, N., & Amigo, J. M. (2018). HYPER-Tools. A graphical user-friendly interface for hyperspectral image analysis. *Chemometrics and Intelligent Laboratory Systems*, *172*(September 2017), 174–187. https://doi.org/10.1016/j.chemolab.2017.11.003

Murphy, K. N., Naftaly, M., Nordon, A., & Markl, D. (2021). Effect of Microsphere Concentration and Size in Compacts on Terahertz Scattering. *2021 51st European Microwave Conference, EuMC 2021*, *1*(1), 994–997. https://doi.org/10.23919/EuMC50147.2022.9784372

Murphy, K. N., Naftaly, M., Nordon, A., & Markl, D. (2022a). Analysis of THz Scattering of Compacted Granular Materials using THz-TDS. *International Conference on Infrared, Millimeter, and Terahertz Waves, IRMMW-THz*, *2022-August*, 1–2. https://doi.org/10.1109/IRMMW-THz50927.2022.9895792

Murphy, K. N., Naftaly, M., Nordon, A., & Markl, D. (2022b). Polymer Pellet Fabrication for Accurate THz-TDS Measurements. *Applied Sciences*, *12*(7), 1–14. https://doi.org/10.3390/app12073475

Murphy, K. N, Naftaly, M, Nordon, A, & Markl, D. (2023) "Effect of particle size and concentration on low-frequency terahertz scattering in granular compacts [Invited]," *Optics. Materials. Express*, 13(1), 2251-2263. https://doi.org/10.1364/OME.494825

Naftaly, M. (2014). *Terahertz Metrology* (1st ed, Vol 1)Artech House. https://uk.artechhouse.com/Terahertz-Metrology-P1697.aspx

Naftaly, M., & Dudley, R. (2009). Methodologies for determining the dynamic ranges and signal-to-noise ratios of terahertz time-domain spectrometers. *Optics Letters*, *34*(8), 1213–1215. https://doi.org/10.1364/ol.34.001213

Naftaly, M., & Miles, R. E. (2005). Terahertz time-domain spectroscopy: A new tool for the study of glasses in the far infrared. *Journal of Non-Crystalline Solids*, *351*(40), 3341–3346. https://doi.org/10.1016/j.jnoncrysol.2005.08.003

Naftaly, M., & Miles, R. E. (2007). Terahertz time-domain spectroscopy for material characterization. *Proceedings of the IEEE*, *95*(8), 1658–1665. https://doi.org/10.1109/JPROC.2007.898835

Naftaly, M., Tikhomirov, I., Hou, P., & Markl, D. (2020). Measuring open porosity of porous materials using thz-tds and an index-matching medium. *MDPI Sensors*, *20*(1), 1–11. https://doi.org/10.3390/s20113120

Naftaly, Vieweg, & Deninger. (2019). Industrial Applications of Terahertz Sensing: State of Play. *Sensors*, *19*(1), 1–35. https://doi.org/10.3390/s19194203

Neu, J., & Schmuttenmaer, C. A. (2018). Tutorial: An introduction to terahertz time domain spectroscopy (THz-TDS). *Journal of Applied Physics*, *124*(23), 1-14. https://doi.org/10.1063/1.5047659

Newton, R. G. (2013). *Scattering Theory of Waves and Particles* (1st ed, Vol 1).Springer Berlin. https://doi.org/https://doi.org/10.1007/978-3-642-88128-2

Özer, Z., Gök, S., Altan, H., & Severcan, F. (2014). Concentration-based measurement studies of L-tryptophan using terahertz time-domain spectroscopy (THz-TDS). *Applied Spectroscopy*, *68*(1), 95–100. https://doi.org/10.1366/13-07165

Pasikatan, M. C., Steele, J. L., Spillman, C. K., & Haque, E. (2001). Near infrared reflectance spectroscopy for online particle size analysis of powders and ground materials. *Journal of Near Infrared Spectroscopy*, *9*(3), 153–164. https://doi.org/10.1255/jnirs.303

Pauli, V., Roggo, Y., Kleinebudde, P., & Krumme, M. (2019). Real-time monitoring of particle size distribution in a continuous granulation and drying process by near infrared spectroscopy. *European Journal of Pharmaceutics and Biopharmaceutics*, *141*(1), 90–99. https://doi.org/10.1016/j.ejpb.2019.05.007

Pierno, L., Fiorello, A. M., Scafe, S., Cunningham, J., Burnett, A. D., Linfield, E. H., & Davies, A. G. (2013). THz-TDS analysis of hidden explosives for homeland security scenarios. *UCMMT 2013* -

2013 6th UK, Europe, China Millimeter Waves and THz Technology Workshop, *1*(1). https://doi.org/10.1109/UCMMT.2013.6641516

Puc, U., Abina, A., Jeglič, A., Zidanšek, A., Kašalynas, I., Venckevičius, R., & Valušis, G. (2018). Spectroscopic analysis of melatonin in the terahertz frequency range. *Sensors*, *18*(12), 1–12. https://doi.org/10.3390/S18124098

Raman, C. V. (1949). The theory of the Christiansen experiment. *Proceedings of the Indian Academy of Sciences - Section A*, *29*(6), 381–390. https://doi.org/10.1007/BF03036872

Rawle, A. (2014). Basic Principles of Particle Size Analysis, Technical Report. *Particle Science - Guide*, *1*(1), 1–19. https://www.atascientific.com.au/basic-principles-of-particle-size-analysis

Reynolds, G. K., Campbell, J. I., & Roberts, R. J. (2017). A compressibility based model for predicting the tensile strength of directly compressed pharmaceutical powder mixtures. *International Journal of Pharmaceutics*, *531*(1), 215–224. https://doi.org/10.1016/j.ijpharm.2017.08.075

Shekunov, B. Y., Chattopadhyay, P., Tong, H. H. Y., & Chow, A. H. L. (2007). Particle size analysis in pharmaceutics: Principles, methods, and applications. *Pharmaceutical Research*, *24*(2), 203–227. https://doi.org/10.1007/s11095-006-9146-7

Shekunov, B. Y., Feeley, J. C., Chow, A. H. L., Tong, H. H. Y., & York, P. (2003). Aerosolisation behaviour of micronised and supercritically-processed powders. *Journal of Aerosol Science*, *34*(5), 553–568. https://doi.org/10.1016/S0021-8502(03)00022-3

Shen, Y. C., Taday, P. F., & Pepper, M. (2008). Elimination of scattering effects in spectral measurement of granulated materials using terahertz pulsed spectroscopy. *Applied Physics Letters*, *92*(5), 2-4. https://doi.org/10.1063/1.2840719

Silva, A. F. T., Burggraeve, A., Denon, Q., Van Der Meeren, P., Sandler, N., Van Den Kerkhof, T., Hellings, M., Vervaet, C., Remon, J. P., Lopes, J. A., & De Beer, T. (2013). Particle sizing measurements in pharmaceutical applications: Comparison of in-process methods versus off-line methods. *European Journal of Pharmaceutics and Biopharmaceutics*, *85*(1), 1006–1018. https://doi.org/10.1016/j.ejpb.2013.03.032

Silva, V. H., Vieira, F. S., Rohwedder, J. J. R., Pasquini, C., & Pereira, C. F. (2017). Multivariate quantification of mebendazole polymorphs by terahertz time domain spectroscopy (THz-TDS). *Analyst*, *142*(9), 1519–1524. https://doi.org/10.1039/c6an02540d

Skelbæk-Pedersen, A. L., Anuschek, M., Vilhelmsen, T. K., Rantanen, J., & Zeitler, J. A. (2020). Non-destructive quantification of fragmentation within tablets after compression from scattering

analysis of terahertz transmission measurements. *International Journal of Pharmaceutics*, *588*(1), 119769. https://doi.org/10.1016/j.ijpharm.2020.119769

Smith, R. M., & Arnold, M. A. (2011). Terahertz time-domain spectroscopy of solid samples: Principles, applications, and challenges. *Applied Spectroscopy Reviews*, *46*(8), 636–679. https://doi.org/10.1080/05704928.2011.614305

Sommer, S., Raidt, T., Fischer, B. M., Katzenberg, F., Tiller, J. C., & Koch, M. (2016a). THz-Spectroscopy on High Density Polyethylene with Different Crystallinity. *Journal of Infrared, Millimeter, and Terahertz Waves*, *37*(2), 189–197. https://doi.org/10.1007/s10762-015-0219-8

Sommer, S., Raidt, T., Fischer, B. M., Katzenberg, F., Tiller, J. C., & Koch, M. (2016b). THz-Spectroscopy on High Density Polyethylene with Different Crystallinity. *Journal of Infrared, Millimeter, and Terahertz Waves*, *37*(2), 189–197. https://doi.org/10.1007/s10762-015-0219-8

Stojanovska Pecova, M., Geskovski, N., Petrushevski, G., & Makreski, P. (2021). A Novel Method for Rapid Particle Size Analysis of Ibuprofen Using Near-infrared Spectroscopy. *AAPS PharmSciTech*, *22*(8), 1–13. https://doi.org/10.1208/s12249-021-02156-x

Stranzinger, S., Faulhammer, E., Li, J., Dong, R., Khinast, J. G., Zeitler, J. A., & Markl, D. (2019). Measuring bulk density variations in a moving powder bed via terahertz in-line sensing. *Powder Technology*, *344*(1), 152–160. https://doi.org/10.1016/j.powtec.2018.11.106

Stranzinger, S., Faulhammer, E., Li, J., Dong, R., Zeitler, J. A., Biserni, S., Calzolari, V., Khinast, J. G., & Markl, D. (2019). Predicting capsule fill weight from in-situ powder density measurements using terahertz reflection technology. *International Journal of Pharmaceutics: X*, *1*, 100004. https://doi.org/10.1016/j.ijpx.2018.100004

Sun, C. (2005). True density of microcrystalline cellulose. *Journal of Pharmaceutical Sciences*, *94*(1), 2132–2134. https://doi.org/10.1002/jps.20459

Swarbrick, J. (2019). Tablet Manufacture by Direct Compression. In Swarbrick James (Ed.), Encyclopedia of Pharmaceutical Technology (3rd ed, Vol. 1). Informa Heathcare. https://doi.org/10.1201/b19309-20

Twersky, V. (1964). Rayleigh Scattering. *Applied Optics*, *3*(10), 1150-1162. https://doi.org/10.1364/ao.3.001150

Wietzke, S., Jansen, C., Reuter, M., Jung, T., Kraft, D., Chatterjee, S., Fischer, B. M., & Koch, M. (2011). Terahertz spectroscopy on polymers: A review of morphological studies. *Journal of Molecular Structure*, *1006*(1), 41–51. https://doi.org/10.1016/j.molstruc.2011.07.036

Withayachumnankul, W, Lin, H, Mickan, S. P, Fischer, B. M, and Abbott, D Analysis of measurement uncertainty in THz-TDS, Proc. SPIE 6593, Photonic Materials, Devices, and Applications II, 659326 (12 June 2007); https://doi.org/10.1117/12.721876

Withayachumnankul, W., & Naftaly, M. (2014). Fundamentals of measurement in terahertz time-domain spectroscopy. *Journal of Infrared, Millimeter, and Terahertz Waves*, *35*(8), 610–637. https://doi.org/10.1007/s10762-013-0042-z

Wu, C. Y., Hancock, B. C., Mills, A., Bentham, A. C., Best, S. M., & Elliott, J. A. (2008). Numerical and experimental investigation of capping mechanisms during pharmaceutical tablet compaction. *Powder Technology*, *181*(2), 121–129. https://doi.org/10.1016/j.powtec.2006.12.017

Wu, F. M., Wu, B. F., Zhao, X. Y., Zhang, Z. H., Zhang, H., Zhang, T. Y., & Fang, Y. (2015). Analysis on scattering and relationship with granular size in THz spectra. *IRMMW-THz 2015 - 40th International Conference on Infrared, Millimeter, and Terahertz Waves*. https://doi.org/10.1109/IRMMW-THz.2015.7327782

Wünsch, I., Friesen, I., Puckhaber, D., Schlegel, T., & Finke, J. H. (2020). Scaling tableting processes from compaction simulator to rotary presses—mind the sub-processes. *Pharmaceutics*, *12*(4), 1–18. https://doi.org/10.3390/pharmaceutics12040310

Xu, R. (2015). Light scattering: A review of particle characterization applications. In *Particuology*.18(1), 11–21. Elsevier B.V. https://doi.org/10.1016/j.partic.2014.05.002

Yamamoto, K., Yamaguchi, M., Tani, M., Hangyo, M., Teramura, S., Isu, T., & Tomita, N. (2004). Degradation diagnosis of ultrahigh-molecular weight polyethylene with terahertz-time-domain spectroscopy. *Applied Physics Letters*, *85*(22), 5194–5196. https://doi.org/10.1063/1.1827332

Zeitler, J. A. (2016). Terahertz Spectroscopy and Imaging. In K.-E. Peiponen (Ed.), *Terahertz Spectroscopy and Imaging* (1st ed) 171–222. Springer. https://doi.org/10.1007/978-1-4939-4029-5_5

Zeitler, J. A., & Shen, Y.-C. (2012). Industrial Applications of Terahertz Imaging. In Rhodes W. T. (Ed.), *Terahertz Spectroscopy and Imaging* (1st ed), 451–489. Springer. https://doi.org/10.1007/978-3-642-29564-5_18

Zhong, H., Chan, G., Hu, Y., Hu, H., & Ouyang, D. (2018). A comprehensive map of FDA-approved pharmaceutical products. *Pharmaceutics*, *10*(4), 1–19. https://doi.org/10.3390/pharmaceutics10040263